

Discrimination of  
Neutral Current Background  
in a Future Long-Baseline Experiment  
with LENA

Diploma Thesis  
Institut für Experimentalphysik  
Universität Hamburg

by

Sebastian Lorenz

January 2012



**Universität Hamburg**

**DER FORSCHUNG | DER LEHRE | DER BILDUNG**



## Abstract

The 50 kt liquid scintillator detector LENA (**L**ow **E**nergy **N**eutrino **A**stronomy) is one possible option for a future European neutrino observatory. In the framework of the LAGUNA-LBNO design study, its application as a far detector in a long-baseline neutrino beam oscillation experiment is evaluated. The present thesis investigates the impact of background from NC neutrino interactions on LENA's sensitivity to measure  $\theta_{13}$ ,  $\delta_{CP}$  and the neutrino mass hierarchy. Furthermore, first quantitative results on the discrimination efficiency for CC  $\nu_e$  and NC  $\pi^0$  events are presented, which represent a serious background to  $\nu_e$  appearance search in a  $\nu_\mu$  beam. Discrimination is obtained by a multivariate analysis with boosted decision trees and has been tested based on a large sample of simulated events.



## Zusammenfassung

Der 50 kt Flüssigszintillator-Detektor LENA (**L**ow **E**nergy **N**eutrino **A**stronomy) ist eine mögliche Option für ein zukünftiges europäisches Neutrino-Observatorium.

Im Rahmen der LAGUNA-LBNO Designstudie wird seine Verwendungsmöglichkeit als Fern-detektor in einem Langstrecken-Neutrinostrahl-Oszillationsexperiment evaluiert. Die vorliegende Diplomarbeit untersucht den Einfluss von Untergrund durch NC Neutrinointeraktionen auf LENAs Sensitivität zur Messung von  $\theta_{13}$ ,  $\delta_{CP}$  und der Neutrino-Massenhierarchie. Des Weiteren werden erste quantitative Resultate zur Diskriminierungseffizienz für CC  $\nu_e$ - und NC  $\pi^0$ -Ereignisse präsentiert, die einen ernstzunehmenden Untergrund für die Suche nach Auftauchen von  $\nu_e$  in einem  $\nu_\mu$  Strahl darstellen. Die Diskriminierung wird durch eine multivariate Analyse mit verstärkten Entscheidungsbäumen erhalten und wurde basierend auf einer großen Auswahl von simulierten Ereignissen getestet.



# Contents

<b>1</b>	<b>Introduction</b>	<b>1</b>
<b>2</b>	<b>Neutrino oscillations</b>	<b>3</b>
2.1	Neutrinos in the Standard Model . . . . .	3
2.2	Neutrino oscillations in vacuum . . . . .	4
2.3	Neutrino oscillations in matter . . . . .	6
2.4	Measurement of mixing parameters . . . . .	7
2.4.1	Present knowledge on mixing parameters . . . . .	8
2.4.2	Current issues of neutrino oscillations physics . . . . .	9
2.4.3	Contributions from a neutrino beam experiment . . . . .	9
2.4.4	Degeneracies in neutrino beam experiments . . . . .	10
<b>3</b>	<b>The LENA experiment</b>	<b>13</b>
3.1	Large Apparatus for Grand Unification and Neutrino Astrophysics . . . . .	13
3.1.1	LAGUNA design study . . . . .	13
3.1.2	LAGUNA-LBNO . . . . .	14
3.2	LENA detector design . . . . .	15
3.2.1	Liquid scintillator . . . . .	16
3.2.2	Light detection and readout electronics . . . . .	18
3.2.3	Detector tank and laboratory site . . . . .	19
3.3	Physics potential of LENA . . . . .	21
3.3.1	Solar neutrinos . . . . .	21
3.3.2	Supernova neutrinos and Diffuse Supernova Neutrino Background . . . . .	22
3.3.3	Geo- and reactor neutrinos . . . . .	24
3.3.4	Neutrino beams . . . . .	24
3.3.5	Nucleon decay . . . . .	25
<b>4</b>	<b>Neutrino oscillation search with a neutrino beam experiment</b>	<b>27</b>
4.1	Concept of an oscillation experiment with a neutrino beam . . . . .	27
4.1.1	General aspects of neutrino beams . . . . .	27
4.1.2	Creation of a conventional muon-neutrino beam . . . . .	28
4.1.3	Detection of high-energy beam neutrinos for oscillation analysis . . . . .	29
4.2	Neutral pion background to electron-neutrino appearance search . . . . .	31
4.2.1	Neutral pion production . . . . .	31
4.2.2	Background from neutral pion decay . . . . .	32

4.2.3	Particle track reconstruction & identification of neutral pion events . . .	33
4.3	Long-baseline oscillation experiment with LENA . . . . .	35
4.3.1	LENA as a far detector . . . . .	35
4.3.2	Sensitivity to mixing parameters & impact of neutral current background	37
<b>5</b>	<b>Variables for multivariate analysis</b>	<b>41</b>
5.1	Monte Carlo simulation . . . . .	41
5.1.1	Simulation setup . . . . .	41
5.1.2	Simulation of signal and background events . . . . .	43
5.2	Time-of-flight-corrected first hit time . . . . .	44
5.2.1	Barycenter reconstruction . . . . .	44
5.2.2	Time-of-flight correction . . . . .	45
5.2.3	Time-of-flight-corrected first hit time as event variable . . . . .	46
5.3	Reconstructed energy . . . . .	48
5.4	First hit pulse shape variables . . . . .	51
5.4.1	First hit pulse shape & Adaptive kernel estimation . . . . .	51
5.4.2	Maximum pulse height . . . . .	52
5.4.3	Pulse fall . . . . .	53
5.4.4	Pulse rise . . . . .	53
5.4.5	Pulse width . . . . .	53
5.4.6	Pulse mean time . . . . .	54
5.5	First hit pulse evolution variables . . . . .	56
5.5.1	Description of pulse evolution . . . . .	56
5.5.2	Determination of variables from pulse evolution . . . . .	58
<b>6</b>	<b>Multivariate analysis with Boosted Decision Trees</b>	<b>61</b>
6.1	Boosted Decision Trees . . . . .	61
6.1.1	Functionality of decision trees . . . . .	61
6.1.2	Boosting of decision trees . . . . .	63
6.1.3	Overtraining . . . . .	65
6.2	Correlations between the MVA variables . . . . .	65
6.3	MVA settings and results . . . . .	67
6.3.1	General analysis . . . . .	68
6.3.2	Energy-dependent analysis . . . . .	71
<b>7</b>	<b>Conclusion and Outlook</b>	<b>77</b>
<b>A</b>	<b>Neutral pion decay kinematics</b>	<b>79</b>
<b>B</b>	<b>Utilized software frameworks</b>	<b>83</b>

# Nomenclature

(V–A)-theory	....	Vector-minus-Axial-vector-theory
AdaBoost	.....	ADAPtive BOOST
AKE	.....	Adaptive Kernel Estimation
BDT	.....	Boosted Decision Tree
BooNE	.....	BOOster Neutrino Experiment
CC	.....	Charged Current
CERN	.....	Conseil Européen pour la Recherche Nucléaire - European Organization for Nuclear Research
CNO	.....	Carbon-Nitrogen-Oxygen fusion cycle
DAQ	.....	Data AcQuisition
DSNB	.....	Diffuse Supernova Neutrino Background
FADC	.....	Fast Analogue-to-Digital Converter
FKE	.....	Fixed Kernel Estimation
FNAL	.....	Fermi National Accelerator Laboratory
GEANT	.....	GEometry ANd Tracking
GLACIER	.....	Giant Liquid Argon Charge Imaging ExpeRiment
GLOBES	.....	General LONg Baseline Experiment Simulator
GS	.....	Giga-Samples
GUT	.....	Grand Unified Theory
HP-PS	.....	High Power Proton Synchrotron
ICARUS	.....	Imaging Cosmic and Rare Underground Signals
K–S	.....	Kolmogorov-Smirnov
Kamiokande	....	KAMIOKA Nucleon Decay Experiment
KamLAND	.....	KAMioka Liquid Scintillator Anti-Neutrino Detector
KATRIN	.....	KARlsruhe TRItium Neutrino
LAB	.....	Linear AlkylBenzene
LAGUNA	.....	Large Apparatus for Grand Unification and Neutrino Astrophysics
LBNO	.....	Long Baseline Neutrino Oscillations
LENA	.....	Low Energy Neutrino Astronomy
LNGS	.....	Laboratori Nazionali del Gran Sasso
LSM	.....	Laboratoire Souterrain de Modane
MEMPHYS	....	MEgaton Mass PHYSics
MSW	.....	Mikheyev-Smirnov-Wolfenstein
MVA	.....	MultiVariate Analysis
mwe	.....	Meters Water Equivalent

NC .....	Neutral Current
NHF .....	Negative Horn Focusing
OC .....	Optical Coverage
pep .....	Proton-Electron-Proton fusion
PHF .....	Positive Horn Focusing
PMNS .....	Pontecorvo—Maki—Nakagawa—Sakata
PMT .....	PhotoMultiplier Tube
POT .....	Protons On Target
pp .....	Proton-Proton fusion
PREM .....	Preliminary Reference Earth Model
PXE .....	Phenyl-o-Xylyl-Ethane
ROC .....	Receiver Operating Characteristic
SciBar .....	SCIntillator BAR
SciBooNE .....	SCIBar BOOster Neutrino Experiment
SM .....	Standard Model
SN .....	SuperNova
SNO .....	Sudbury Neutrino Observatory
SSM .....	Standard Solar Model
SUSY .....	SUper SYmmetry
T2K .....	Tokai-to-Kamioka
TOF .....	Time-Of-Flight
TPC .....	Time Projection Chamber

# Chapter 1

## Introduction

Since the postulation of neutrinos by *Wolfgang Pauli* in 1930 [1] and confirmation of their existence by *Frederick Reines* and *Clyde L. Cowan, Jr.* in 1956 [2], neutrinos have been subject to extensive research. Particle detectors of increasing size and technological sophistication had to be built in order to address important questions regarding the neutrino's properties. Furthermore, the small reaction cross-sections of neutrinos make them ideal probes for terrestrial, galactic and extragalactic neutrino-emitting phenomena, where standard techniques are insufficient or impossible to use. Thereby, the neutrino has not only become an object of direct research, but also an invaluable carrier of information on physical processes for other questions in science.

Current issues in particle and astro-particle physics, which involve the neutrino properties themselves, as well as their probe character, require the construction of a next-generation neutrino observatory. Within Europe, this endeavor cannot be done by a single country, but has to become a project of international scope. The LAGUNA<sup>1</sup> project is one of these joint efforts to extend the knowledge in different branches of physics beyond the current state. The 50 kt liquid scintillator detector LENA<sup>2</sup> is one of the options possible in the framework of LAGUNA. Its design profits from wide experience on application of liquid scintillator in low-energy neutrino physics gained by experiments like Borexino [3] or KamLAND<sup>3</sup> [4].

The LAGUNA project also investigates the feasibility of a long-baseline neutrino beam experiment in order to determine the still hardly known mixing angle  $\theta_{13}$ , the CP-violating phase  $\delta_{CP}$  and the neutrino mass hierarchy. Valuable contributions are expected from the  $\bar{\nu}_e$  appearance search in a  $\bar{\nu}_\mu$  beam, but the sensitivity to the relevant oscillation effects depends on an effective rejection of neutral current background. Especially the production of single neutral pions in neutrino interactions is problematic, as the pion's decay products can mimic a  $\bar{\nu}_e$  event signature.

Liquid scintillator detectors have so far never been used as the far detector in a long-baseline beam experiment as they were assumed to be unable to reconstruct the high-energy neutrino events based on isotropic scintillation light. Due to this shortcoming, the ability to identify the background from single neutral pions was doubted as well. However, the idea to use

---

<sup>1</sup>LAGUNA: Large Apparatus for Grand Unification and Neutrino Astrophysics

<sup>2</sup>LENA: Low Energy Neutrino Astronomy

<sup>3</sup>KamLAND: Kamioka Liquid Scintillator Anti-Neutrino Detector

the arrival times of scintillation photons as the basis for the track reconstruction [5] was successfully demonstrated on Monte Carlo studies [6] [7].

Acting on this idea, a Monte Carlo simulation of the LENA detector was utilized to deduce characteristic event variables from neutral pion events and electron events. These variables were used to assess the efficiency of neutral pion and electron discrimination by a multivariate analysis with boosted decision trees up to energies of 1 GeV. The results are presented in this thesis, which is outlined as follows:

Chapter 2 covers the theory of neutrino oscillations and discusses the measurement of the associated mixing parameters in general. The second chapter gives an overview of the LAGUNA project as well as of the design and physics program of LENA. In Chapter 4 the concept of neutrino oscillation search with a superbeam is outlined, aiming to more explicitly motivate the topic of this thesis. The event parameters used for the multivariate analysis were deduced from simulated events—the underlying procedures are detailed in Chapter 5, whereas Chapter 6 covers the actual multivariate analysis with boosted decision trees.

# Chapter 2

## Neutrino oscillations

In this chapter the theory of neutrino oscillations in vacuum (Section 2.2) and matter (Section 2.3) is discussed, introducing neutrino properties beyond the representation in the SM<sup>1</sup> treated in Section 2.1. Finally some information and remarks regarding measurement of the theory's underlying parameters are given in Section 2.4.

### 2.1 Neutrinos in the Standard Model

The SM of elementary particle physics describes the fundamental, fermionic constituents of matter and their interactions through bosonic mediators of the fundamental forces. The fermions comprise the groups of leptons and quarks. Each of these groups can be separated into three families of two particles.

**Table 2.1:** Fermionic constituents of matter in the SM of elementary particle physics.

Fermions	Family			Charge	Color
	1	2	3		
Leptons	$\nu_e$	$\nu_\mu$	$\nu_\tau$	0	-
	$e^-$	$\mu^-$	$\tau^-$	-1	-
Quarks	$u$	$c$	$t$	+2/3	r, g, b
	$d$	$s$	$b$	-1/3	r, g, b

In the family of leptons one neutrino is associated to one charged lepton determining the neutrino's flavor (see Table 2.1). The neutrino is electrically neutral and has no strong charge (color). It couples only to the  $W^\pm$  and  $Z^0$  mediator bosons of weak interaction and therefore has a very small reactivity. Actually, in (V-A)-theory<sup>2</sup> of weak interaction the mentioned coupling is only on the left-handed component of neutrinos and on the right-handed component of anti-neutrinos. This has been arranged by definition to take violation of parity in beta decay into account. As a direct consequence neutrinos are massless particles in the SM [8].

However, some results from experimental neutrino physics can only be explained if one abandons the idea of massless neutrinos and thereby considers physics beyond the SM. One ex-

---

<sup>1</sup>SM: Standard Model

<sup>2</sup>(V-A)-theory: "Vector-minus-axial-vector"-theory

ample is the “Solar Neutrino Problem”. In the late 1960s, *Ray Davis Jr.* measured the flux of neutrinos from the Sun in the Homestake experiment [9]. In comparison to the SSM<sup>1</sup> [10] the measurement yielded a flux which was only about a third to a half of the expected flux. Further experiments confirmed the presence of a deficit. Available data can only be explained if the theory of neutrino oscillations is taken into account, which is topic of the following sections. This theory, first proposed by *Bruno Pontecorvo* in 1957, comes from the idea that neutrino flavors can transform into each other due to a non-vanishing neutrino rest mass. Predictions on further neutrino flavors contributing to the Sun’s original  $\nu_e$  flux were confirmed by measurements of the SNO<sup>2</sup> experiment in 2001 [11].

## 2.2 Neutrino oscillations in vacuum

In this section a brief overview over the theory of neutrino oscillations in vacuum is given. The discussion will follow the approach of *Samoil Bilenky* [12] using a simplified version<sup>3</sup>.

The theory of neutrino oscillations bases on the idea of neutrinos being particles with non-vanishing rest masses. The approach to give mass to neutrinos in local quantum field theory results in the theoretical predication that the left-handed flavor neutrino fields,  $\nu_{l,L}(x)$  with  $l \in \{e, \nu, \tau\}$ , taking part in the weak interactions of the SM are not necessarily equal to the fields of left-handed neutrinos with definite mass  $\nu_{i,L}(x)$ . Instead, the flavor fields are mixtures of the fields of massive neutrinos,

$$\nu_{l,L}(x) = \sum_i U_{li} \nu_{i,L}(x), \quad (2.1)$$

where  $U_{li}$  is a unitary mixing matrix. If the mixing matrix is not the identity matrix, neutrinos change their flavor in an oscillating way.

The mechanism of mass generation for neutrinos is not known. Current theory offers two different possibilities:

- Introduction of right-handed neutrino fields allows to describe neutrinos according to the Dirac equation. These Dirac neutrinos would get their mass by a Yukawa coupling to the Higgs field.
- Neutrinos are Majorana particles and thus their own anti-particles. From the Majorana condition,

$$\nu_i^c(x) = \nu_i(x), \quad (2.2)$$

with  $\nu_i^c(x)$  as the conjugated field, follows that right-handed flavor neutrino fields can be replaced by charge conjugated, left-handed flavor neutrino fields in neutrino mass terms. As a consequence lepton number is no longer conserved.

In general, the unitary  $n \times n$  mixing matrix  $U$  can be characterized by  $n_\theta = \frac{n(n-1)}{2}$  angles and  $n_\phi = \frac{n(n+1)}{2}$  phases. The number of physically relevant phases is smaller. As the mixing

<sup>1</sup>SSM: Standard Solar Model

<sup>2</sup>SNO: Sudbury Neutrino Observatory

<sup>3</sup>A complete derivation requires usage of the wave packet formalism.

matrix enters CC<sup>1</sup> in combination with lepton fields, some of the phases can be used for a global phase transformation of the lepton fields without physical effects. Thereby the number of relevant phases decreases to  $n_\phi^D = \frac{(n-1)(n-2)}{2}$  in the Dirac case and to  $n_\phi^M = \frac{n(n-1)}{2}$  in the Majorana case as some of the phases are fixed by the Majorana condition (Equation 2.2). In the following discussion only three active neutrino flavors will be considered for neutrino oscillations. Possible sterile neutrinos will be neglected. The resulting  $3 \times 3$  mixing matrix is given by the PMNS<sup>2</sup> matrix with the following standard parameterization:

$$U = \begin{pmatrix} 1 & 0 & 0 \\ 0 & c_{23} & s_{23} \\ 0 & -s_{23} & c_{23} \end{pmatrix} \begin{pmatrix} c_{13} & 0 & s_{13} e^{-i\delta} \\ 0 & 1 & 0 \\ -s_{13} e^{i\delta} & 0 & c_{13} \end{pmatrix} \begin{pmatrix} c_{12} & s_{12} & 0 \\ -s_{12} & c_{12} & 0 \\ 0 & 0 & 1 \end{pmatrix} \cdot V, \quad (2.3)$$

with the denotations  $s_{ij} \equiv \sin \theta_{ij}$ ,  $c_{ij} \equiv \cos \theta_{ij}$  and the matrix  $V = \text{diag}(e^{i\alpha_1/2}, e^{i\alpha_2/2}, 1)$ . The matrix  $V$  with the Majorana phases  $\alpha_i$  is only required in case the neutrino is a Majorana particle. As these additional phases do not affect oscillations physics, but contribute to lepton number violating processes like neutrinoless double beta decay, they will be omitted from now on.

In order to determine the time evolution of a quantum state in quantum field theory the time dependent Schrödinger equation has to be solved. In the subsequent discussion natural units<sup>3</sup> are used. Transition matrix elements of weak interaction processes are calculated with the flavor eigenstate  $|\nu_l\rangle$  of the neutrino. Eigenstates of the Hamiltonian  $H$ , and thus of the time evolution operator  $e^{-iHt}$  describing the neutrino's propagation, are the neutrino mass eigenstates  $|\nu_i\rangle$  with energy eigenvalues  $E_i$ . They are connected by the mixing matrix  $U$ :

$$|\nu_l\rangle = \sum_{i=1}^3 U_{li}^* |\nu_i\rangle, \quad (2.4)$$

where  $U_{li}^*$  changes to  $U_{li}$  in the case of anti-neutrinos. To determine the probability  $P(l \rightarrow l')$  at time  $t$  to detect the flavor eigenstate  $|\nu_{l'}\rangle$  from the propagated initial eigenstate  $|\nu(t)\rangle$ ,  $|\nu(t=0)\rangle = |\nu_l\rangle$ , the squared modulus of the transition amplitude has to be calculated:

$$P(l \rightarrow l') = |\langle \nu_{l'} | \nu(t) \rangle|^2 = \left| \sum_{i=1}^3 U_{l'i} e^{-iE_i t} U_{li}^* \right|^2 \quad (2.5)$$

A commonly used approximation is the assumption of ultra-relativistic neutrinos,  $v_\nu/c \approx 1$ . Hence, it follows that  $t \simeq L$ , with  $L$  being the propagated distance<sup>4</sup> of the neutrino. If one further assumes that  $m_i \ll |\mathbf{p}_i|$  and that all mass eigenstates have the same momentum,  $\mathbf{p}_i = \mathbf{p} \forall i$ , the different energy eigenvalues of the mass eigenstates can be expressed in terms

<sup>1</sup>CC: Charged Current

<sup>2</sup>PMNS: Pontecorvo–Maki–Nakagawa–Sakata

<sup>3</sup> $\hbar = c = 1$

<sup>4</sup>Often referred to as "baseline", especially in case of distinct neutrino sources and detectors like in accelerator experiments.

of neutrino momentum and mass:

$$E_i = \sqrt{\mathbf{p}_i^2 + m_i^2} \approx |\mathbf{p}| + \frac{m_i^2}{2|\mathbf{p}|} \approx E + \frac{m_i^2}{2E} \quad (2.6)$$

Using Equation 2.6, Equation 2.5 can be written as follows:

$$\begin{aligned} P(l \rightarrow l') = & \delta_{l,l'} - 4 \sum_{i>k} \Re(U_{li}^* U_{l'i} U_{lk} U_{l'k}^*) \sin^2 \left( \frac{\Delta m_{ik}^2 L}{4E} \right) + \\ & + 2 \sum_{i>k} \Im(U_{li}^* U_{l'i} U_{lk} U_{l'k}^*) \sin \left( \frac{\Delta m_{ik}^2 L}{2E} \right), \end{aligned} \quad (2.7)$$

with  $\Delta m_{ik}^2 = m_i^2 - m_k^2$ . Three points are important to realize:

- The matrix elements  $U_{lk}$  determine the oscillation amplitude while the difference of squared masses  $\Delta m_{ik}^2$  affects the oscillation frequency. The ratio of the adjustable parameters baseline  $L$  and energy  $E$  in combination with  $\Delta m_{ik}^2$  allows to choose the phase of the flavor transition.
- At least one mass eigenstate must have a non-vanishing rest mass in order to make neutrino oscillations possible. Otherwise all differences of squared masses  $\Delta m_{ik}^2$  are zero and the transition probability between two different flavor eigenstates vanishes.
- If the mixing matrix  $U$  is not a real matrix, i. e.  $\delta \neq 0$ , CP invariance is violated in the leptonic sector. As a consequence, neutrinos and anti-neutrinos oscillate differently:  $P(\nu_l \rightarrow \nu_{l'}) \neq P(\bar{\nu}_l \rightarrow \bar{\nu}_{l'})$

## 2.3 Neutrino oscillations in matter

If one considers neutrinos propagating through matter, physics of oscillations changes as it was first shown by *Lincoln Wolfenstein* [13]. Neutrino oscillations in matter are subject of this section, sticking closely to the explanations given by *Samoil Bilenky* [12].

The neutrino evolution equation in vacuum in the flavor representation is given by

$$i \frac{\partial a(t)}{\partial t} = U \frac{m^2}{2E} U^\dagger a(t), \quad (2.8)$$

where  $a(t)$  denotes the probability amplitude. It can be deduced from the Schrödinger equation with the free Hamiltonian  $H_0$  by expanding over the states of flavor neutrinos and taking Equation 2.4 into account. The kinetic term does not affect oscillation and can be excluded from the Hamiltonian by a redefinition of a common phase of the wave function. If one considers neutrino propagation in matter, Equation 2.8 has to be modified due to effects of neutrino interactions with constituents of matter. Normal matter consists of electrons, protons and neutrons. These particles can interact with neutrinos through CC and NC<sup>1</sup> interactions, which yield additional contributions  $H_{\text{int}}$  to the effective Hamiltonian  $H_{\text{eff}} = H_0 + H_{\text{int}}$ . The

<sup>1</sup>NC: Neutral Current

most important effect is the coherent forward scattering of neutrinos, which does not change the state of matter. One can deduce, that the contributions of electrons and protons to the effective Hamiltonian due to NC interactions cancel each other for all neutrino flavors in neutral matter. The remaining contribution from neutrons is equal for all neutrino flavors and thereby cannot affect flavor change. It can be removed from the total Hamiltonian by a phase transformation of the wave function. CC interactions can only occur between  $\nu_e$  and the electrons of matter and create an additional effective potential for these neutrinos. Therefore, the evolution equation of neutrino in matter becomes

$$i \frac{\partial a(t)}{\partial t} = \left( U \frac{m^2}{2E} U^\dagger \pm \sqrt{2} G_F n_e(t) \beta \right) a(t), \quad (2.9)$$

with the Fermi constant  $G_F$  and  $n_e(t)$  being the matter's time-dependent electron density.  $\beta_{\nu_e; \nu_e} = 1$ , all remaining elements of the matrix  $\beta$  are equal to zero. If constant matter density is assumed,  $n_e(t) = n_e$ , the interaction Hamiltonian  $H_{\text{int}}$  becomes time independent and the evolution equation can be solved easily by diagonalizing the total Hamiltonian. One finds that the probability of a transition  $\nu_l \rightarrow \nu_{l'}$  in matter has the same form as a transition in vacuum (see Equation 2.5):

$$P^m(l \rightarrow l') = \left| \sum_i U_{l'i}^m e^{-i E_i^m (t-t_0)} U_{li}^{m*} \right|^2 \quad (2.10)$$

$t_0$  is the point in time when the neutrino is created and oscillation starts. The matrix  $U^m$  describes the connection between the flavor eigenstates and the new mass eigenstates in matter with eigenvalues  $E_i^m$ . Looking at a much simpler case with only two neutrino flavors, the effective mixing angle  $\theta^m$  and the effective difference of squared masses  $\Delta m_m^2$  in matter are related to the vacuum quantities  $\theta$  and  $\Delta m^2$  the following way:

$$\sin(2\theta^m) = \frac{\Delta m^2 \sin(2\theta)}{\sqrt{(\Delta m^2 \cos(2\theta) - A)^2 + (\Delta m^2 \sin(2\theta))^2}}, \quad (2.11)$$

$$\Delta m_m^2 = \sqrt{(\Delta m^2 \cos(2\theta) - A)^2 + (\Delta m^2 \sin(2\theta))^2}, \quad (2.12)$$

with  $A = 2 \sqrt{2} G_F n_e E$ . Both quantities are maximal if

$$A = \Delta m^2 \cos(2\theta). \quad (2.13)$$

This equation is called the MSW<sup>1</sup> resonance condition. The issue of neutrino oscillations in matter becomes more complicated if one considers variable matter density.

## 2.4 Measurement of mixing parameters

Mixing angles of the PMNS mixing matrix and the differences of squared masses are subject to measurements in neutrino oscillation experiments. In a simplified picture, the measuring

<sup>1</sup>MSW: Mikheyev–Smirnov–Wolfenstein

principle for identifying the parameters relies on comparison of experimentally determined oscillation probabilities, basing on event rates for distinct neutrino flavors, with probabilities predicted by oscillation theory. The result of a measurement is a set of mixing parameters which fits the experimental data best and holds constraints from other experiments at the same time.

One distinguishes two variants of oscillation search using transition probabilities between neutrino flavors: In disappearance experiments the survival probability  $\nu_l \rightarrow \nu_l$  of a distinct neutrino flavor is investigated, while appearance experiments search for the probability to find a resulting neutrino flavor of a flavor state transition,  $\nu_l \rightarrow \nu_{l'}$ ,  $l \neq l'$ . Both variants depend differently on the mixing parameters. The same holds for oscillation probabilities with different combinations for the neutrino flavors  $l$  and  $l'$ . Concurrently, invariance conditions force equality of probabilities [14]:

$$\begin{aligned} \text{T} &: \text{P}(\nu_l \rightarrow \nu_{l'}) = \text{P}(\nu_{l'} \rightarrow \nu_l) , \quad \text{P}(\bar{\nu}_l \rightarrow \bar{\nu}_{l'}) = \text{P}(\bar{\nu}_{l'} \rightarrow \bar{\nu}_l) , \\ \text{CP} &: \text{P}(\nu_l \rightarrow \nu_{l'}) = \text{P}(\bar{\nu}_l \rightarrow \bar{\nu}_{l'}) , \\ \text{CPT} &: \text{P}(\nu_l \rightarrow \nu_{l'}) = \text{P}(\bar{\nu}_{l'} \rightarrow \bar{\nu}_l) , \end{aligned}$$

with charge conjugation C, parity transformation P and time inversion T. Vice versa, a measurement of the probabilities can be used to verify validity of the invariances, especially of CP conservation.

### 2.4.1 Present knowledge on mixing parameters

As probability of oscillation depends on more than one parameter, a single experiment is insufficient to determine all mixing parameters at once and therefore relies on results from other experiments. By choosing cleverly the adjustable parameters neutrino energy (spectrum) and source–detector–distance (baseline), the impact of some mixing parameters on the oscillation probability is negligible. Thereby, leading order measurements are possible for dominant parameters, which are easier to analyze. Sometimes even a two-neutrino analysis is done.

An analysis of the global data from neutrino oscillation experiments yields the following best fit values for the mixing parameters at  $1\sigma$  CL assuming a normal mass hierarchy (see below) [15] [16]:

$$\begin{aligned} \Delta m_{21}^2 &= 7.59_{-0.18}^{+0.20} \times 10^{-5} \text{ eV}^2 \\ |\Delta m_{31}^2| &= 2.50_{-0.16}^{+0.09} \times 10^{-3} \text{ eV}^2 \\ \sin^2 \theta_{12} &= 0.312_{-0.015}^{+0.017} \\ \sin^2 \theta_{23} &= 0.52_{-0.07}^{+0.06} \\ \sin^2 \theta_{13} &= 0.013_{-0.005}^{+0.007} \\ \delta_{CP} &= (-0.61_{-0.65}^{+0.75}) \pi \end{aligned}$$

### 2.4.2 Current issues of neutrino oscillations physics

Some issues of neutrino physics still need to be addressed by running and future neutrino (oscillation) experiments.

**Majorana / Dirac neutrino** The answer to the question whether neutrinos are Majorana or Dirac particles cannot be given by oscillation experiments as they are insensitive to the Majorana phases. However, this issue could be solved by experiments looking for neutrinoless double beta decay [12].

**Precision measurement of mixing parameters** The mixing parameters are currently known with a precision of a few percent. Therefore, future oscillation experiments must aim to do precision measurements by being sensitive enough for next-to-leading-order effects. Furthermore, these measurements strongly depend on the outcome of the search for sterile neutrinos. Although they cannot be detected by direct interaction with matter, their existence would allow further oscillation channels for flavor neutrinos and thereby challenge unitarity of the  $3 \times 3$  PMNS matrix. At the same time, the uncertainties on neutrino interaction cross-sections must be decreased by a specific measurement as they have a major impact on systematic errors of current oscillation experiments.

**Mass hierarchy / Absolute mass scale** The phenomenon of neutrino oscillations bases on the existence of at least one non-zero neutrino mass eigenvalue. Oscillation experiments are only sensitive to the differences of squared masses. In case of three-neutrino oscillations three differences of squared mass exist with two of them being independent. Former experiments determined one of the differences to be much larger than the other, but the hierarchy of the masses is unclear. The separated mass eigenstate  $\nu_3$  with the large difference to the mass doublet  $\nu_1, \nu_2$  can have a larger (normal hierarchy) or smaller (inverted hierarchy) absolute mass than the doublet states. Furthermore, the absolute mass scale for neutrinos is unknown. The Troitzk and Mainz experiments yielded an upper limit of  $m_{\bar{\nu}_e} < 2.3 \text{ eV}$  at 95 % CL [14]. The future KATRIN<sup>1</sup> experiment aims for a sensitivity of  $m_{\bar{\nu}_e} < 0.2 \text{ eV}$  [17].

**$\theta_{13}$  &  $\delta_{CP}$**  Former reactor and accelerator experiments only yielded an upper limit for the mixing angle  $\theta_{13}$ . The most stringent comes from the reactor experiment CHOOZ with  $\sin^2(2\theta_{13}) < 0.19$  at 90 % C.L.<sup>2</sup> [14]. However, recent results from the T2K<sup>3</sup> accelerator experiment [18] suggest a non-zero value of  $0.03$  ( $0.04$ )  $< \sin^2(2\theta_{13}) < 0.28$  ( $0.34$ ) at 90 % CL for normal (inverted) mass hierarchy [19]. So far, almost nothing is known about the phase  $\delta_{CP}$ . This parameter is only measurable if  $\theta_{13}$  is confirmed to be non-zero. While a short-baseline reactor experiment can perform a clear measurement on  $\theta_{13}$  without competing matter effects, it is insensitive to CP violation.

### 2.4.3 Contributions from a neutrino beam experiment

In order to solve the issues concerning mass hierarchy,  $\theta_{13}$  and  $\delta_{CP}$  a neutrino beam experiment with baseline  $L$  and neutrino energy  $E$  using  $\nu_\mu \rightarrow \nu_e$  and  $\bar{\nu}_\mu \rightarrow \bar{\nu}_e$  appearance would

<sup>1</sup>KATRIN: Karlsruhe Tritium Neutrino

<sup>2</sup>for  $\Delta m^2 = 2 \times 10^{-3} \text{ eV}^2$

<sup>3</sup>T2K: Tokai-to-Kamioka

contribute valuable information. An approximated analytical expression for the transition probability  $P_{\mu e}$  to second order in the small quantities  $\theta_{13}$  and  $\alpha \equiv \Delta m_{21}^2/\Delta m_{31}^2$  is given by [20]:

$$\begin{aligned}
P_{\mu e} \simeq & \underbrace{\sin^2 \theta_{23} \sin^2 2\theta_{13} \frac{\sin^2[(1-\hat{A})\Delta]}{(1-A)^2}}_{C_0} + \alpha^2 \underbrace{\cos^2 \theta_{23} \sin^2 2\theta_{12} \frac{\sin^2(\hat{A}\Delta)}{\hat{A}^2}}_{C_1} \\
& \mp \alpha \underbrace{\sin 2\theta_{13} \cos \theta_{13} \sin 2\theta_{12} \sin 2\theta_{23} \sin(\Delta) \frac{\sin(\hat{A}\Delta)}{\hat{A}} \frac{\sin[(1-\hat{A})\Delta]}{(1-\hat{A})}}_{C_-} \sin \delta_{CP} \\
& + \alpha \underbrace{\sin 2\theta_{13} \cos \theta_{13} \sin 2\theta_{12} \sin 2\theta_{23} \cos(\Delta) \frac{\sin(\hat{A}\Delta)}{\hat{A}} \frac{\sin[(1-\hat{A})\Delta]}{(1-\hat{A})}}_{C_+} \cos \delta_{CP},
\end{aligned} \tag{2.14}$$

with

$$\Delta \equiv \frac{\Delta m_{31}^2 L}{4E}, \quad \hat{A} \equiv \frac{A}{\Delta m_{31}^2}, \quad A = \pm 2\sqrt{2}G_F n_e E$$

Equation 2.14 assumes constant matter density. The upper sign of matter potential  $A$  and term  $C_-$  corresponds to neutrinos and the lower sign to anti-neutrinos. Term  $C_0$  is most sensitive to Earth matter effects and therefore can be used to measure the sign of  $\Delta m_{31}^2$ . It can also be used to obtain information on  $\theta_{13}$ . CP-violating contributions come from term  $C_-$ . Although  $C_+$  depends on  $\theta_{13}$  and  $\delta_{CP}$  it is CP-conserving. The second term  $C_1$  depends only on the solar mixing parameters  $\theta_{12}$  and  $\Delta m_{21}^2$ . More details on oscillation search with a neutrino beam experiment are given in Chapter 4.

#### 2.4.4 Degeneracies in neutrino beam experiments

A transition probability can be composed as a product of several mixing parameters and therefore a measurement yields ambiguous results for the parameters. Two sets of parameters fitting the experimental results and at the same time holding constraints from other experiments represent degenerate solutions. Degeneracies complicate exact determination of the mixing parameters in a neutrino beam experiment. They can even mix a CP-violating set with a CP-conserving set of parameters. A partial solution is possible by choosing the adjustable parameters neutrino energy  $E$  and base-line  $L$  appropriately, but some require multiple measurements with different choices for  $L$  and  $E$  to solve them. Considerable two-fold degeneracies are summarized below [21]. Together they form an eight-fold degeneracy.

**$\delta_{CP}$  -  $\theta_{13}$  degeneracy:** Both mixing parameters,  $\delta_{CP}$  and  $\theta_{13}$ , always appear in combination due to the structure of the PMNS matrix (see Equation 2.3). The ambiguity can be solved by choosing the ratio  $L/E$  properly.

**$\text{sgn}(\Delta m_{31}^2)$  degeneracy:** The mass hierarchy and thus the sign of  $\Delta m_{31}^2$  is unknown. Two parameter sets with different hierarchies can yield the same probability. Great matter effects implicating a long baseline can solve the degeneracy.

**$\theta_{23}$  ,  $\pi/2 - \theta_{23}$  degeneracy:** A measurement of the  $\nu_\mu$  survival probability only determines  $\sin^2 2\theta_{23}$ . The degeneracy exists only if  $\theta_{23}$  deviates from the preferred value of  $\theta_{23} \approx \pi/4$  from atmospheric data. In order to solve the degeneracy, a comparison of different oscillation channels, like  $P(\nu_e \rightarrow \nu_\tau)$  and  $P(\nu_e \rightarrow \nu_\mu)$ , is necessary.



## Chapter 3

# The LENA experiment

The LAGUNA project is the joint European effort to plan and build a next generation neutrino observatory, which is foreseen to solve current issues in particle and astro-particle physics related to neutrinos. LENA is a 50 kt liquid scintillator detector and one possible option in LAGUNA.

General information regarding the European project are given in Section 3.1. Design of the LENA detector is topic of Section 3.2, whereas its research program is discussed in Section 3.3.

### 3.1 Large Apparatus for Grand Unification and Neutrino Astrophysics

The search for physics beyond the SM of particle physics, like GUTs<sup>1</sup> for unification of strong, weak and electromagnetic interaction, and the answering of important questions from astro-particle physics and cosmology relies heavily on detection and investigation of rare events, interactions with very small cross-sections and signal sources with low fluxes. In order to compensate for these difficult measurement conditions, the construction of detectors with higher target masses and increasing technological complexity is inevitable, as it is the only way to get statistical significant results after a reasonable amount of time. Furthermore, these detectors need to be placed underground to suppress competing influences from otherwise dominant sources of cosmic background.

#### 3.1.1 LAGUNA design study

It is very unlikely, that a European country can on its own handle the financial burden, as well as deal with the challenges to develop, build and maintain such a next-generation detector. With the aim to do leading research, a careful view on international research plans for the next decades is necessary in order to to assess the best strategy [22]. For this reason, the pan-European LAGUNA project has been set up in 2008 [23][24][25].

LAGUNA is pushed by a consortium, incipiently consisting of about 100 physicists and engineers from 28 scientific institutions and several economic partners with a total of 10 different

---

<sup>1</sup>GUT: Grand Unified Theory

countries involved. The project is sponsored under the "7<sup>th</sup> Framework Programme" of the European Union. It is the aim of the project to investigate, elaborate and finally realize a European next-generation neutrino observatory with a possible target mass of several tens to hundreds of kilotons. The project's first phase was a design study focusing on the investigation of potential detector sites and excavation of the underground laboratory, which lasted from 2008 until 2011.

The following summary gives a brief overview of the considered detector technologies within LAGUNA:

**MEMPHYS** - The MEMPHYS<sup>1</sup> detector design [26] bases on the water Cerenkov technology, which is e. g. used by the Super-Kamiokande<sup>2</sup> detector [27] in Japan. The baseline design study foresees to split the target mass in three cylindrical tank modules, each of them with 65 m in height and diameter. With a fiducial mass of 146 kt per module, one ends up with a total fiducial mass of 440 kt.

**GLACIER** - A further option within LAGUNA is the GLACIER<sup>3</sup> detector [28]. The core element of the design is a liquid argon TPC<sup>4</sup> with a foreseen mass of 100 kt, which is stored in a cylindrical vessel of 20 m height and 70 m in diameter. A variant of this technology is implemented by the ICARUS<sup>5</sup> collaboration [29].

**LENA** - The design for LENA foresees a 50 kt detector of organic liquid scintillator. An overview of the detector's expected physics potential is given in Section 3.3, while important aspects of the design are summarized in Section 3.2.

All detectors need to be placed underground in order to use the rock overburden as shielding, usually measured in mwe<sup>6</sup>, from cosmic background like muons. Additionally, the performance of the different detector types as far detector in a future long-baseline oscillation experiment with a neutrino beam from CERN<sup>7</sup> is studied (see Section 3.1.2). As discussed in Chapter 2, the neutrino oscillation probability depends on the neutrino's energy and the distance between neutrino source and detector. For the different distances of considered detector location to CERN the neutrino energy to reach the first oscillation maximum varies. Table 3.1 summarizes some information on the sites investigated by LAGUNA.

### 3.1.2 LAGUNA-LBNO

The second stage of LAGUNA, LAGUNA-LBNO<sup>8</sup>, started in 2011 and will last 3 years. Within this phase it is planned to elaborate more precise underground construction plans, especially concerning the detector tank. Furthermore, the possibility to use a LAGUNA detector to investigate long-baseline neutrino oscillations with a neutrino beam from CERN to three selected sites will be studied [30]:

<sup>1</sup>MEMPHYS: Megaton Mass Physics

<sup>2</sup>Kamiokande: Kamioka Neutron Decay Experiment

<sup>3</sup>GLACIER: Giant Liquid Argon Charge Imaging Experiment

<sup>4</sup>TPC: Time Projection Chamber

<sup>5</sup>ICARUS: Imaging Cosmic and Rare Underground Signals

<sup>6</sup>mwe: meters water equivalent

<sup>7</sup>CERN: Conseil Européen pour la Recherche Nucléaire - European Organization for Nuclear Research

<sup>8</sup>LBNO: Long Baseline Neutrino Oscillations

**Table 3.1:** Selected sites for the LAGUNA design study [24].

Location	Type	Envisaged depth [mwe]	Distance from CERN [km]	Energy 1st osc. max. [GeV]
Fréjus ( <i>F</i> )	Road tunnel	$\simeq 4800$	130	0.26
Canfranc ( <i>ES</i> )	Road tunnel	$\simeq 2100$	630	1.27
Umbria ( <i>IT</i> )	Green field	$\simeq 1500$	665	1.34
Sieroszowice ( <i>PL</i> )	Mine	$\simeq 2400$	950	1.92
Boulby ( <i>UK</i> )	Mine	$\simeq 2800$	1050	2.12
Slanic ( <i>RO</i> )	Salt mine	$\simeq 600$	1570	3.18
Pyhäsalmi ( <i>FI</i> )	Mine	up to $\simeq 4000$	2300	4.65

**CN2PY:** With a distance of 2288 km, the CERN to Pyhäsalmi option includes the longest baseline of all considered LAGUNA sites. As a neutrino beam from CERN would have to propagate a long way through the Earth’s crust, this option involves distinct matter effects and thus offers opportunities to gather valuable information on the hardly known or fully unknown neutrino mixing parameters  $\theta_{13}$ ,  $\delta_{CP}$ , as well as on the neutrino mass hierarchy.

**CN2FR:** The CERN to Fréjus option includes the shortest distance of 130 km within the set of considered LAGUNA sites. As matter interference on neutrino oscillations would be negligible along this baseline, the comparison of neutrinos and anti-neutrinos from a low-energy beam would offer the determination of  $\delta_{CP}$  without competing matter effects.

**CNGS<sup>1</sup> – Umbria:** This option is considered as it would use existing neutrino beam infrastructure from the CNGS experiment, which sends a  $\nu_{\mu}$  beam from CERN to the OPERA [31] and ICARUS detectors at LNGS<sup>2</sup>. For the LAGUNA detector at Umbria a location 1° off-axis is considered, resulting in a 658 km long baseline.

## 3.2 LENA detector design

LENA is planned to be an apparatus for neutrino physics and observation based on liquid scintillator with a target mass of about 50 kt. Already existing and running experiments with the same technology, like Borexino [3] or KamLAND [4], as well as detectors of similar size, like Super-Kamiokande [27], grant valuable experience to help with the design of a next-generation detector like LENA. Nevertheless, scaling up in mass and technological improvements still offer a great challenge for detector design.

Within the upcoming sections, an overview of a possible LENA design will be given, sticking closely to the information given in the LENA white paper [32], as no final detector setup has been chosen at the time of writing. Starting with the liquid scintillator as the core element and responsible for generating the first physical information on the detected particle interaction, the description will follow the way of information flow to the hardware responsible

<sup>2</sup>LNGS: Laboratori Nazionali del Gran Sasso

for detection of scintillation light and proceed with remarks regarding solutions for readout electronics. Finally, some information regarding the housing of the detector components in a tank structure will be given.

### 3.2.1 Liquid scintillator

Detection of a particle is based on an electromagnetic interaction between the particle and the active detector material. Neutrinos are uncharged particles only participating in the weak interaction and can thus only be detected if they produce charged particles in CC and NC reactions. In the case of LENA, the active detector material is given by 50 kt of liquid scintillator. Different CC and NC detection channels for neutrinos are described in Section 3.3 and in Section 4.1.3. The functionality of liquid scintillator to detect charged particles is explained in the following.

The process of scintillation describes the behavior of materials to transform atomic excitation energy, induced by electromagnetic interaction of charged particles, into ultraviolet or visible light through de-excitation. Thus, the property of luminescence is essential for these kinds of material. One differs fluorescence processes, where the de-excitation takes place typically  $\tau \approx 10^{-9} - 10^{-8}$  s after the exciting interaction, from phosphorescence processes with time scales of  $10^{-6}$  s or more [33].

Application of scintillators is widely spread in detector construction for particle physics [34]. The ability to convert kinetic energy of charged particles into light makes them ideal for calorimetric purposes: As a charged particle propagates through scintillating matter, it interacts with the surrounding molecules and atoms electromagnetically. Thereby, it transfers its kinetic energy to the scintillator along the particle's path. For heavier charged particles, like protons and alphas, the energy deposition per unit length can be described by the formula of Bethe-Bloch [34].

In liquid scintillator about 5 % of the transferred energy is isotropically emitted in the form of scintillation light. Due to the fact that several de-excitation modes are possible, a scintillator pulse has more than one radiative decay constant and its shape can be described by a superposition of several exponential decay functions:

$$n(t) = \sum_i n_i e^{-\frac{t}{\tau_i}}, \quad (3.1)$$

where  $\tau_i$  is the fluorescence time of a possible decay process and  $n_i$  its amplitude. The correlation between the amount of deposited energy per unit length  $dE/dx$  and the number of emitted scintillation photons per unit length  $dL/dx$  is in general not linear. In case the penetrating particle is not minimum ionizing, the number of degrees of freedom for scintillation light production is locally not sufficient for a total conversion of the deposited energy to photons. Thereby the light output is reduced. An approximation for this quenching is given by the semi-empirical Birks' formula:

$$\frac{dL}{dx} = \frac{A \frac{dE}{dx}}{1 + k_B \frac{dE}{dx}}, \quad (3.2)$$

with a normalization constant  $A$  and the Birks constant  $k_B$ .

In case the scintillator consists of only a single component, the emission and absorption spectra show a significant overlap, resulting in re-absorption processes. This way, a considerable part of timing and energetic information gets lost. In order to minimize these internal losses, one or more organic solutes are added to the scintillation solvent, functioning as wavelength shifters. Molecules of these solutes gain excitation energy by non-radiative interactions with the solvent, which is afterwards released as light. As this light has a higher wavelength, the scintillator becomes transparent to the wavelength shifted scintillation light.

For the LENA experiment approximately 50 kt of organic liquid scintillator are foreseen as primary detector material. Due to the large target mass, which needs to be stored in a volume of appropriate dimensions, and the experiment's goal to measure rare physical effects with high precision, a careful selection of the scintillating liquid with a view to its characteristic properties is very important:

- In order to conduct precision measurements, a high energy resolution and a low energy threshold are necessary. For this reason, the optical transparency to the scintillation light should be maximal while absorption reduces the photon count and therefore energy resolution. Scattering diminishes spatial and time resolution. The importance of this point becomes further enhanced, if one considers the large dimensions of the detector and the resulting long distances the scintillation light has to cover.
- For low energy applications, like detection of  $\bar{\nu}_e$  from supernovae, the channel called "inverse beta decay",  $\bar{\nu}_e + p \rightarrow n + e^+$ , is preferred. Therefore, an organic liquid with a high fraction of free protons is favorable.
- The scintillation light does not only contain information regarding the deposited energy, but also on the time and spatial structure of an event. Position reconstruction codes rely mostly on the time of flight of the detected photons [5]. In order to obtain good spatial resolution, the liquid scintillator has to be fast, meaning that fluorescence time has to be short. This becomes even more important, if one attempts to reconstruct particle tracks in high-energy applications.

Two possible solvents currently under discussion are LAB<sup>1</sup> (C<sub>18</sub>H<sub>30</sub>) and PXE<sup>2</sup> (C<sub>16</sub>H<sub>18</sub>). LAB is advantageous with respect to PXE regarding the number of free protons, attenuation and scattering length. Adding Dodecane (C<sub>12</sub>H<sub>26</sub>) to PXE will enhance proton number and optical transparency while diminishing timing properties and light yield. Furthermore, scintillators based on PXE are faster than LAB, as the decay constant is smaller while the weight of the fast pulse component is larger. With a view to high-energy applications, a fast scintillator, and thus PXE, is favorable. An alternative is to increase the concentration of wavelength shifters in LAB, which speeds up the non-radiative energy transport to the light-emitting centers.

---

<sup>1</sup>LAB: Linear Alkylbenzene

<sup>2</sup>PXE: Phenyl-o-xylylethane

### 3.2.2 Light detection and readout electronics

In order to extract the physical information on the particle interactions from the scintillation signal, two steps are necessary to gain data in digital form for further processing and analysis. First of all, the scintillation light photons are detected by conversion to photo electrons and amplified into a measurable analogue signal. This task is taken on by photosensors, with bialkali PMTs<sup>1</sup> being the most sophisticated variant.

The overall efficiency for light detection is determined by two factors:

- The OC<sup>2</sup> defines the fraction of the detector's surface covered by photosensors. In the current design an OC of 30 % is intended.
- The photo detection efficiency of the photosensor is related to the efficiencies of single components of the photosensor, mostly the quantum efficiency of the photocathode. A value of 20 % is assumed to be a baseline for LENA, a conservative estimate for current PMTs.

Therefore, the overall efficiency for light detection is 6 %.

The number of PMTs necessary to reach the designated OC primarily depends on the diameter of the photocathode. Possible diameters currently under consideration and investigation range from 3 inch to 20 inch. Characteristics of the corresponding PMTs like dark count, dynamic range and pressure resistance are taken into account. For tracking particles in the high-energy domain, a fine granularity of the entire light detection surface is advantageous due to improved spatial and time reconstruction capabilities. At the same time, the demand for a high dynamic range of the sensors vanishes, as the expected number of photo electrons per PMT is reduced compared to sensors with larger diameters. There are ways to increase the light collection per PMT, that would lead to a reduction of the total number of photosensors without decreasing the overall light detection efficiency. Among these is the Winston cone. These reflecting cones deflect incoming photons, which would have missed the sensor without the cone, to concentrate them on the photosensitive area. Thereby the effective area for light incidence from the front of a PMT is increased, while photons with too high incident angles are reflected.

After the detected light has been transformed into an analogue signal by photosensors, further processing of the gathered information is required to store the relevant data in digital form for analysis. For this step appropriate readout electronics are necessary. In order to make full use of the detector's scientific potential, a signal readout consisting of FADCs<sup>3</sup> recording the full pulse shapes of individual PMTs tends to be the best solution. Especially in the case of high-energy interactions, a sampling rate of 1-2 GS/s<sup>4</sup> and an appropriate voltage resolution would help to investigate the time evolution of an event and thus support particle tracking and identification through valuable timing information. In addition, the electronics and a good trigger architecture have to make sure that the amount of data assigned for

---

<sup>1</sup>PMT: Photomultiplier tube

<sup>2</sup>OC: Optical coverage

<sup>3</sup>FADC: Fast Analogue-to-Digital Converter

<sup>4</sup>GS: Giga-samples

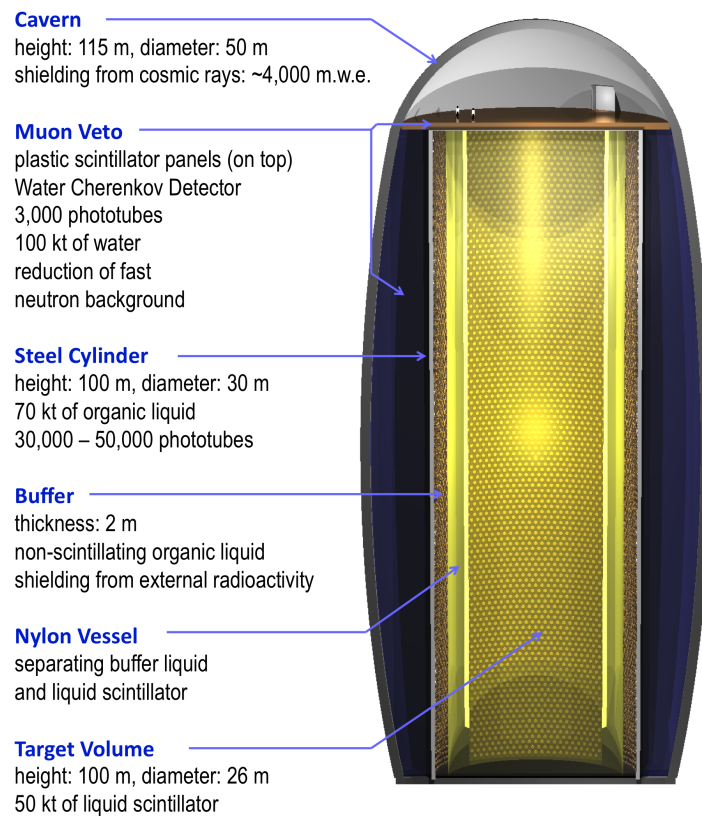


**Figure 3.1:** Vertical section of the LENA detector with its different volumes [32]. The curved cavern wall originates from the Pyhäsalmi design for better resistance against the outer pressure from the surrounding rock.

storage is as low as possible. Therefore, dark noise from the PMTs has to be suppressed as good as possible without losing important information. At the same time the FADC DAQ<sup>1</sup> must be capable to handle the high event rates induced by a possible galactic supernova neutrino burst, without being "blinded" by neutrino interaction events in the scintillator.

### 3.2.3 Detector tank and laboratory site

The active detector components mentioned above are contained in a safe and stable tank structure encapsulating the liquids without leakage and holding the PMTs. A schematic view of the entire *LENA* detector with its different volumes is shown in figure 3.1 .

The detector's cylindrical core volume is 100 m high and 26 m in diameter. It comprises the target mass of about 50kt of organic liquid scintillator. A thin nylon vessel separates the fiducial volume from a second, 2 m thick layer of organic, non-scintillating liquid. This buffer volume provides shielding from external radioactivity. An outer tank structure encloses the inner organic liquids and provides structural stability, as well as the capabilities to mount PMTs and to install necessary electronics and power supply lines. The entire tank is placed in an underground cavern. In order to reduce background from fast neutrons, 100 kt of

<sup>1</sup>DAQ: Data acquisition

water are planned to fill the gap between the outer tank and the walls of the cavern. PMTs mounted at the outside of the tank will make the water volume a Cherenkov detector for cosmic muons and therefore provide veto functionality, which is further extended by plastic scintillator panels on top of the detector. For the construction of the tank vessel two types of materials are possible: steel and concrete. A concrete tank is low in costs and would do better in resisting compression forces arising from density differences between water and scintillator, but suffers from higher intrinsic radioactivity. To compensate the intrinsic radioactivity, an increase of the inner volume would be necessary to obtain the same fiducial volume for low-energy applications as with a steel tank.

Although seven different locations in Europe are under research regarding their suitability to support a future LAGUNA-type detector, LENA requires adequate environmental conditions to unfold its full physics potential. Due to the large dimensions of any considered detector type, no underground laboratory in Europe is currently capable to house such an extensive structure. Therefore excavation works are inevitable. In addition, LENA depends on a strong shielding from cosmic muons of at least 4000 mwe above the detector to conduct its research in the low-energy domain without too much interference from cosmic background. Thereby the number of acceptable locations for LENA is reduced from seven to two:

**Pyhäsalmi** - In this scenario the LENA detector would be placed 1450 m below ground in the currently deepest mine in Europe, the Pyhäsalmi mine in Finland [35]. The mine, which is planned to be operational at least until 2018, already offers good infrastructural conditions like transportation connections via rail and road, as well as underground supply lines that could be used to construct and run LENA. The background levels, most important for the low-energy physics program, are as follows:

Radioactivity by radon	20 Bq/m <sup>3</sup>
Muon flux	$1.1 \times 10^{-4} / \text{m}^2 \text{s}$
Expected reactor $\bar{\nu}_e$ background	$1.9 \times 10^5 / \text{cm}^2 \text{s}$

**Table 3.2:** Background levels of the Pyhäsalmi mine in Finland. The next nuclear power plant is 350 km away. Two more are planned in the next decades.

**Fréjus** - In this case the LSM<sup>1</sup> would be used to house the LENA detector [36]. The laboratory is located next to the Fréjus road tunnel in the French-Italian Alps. The direct road connection could be used for transportation of materials during the construction phase of the detector. With a rock overburden of 4800 mwe from the Fréjus mountain this site offers the best shielding capabilities of all locations studied by LAGUNA. The background levels are summarized below:

While Fréjus offers better shielding from cosmic rays, Pyhäsalmi is favorable in terms of the reactor background for  $\bar{\nu}_e$  detection.

---

<sup>1</sup>LSM: Laboratoire Souterrain de Modane

Radioactivity by radon	15 Bq/m <sup>3</sup>
Muon flux	$5.0 \times 10^{-5} / \text{m}^2 \text{s}$
Expected reactor $\bar{\nu}_e$ background	$1.6 \times 10^6 / \text{cm}^2 \text{s}$

**Table 3.3:** Background levels of the LSM [32]. The nearest nuclear power plant is in France with a distance of about 130 km.

### 3.3 Physics potential of LENA

The liquid scintillator detector LENA is one option within the LAGUNA project for a next-generation neutrino observatory. Compared to the competing water Cherenkov and liquid argon detector technologies, organic liquid scintillator technology features some remarkable characteristics, which make it well-suited for research in the low-energy domain from  $\sim 200$  keV to some tens of MeV. But also for energies in the range of several hundreds of MeV to some GeV LENA is expected to have formidable potential. Within the following sections some basic information regarding key points of LENA’s research potential are discussed. The basic overview starts out with some topics from the low-energy domain and goes out to cover physics at higher energies.

#### 3.3.1 Solar neutrinos

The Sun is the closest extraterrestrial neutrino source to Earth, which produces a permanent neutrino flux of about  $6.5 \times 10^{10} \text{ m}^{-2} \text{ s}^{-1}$ . In a sequence of fusion processes in the Sun’s core, the dominant pp-chain<sup>1</sup> and the CNO-cycle<sup>2</sup>, new atomic nuclei, photons and neutrinos are produced [37]. The spectrum of solar neutrinos according to the predictions of the SSM is shown in Figure 3.2.

While photons diffuse from the core to the surface at a time scale of thousands of years due to interactions with the dense solar matter, neutrinos can leave the Sun more or less immediately. A detection of these solar neutrinos allows to extract important information on the state and the processes in the Sun’s interior, which are decisive for validation of the SSM, developed since 1963 by *John N. Bahcall* and others [10][38]. Since the pioneering chlorine experiment by *Raymond Davis Jr.* in the Homestake-mine in the late 1960s [9], neutrinos from the Sun have been subject to intensive research. Thereby, valuable insights have been gained, not only on the Sun itself, but also on the properties of the neutrinos. All experiments reported a significant deficit in the measured neutrino rate. The results of the SNO experiment [39] finally resolved the Solar Neutrino Problem (see Section 2.1) by confirmation of the predictions from the theory of neutrino oscillations [11].

Although former and still running experiments like SNO, Super-Kamiokande, Borexino, or the reactor experiment KamLAND provided valuable data to verify the SSM and to set limits on the solar mixing parameters, a high-statistics detector like LENA can still grant further insight into the nature of solar neutrinos. Compared to Borexino, event rates will increase

<sup>1</sup>pp: Proton-Proton fusion; 98.4 % of the Sun’s total energy release

<sup>2</sup>CNO: Carbon-Nitrogen-Oxygen fusion cycle; 1.6 % of the Sun’s total energy release

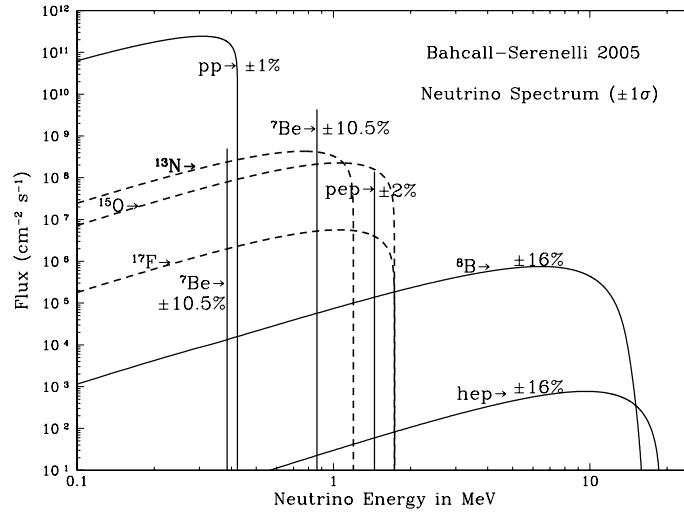


**Figure 3.2:** Spectrum of the solar neutrinos according to the predictions of the SSM [38]. The solid lines show neutrinos from the pp-chain while the dashed lines show the contributions from the CNO-cycle.

by more than two orders of magnitude, increasing the accuracy in the determination of pep<sup>1</sup>- and <sup>8</sup>B-neutrinos. Due to the great depth, background conditions for CNO-neutrinos will be more favorable. The high statistics of  $\sim 10^4$  per day for <sup>7</sup>Be-neutrinos offers the opportunity to search for time variations in the solar neutrino flux. CC interactions on <sup>13</sup>C provide a way for a precise energy-dependent measurement of the  $\nu_e$  survival probability.

### 3.3.2 Supernova neutrinos and Diffuse Supernova Neutrino Background

The evolution of a dying star to its final stage can proceed in various ways and is heavily affected by its mass. While stars with a comparable small mass evolve to a red giant and finally to a white dwarf, more massive stars, with eight or more solar masses<sup>2</sup>, lead to a tremendous explosion, a SN<sup>3</sup>. Due to the enormous amounts of released energy, approximately  $3 \times 10^{53} \text{ erg} = 3 \times 10^{46} \text{ J}$  [40], the SN is one of the most spectacular events which can be observed for a single star. There are different kinds of SNe, which are classified according to spectral types and base on varying mechanisms of formation. One of these kinds is the core-collapse SN, which occurs to stars above eight solar masses, comprises the spectral types II, Ib and Ic and produces huge amounts of neutrinos [41].

The details of a core-collapse SN are not fully understood, but the basic chain of events is as follows: When a massive star has fused its initial hydrogen reservoir in the center to <sup>56</sup>Fe in a sequence of fusion processes, no further nuclear fusion or fission processes can lead to a release of energy. The different fusion processes were initiated by several contractions of the star and propagate in a shell-like structure to the outer surface. When the mass of

<sup>1</sup>pep: Proton-Electron-Proton fusion

<sup>2</sup> $\approx 1.99 \times 10^{30} \text{ kg}$

<sup>3</sup>SN: Supernova

the iron core exceeds the critical Chandrasekhar limit of 1.4 solar masses, the equilibrium between the star's own gravity and the internal pressure can no longer be maintained and the core collapses. In succession to the high compaction of the matter, "Neutronization" ( $e^- + p \rightarrow n + \nu_e$ ) sets in and  $\nu_e$  become released, which are initially trapped due to the high matter density of  $\rho_{trap} \approx 10^{12} \text{ g cm}^{-3}$ . Infalling matter bounces from the compacted core ( $\rho_0 \approx 10^{14} \text{ g cm}^{-3}$ ) and a hydrodynamic shock wave spreads towards the surface, which rapidly stalls due to further infall of matter. Continuous production of neutrinos and their interaction with the dense matter finally can build up enough pressure to revive the shock and explosively eject the star's outer envelope. Depending on the mass of the progenitor star, the remnant is either a neutron star, which steadily cools down on a time scale of seconds by emission of neutrinos, or a black hole [40].

Core-collapse SNe within the Milky Way are rare. One expects only a few per century, which have a mean distance of 10 kiloparsec =  $30.857 \times 10^{16} \text{ km}$ . In addition to the observation of a single supernova, which would trigger thousands of events in LENA within seconds, one is also interested in detecting the neutrino background from former SNe, the DSNB<sup>1</sup> [42]. The spectrum of DSNB events mainly depends on three factors:

- the number of core-collapse SNe, which can be deduced from the cosmic SN rate as a function of redshift
- the neutrino emission per SN, which determines the energy spectrum
- the detector performance

A detection of a core-collapse SN or the DSNB by LENA would help to resolve important questions of SN research. The huge number of events in LENA from a SN will allow a time-dependent investigation of the burst and thus confirm or reject existing models on core-collapse SNe. Furthermore, oscillation effects at high neutrino densities could be probed. Information on the average neutrino spectrum emitted by SNe, gathered from DSNB data, would contribute to modeling and simulation of SNe and answer the question, if the last supernova SN 1987A [43] was typical.

The great number of free protons in liquid scintillator enables two important detection channels for SN neutrinos in LENA [44]:

- The CC reaction known as the inverse beta decay,  $\bar{\nu}_e + p \rightarrow n + e^+$ , allows for detection of  $\bar{\nu}_e$ . The final state neutron recombines with a proton  $n + p \rightarrow d + \gamma$  (2.2 MeV) after a mean time of 250  $\mu\text{s}$ . A coincidence signal from the prompt positron and the delayed gamma is a clear signature for this type of event.
- NC elastic proton scattering,  $\nu + p \rightarrow \nu + p$ , allows for detection of all neutrino flavors and thus measures the total flux. This detection channel is very sensitive to the mean energy of all neutrino flavors and dominated by  $\nu_\mu$ ,  $\bar{\nu}_\mu$ ,  $\nu_\tau$  and  $\bar{\nu}_\tau$ . The low-energy part of the proton recoil spectrum is highly quenched and thus likely below the threshold of  $\sim 200 \text{ keV}$ . The part above threshold increases with larger mean energies.

<sup>1</sup>DSNB: Diffuse Supernova Neutrino Background

Together with CC / NC reactions of the neutrinos on carbon, LENA can distinguish between different neutrino flavors. It can also probe predictions of SN theory, like the prompt  $\nu_e$ -burst, its absence or conversion to other flavors.

### 3.3.3 Geo- and reactor neutrinos

A natural flux of low-energy neutrinos from Earth itself are geo-neutrinos, which are produced in beta decays,  $n \rightarrow p + e^- + \bar{\nu}_e$ , of naturally occurring radioactive elements. Due to the large temperature gradient between the planet's core and the surface, thermal energy is transported from the interior to the outside. The sources of the thermal energy, as well as the contribution of natural radioactivity from nuclei in the decay chains of  $^{238}\text{U}$  and  $^{232}\text{Th}$  or elements like  $^{40}\text{K}$ , are not fully understood. Measurements yielded different results for the total heat flux, ranging from  $31 \text{ TW} \pm 1 \text{ TW}$  up to  $47 \text{ TW} \pm 2 \text{ TW}$ . The continental crust, which is expected to store about a half of the planet's amount of the formerly mentioned radioisotopes, contributes with  $7.3 \text{ TW} \pm 2.3 \text{ TW}$  ( $2\sigma$ ) [32]. There are different geochemical and geophysical models trying to explain the thermal budget of Earth, as well as the role of natural radioactivity and their various sources. A high-statistics measurement of the geo-neutrino flux with LENA will allow to state stringent limits to the unknown quantities, like the U/Th ratio, to constrain geo-chemical models [32]. Reports on detection of geo-neutrinos have been made by the liquid scintillator detectors KamLAND [45] and Borexino [46], but beyond establishing the existence of this neutrino flux the results did not suffice to distinguish between different forecasts on the quantities of interest.

The measurement of geo-neutrinos and the DSNB (see Section 3.3.2) suffer from heavy background, brought in by  $\bar{\nu}_e$  from nuclear power plants, which represent an artificial low-energy neutrino source on Earth. The neutron-rich fission products of  $^{232}\text{Th}$  and  $^{235}\text{U}$  undergo cascades of  $\beta^-$ -decays, emitting  $\sim 6$   $\bar{\nu}_e$  per fission. Therefore nuclear reactors represent a high-intensity source of  $\bar{\nu}_e$ , which can be distinguished from neutrinos emitted in beta decays of naturally occurring radioactive elements only by their spectrum and cover the spectrum of the DSNB up to  $\sim 10 \text{ MeV}$ . Number and distance of the reactors to the detector are critical parameters and yield different  $\bar{\nu}_e$ -fluxes for different sites. Despite their background character for other fields of neutrino research, a high-statistics measurement of reactor neutrinos with LENA would offer a chance to determine the solar mixing parameters  $\Delta m_{21}^2$  and  $\theta_{12}$  at high precision.

### 3.3.4 Neutrino beams

Within the LAGUNA-LBNO project phase, a neutrino beam application with a LAGUNA type detector is investigated (see Section 3.1.2). Although the LENA detector is best suited for measurements in the low-energy domain below  $100 \text{ MeV}$ , some research topics related to higher energies can also be covered and are expected to yield useful information concerning  $\theta_{13}$ ,  $\delta_{CP}$  and the neutrino mass hierarchy [47]. The performance of a far detector to identify different neutrino-interactions and related particles, as well as the ability to discriminate background, is a crucial ingredient to assess a beam experiment's real gain. Compared to the other technologies, liquid scintillator has been seen as inferior in particle identification and tracking capabilities. Especially at higher energies of several  $\text{GeV}$ , which coincide

with longer baselines. However, the capability to reconstruct extended muon tracks has been demonstrated in Borexino [48] and KamLAND [49], first Monte Carlo studies for the reconstruction of contained lepton tracks returned promising results [7] [6].

Neutrino beams can determine oscillation parameters by  $\nu_e$  appearance in a  $\nu_\mu$  beam. The sensitivity of this search depends to a large extent on the capability to discriminate background events, especially single neutral pion production in NC events. A first approach to discriminate this background in a liquid scintillator detector is topic of this thesis and will be motivated and treated in the following chapters.

### 3.3.5 Nucleon decay

The range of high-energy applications for a LAGUNA type detector not only involves neutrino-based topics, but also extends to the search for physics beyond the SM by challenging stability of matter. Valuable data regarding proton decay has been contributed by the Super-Kamiokande experiment. It currently provides the best lower limits on the life time of the proton, related to different decay branches favored in different GUTs [50]:

$$p \rightarrow e^+ + \pi^0 \quad (\tau > 8.2 \times 10^{33} \text{ a} , 90 \% \text{ CL}) ,$$

$$p \rightarrow \mu^+ + \pi^0 \quad (\tau > 6.6 \times 10^{33} \text{ a} , 90 \% \text{ CL}) .$$

The favored decay mode of most SUSY<sup>1</sup> models is

$$p \rightarrow K^+ + \bar{\nu} \quad (\tau > 2.3 \times 10^{33} \text{ a} , 90 \% \text{ CL}) [51].$$

This is the golden channel for proton decay search in a liquid scintillator detector like LENA. While a water Cerenkov detector can only detect the decay products of the sub-threshold kaon, the ionization signal of the stopping kaon can be detected in liquid scintillator. Together with the delayed signals from the kaon's decay products after a life time of 15 ns and a sophisticated pulse shape analysis background can be suppressed very efficiently, allowing a background-free measurement for 10 years. A new limit of  $4 \times 10^{34}$  a at 90% CL could be set if no event was observed in this time [33].

---

<sup>1</sup>SUSY: Super Symmetry



## Chapter 4

# Neutrino oscillation search with a neutrino beam experiment

The LAGUNA-LBNO project (see Section 3.1.2) studies the application of a LAGUNA-type detector (see Section 3.1.1) as far detector for an oscillation experiment with a neutrino beam. Investigation of the  $\bar{\nu}_e \rightarrow \bar{\nu}_\mu$  appearance channel is expected to contribute valuable information for determination of the mixing parameters  $\theta_{13}$ ,  $\delta_{CP}$  and the neutrino mass hierarchy (see Section 2.4.3), especially at the baseline CERN-Pyhäsalmi considered in LAGUNA. However, the performance of a specific detector type is correlated with its capability to identify background from NC reactions—including single neutral pion production.

This chapter covers the general concept of a neutrino oscillation beam experiment in Section 4.1 and motivates the identification of single neutral pions in Section 4.2. The impact of NC background to the performance of LENA as far detector in a possible long-baseline experiment was assessed within the context of this thesis and is discussed in Section 4.3.

### 4.1 Concept of an oscillation experiment with a neutrino beam

In this section the general concept of a neutrino oscillation beam experiment is discussed. Starting with some general aspects of neutrino beams in Section 4.1.1, the creation in a conventional  $\bar{\nu}_\mu$  beam is explained in Section 4.1.2. The detection of high-energy beam neutrinos for an oscillation analysis is the topic of Section 4.1.3.

#### 4.1.1 General aspects of neutrino beams

As a high intensity neutrino source, a neutrino beam is an established tool for experiments in neutrino physics. Its application allows to measure neutrino interaction cross-sections on atomic nuclei and to investigate neutrino oscillations (see Chapter 2). The latter type of experiment uses the artificial neutrino beam for determining neutrino mixing parameters and to investigate possible effects beyond the standard three-flavor neutrino mixing model. The general concept of a neutrino beam can be implemented in manifold ways. Important parameters for characterizing a neutrino beam include:

- the beam intensity

- the energy spectrum of the beam neutrinos
- the primary flavor of the beam neutrinos
- the information whether it is a neutrino or an anti-neutrino run
- the distance between the source and the detector (baseline)

For sufficiently large distances between source and detector, beam neutrinos can be assumed to be emitted from a point-like source.

Different technological and physical approaches for the creation of neutrino beams exist: The creation of a conventional  $\bar{\nu}_\mu$  beam, as used by experiments like OPERA [31] or T2K [18], relies on accelerated protons and is discussed in the following section. The corresponding analyses focus on the  $\nu_\mu \rightarrow \nu_\tau$  (OPERA) or  $\nu_\mu \rightarrow \nu_e$  (T2K) appearance channels.

A  $\beta$ -beam, on the other hand, is purely comprised of the  $\nu_e$  from the  $\beta^+$ -decay or the  $\bar{\nu}_e$  from the  $\beta^-$ -decay of accelerated radionuclides. In this case, the analysis is done using the  $\bar{\nu}_e \rightarrow \bar{\nu}_\mu$  appearance channel[52]. A neutrino factory uses neutrinos from the decays  $\mu^- \rightarrow e^- + \nu_\mu + \bar{\nu}_e$  and  $\mu^+ \rightarrow e^+ + \bar{\nu}_\mu + \nu_e$  of accelerated muons. Here, the "golden channel"  $\bar{\nu}_e \rightarrow \bar{\nu}_\mu$  is used for the oscillation analysis [53]. It requires the detector to distinguish between  $\nu_\mu$  and  $\bar{\nu}_\mu$  interactions, i. e. a charge-sign determination, as the beam is inherently contaminated with  $\nu_\mu / \bar{\nu}_\mu$  from  $\mu^\pm$ -decay. So far,  $\beta$ -beams and neutrino factories are still theoretical concepts.

#### 4.1.2 Creation of a conventional muon-neutrino beam

The generation of a neutrino beam is a challenging task due to the intrinsic properties of neutrinos. As these particles only interact via the weak interaction and thus have very cross-sections, large neutrino fluxes at the detector site are necessary in order to gather sufficient statistics in a reasonable amount of time. In the case of a long-baseline experiment, this requires a high beam intensity and an optimal focusing of neutrino over distances of several hundreds to thousands of kilometers. As they do not carry electric charge, direct focusing of neutrinos by electromagnetic fields is impossible. Therefore, only the charged, unstable particles, used to produce the neutrinos by their decay, can be focused, confining the direction of the later neutrino beam.

The creation of a conventional  $\bar{\nu}_\mu$  beam based on accelerated protons will be described in the following. This approach is, for instance, implemented by the CNGS beam [54], which sends neutrinos to OPERA [31] and ICARUS [29] experiments, shall serve as an example. A schematic view of the CNGS setup for the beam generation is shown in Figure 4.1.

In the first step, accelerated bunches of protons with several GeV of energy are brought to collision with a stationary target. The target's material must be able to resist high power densities and mechanical stress due to the fast alternating phases of heating and cooling from the impinging proton bunches. Proton beam powers range from several hundreds of kW, as in the case of CNGS<sup>1</sup>, to some MW in case of possible neutrino superbeams [30]. The number of protons directed onto the target POT<sup>2</sup> per time unit is a measure for the neutrino beam's power as it is related to the number of produced neutrinos per time unit.

<sup>1</sup>The mean power of the CNGS neutrino beam is 510 kW[54]

<sup>2</sup>POT: Protons On Target

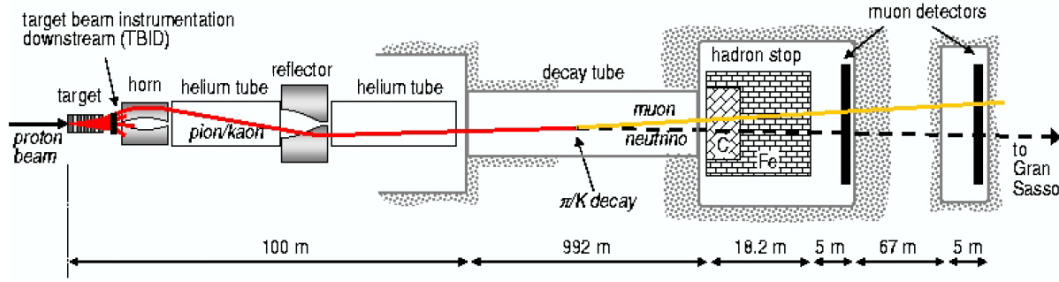


**Figure 4.1:** Schematic view of the CNGS secondary beamline for generation of the neutrino beam. Figure taken from [55].

As the high-energy protons interact with the nuclei of the target, secondary particles such as charged pions and kaons are produced. These short-lived particles become focused towards a decay pipe by a magnetic lens system (called “Horn” and “Reflector”, see Figure 4.1). The adjustable polarity of the lens system (referred to as PHF<sup>1</sup> or NHF<sup>2</sup>) defines the direction of the magnetic field and thus the charge sign of focused / deflected particles. Thus, the later neutrino beam is primarily composed of either  $\nu_\mu$  or  $\bar{\nu}_\mu$ . Inside a long, evacuated decay tube, the pions and kaons decay in flight. The evacuation of the tube reduces defocussing effects from scattering on air molecules. The relevant decay modes of the charged pions and kaons comprise

$$\begin{aligned}\pi^\pm &\rightarrow \mu^\pm + \overset{(-)}{\nu}_\mu, \\ K^\pm &\rightarrow \mu^\pm + \overset{(-)}{\nu}_\mu,\end{aligned}$$

dominantly producing  $\nu_\mu$  or  $\bar{\nu}_\mu$  [14]. Nevertheless, a contamination of about 1% with  $\nu_e$  and  $\bar{\nu}_e$  from other decays is present. Due to the relativistic boost from the reference frame of the decaying particle to the laboratory frame, the neutrinos mainly travel in the original beam direction. The muons accompanying these neutrinos are monitored with muon detectors that are used for supervision of the beam. Protons which did not interact in the target or non-decayed mesons are stopped in a “hadron stop” consisting of high-density material like lead.

### 4.1.3 Detection of high-energy beam neutrinos for oscillation analysis

While the neutrino beam propagates from its source to the detector, the flavor composition of the beam changes due to neutrino oscillations. This effect can be further enhanced by matter effects (see Section 2.3). Investigation of neutrino oscillations is basically done by measurement of the oscillated beam spectrum from neutrino interactions with the detector and comparison to the beam’s original flavor content which is sometimes measured with a near detector.

The sensitivity of a neutrino oscillation experiment is decisively affected by the event rate determination. If only the total event rate is measured, one can solely discover effects causing notable fluctuations in the total flux. If also energy and flavor can be measured, this allows

<sup>1</sup>PHF: Positive Horn Focusing

<sup>2</sup>NHF: Negative Horn Focusing

to gain more insight into effects of neutrino oscillations via distinct oscillation channels. Further-differentiated results can be produced by the determination of the charge sign of the lepton created in CC interactions, as it identifies the event's primary particle as a neutrino or an anti-neutrino. All this requires corresponding detection capabilities. Therefore, the yield of information gained by neutrino oscillation experiments is strongly coupled to the performance of the utilized detector.

The total event rate  $R(r, E_\nu) \propto \phi_\nu(r) \sigma_\nu(E_\nu) m_{\text{target}}$  in a beam experiment's neutrino detector is proportional to the neutrino flux  $\phi_\nu(r) \propto \frac{1}{r^2}$  created by the beam source with distance  $r$  to the detector, the energy-dependent cross-section  $\sigma_\nu(E_\nu)$  for neutrino interactions and the total active target mass of the detector  $m_{\text{target}}$ . The total cross-section  $\sigma_\nu(E_\nu)$  has been subject to different experiments like SciBooNE<sup>1</sup> [56]. These measurements provide valuable input to oscillation experiments, as any uncertainty regarding the neutrino cross-section translates into a systematic error for the determination of event rates and thus for the oscillation analysis. The interactions on a nucleon  $N$  or whole nucleus  $A$  relevant for high-energy neutrino beam applications are [57] [58]:

$$\text{(Quasi-)Elastic scattering: } \nu_l (\bar{\nu}_l) + N \rightarrow l^- (l^+) + N', \quad N \neq N' \quad (\text{CC})$$

$$\nu_l (\bar{\nu}_l) + N \rightarrow \nu_l (\bar{\nu}_l) + N \quad (\text{NC})$$

$$\text{Single pion production: } \nu_l (\bar{\nu}_l) + N \rightarrow l^- (l^+) + N + \pi^+ (\pi^-) \quad (\text{CC})$$

$$\text{(resonant)} \quad \nu_l (\bar{\nu}_l) + N \rightarrow l^- (l^+) + N' + \pi^0, \quad N \neq N' \quad (\text{CC})$$

$$\nu_l (\bar{\nu}_l) + N \rightarrow \nu_l (\bar{\nu}_l) + N + \pi^0 \quad (\text{NC})$$

$$\nu_l (\bar{\nu}_l) + N \rightarrow \nu_l (\bar{\nu}_l) + N' + \pi^\pm, \quad N \neq N' \quad (\text{NC})$$

$$\text{Single pion production: } \nu_l (\bar{\nu}_l) + A \rightarrow l^- (l^+) + A + \pi^+ (\pi^-) \quad (\text{CC})$$

$$\text{(coherent)} \quad \nu_l (\bar{\nu}_l) + A \rightarrow \nu_l (\bar{\nu}_l) + A + \pi^0 \quad (\text{NC})$$

$$\text{Deep-inelastic scattering: } \nu_l (\bar{\nu}_l) + N \rightarrow l^- (l^+) + \text{hadrons} \quad (\text{CC})$$

$$\nu_l (\bar{\nu}_l) + N \rightarrow \nu_l (\bar{\nu}_l) + \text{hadrons} \quad (\text{NC})$$

with  $l = e, \mu, \tau$

Detection of a particle is based on an electromagnetic interaction between the particle and the active detector material (see Section 3.2.1 and [34]). Neutrinos are uncharged particles only participating in the weak interaction and can thus only be detected if they produce charged particles in CC and NC reactions. As stated above, the overall performance of a neutrino oscillation experiment depends on its capability of extracting various information on the incident neutrino. In CC interactions, this information, like the energy and the flavor, is (partially) transferred to the secondary charged particles and the detector is the tool to

<sup>1</sup>SciBooNE: SciBar Booster Neutrino Experiment - SciBar: Scintillator Bar

extract this information. Different techniques exist for this purpose. Those considered in LAGUNA are described in Section 4.2.3.

The final step in an oscillation analysis is to determine the values for the (relevant) mixing parameters which have to be in agreement with the measured differences between oscillated and un-oscillated event rate spectra. This is basically done by statistical hypothesis tests, which take systematic uncertainties, parameter constraints from other experiments and possible parameter degeneracies (see Section 2.4.4) into account. As a final result one gets a region in mixing parameter space, which includes all parameters consistent with the measurement data at a given confidence level (cf. [19]).

## 4.2 Neutral pion background to electron-neutrino appearance search

This section covers the explanation of the neutral pion's background character to  $(\bar{\nu}_e)$  appearance search in a  $(\bar{\nu}_\mu)$  beam. Production of neutral pions in high-energy neutrino interactions is treated in Section 4.2.1, while the neutral pion decay and its consequences to oscillation experiments are discussed in Section 4.2.2. Finally, some remarks regarding approaches for identification of neutral pion events with different detector technologies, including liquid scintillator, are given in Section 4.2.3.

### 4.2.1 Neutral pion production

The neutral pion is a possible product of interactions between high-energy neutrinos and atomic nuclei. It is short-lived and almost instantly decays into particles, which can mimic the signal of an electron event in the detector. Therefore, neutral pion decays (see Section 4.2.2) pose a serious complication to search for appearance of  $(\bar{\nu}_e)$  via characteristic CC interactions.

Dedicated experiments like SciBooNE [56] measured the production of neutral pions in neutrino interactions on nuclear targets, e. g. carbon [59]. The following mechanisms for creation of single neutral pions are important:

**Resonant pion production:** This incoherent process relies on the excitation of a baryonic resonance, e. g.  $\Delta(1232)$ , which subsequently produces a single pion by decay. It contributes the dominant part to overall production of neutral pions, which occurs via the NC reaction

$$\nu_l(\bar{\nu}_l) + N \rightarrow \nu_l(\bar{\nu}_l) + N + \pi^0,$$

$l = e, \mu, \tau$ .  $N$  denotes the participating nucleon. The corresponding CC reaction produces charged pions.

**Coherent pion production:** In the process of coherent pion production the neutrino interacts coherently with the entire nucleus  $A$ . It has a smaller contribution to the overall single neutral pion production than the resonant process. The relevant NC reaction is

$$\nu_l(\bar{\nu}_l) + A \rightarrow \nu_l(\bar{\nu}_l) + A + \pi^0,$$

$l = e, \mu, \tau$ , but also a CC variant producing charged pions exists. As the momentum transfer to the target nucleus is small, the produced pion tends to go in the forward direction in the laboratory reference frame.

#### 4.2.2 Background from neutral pion decay

In quantum mechanics, the neutral pion  $\pi^0$  is a superposition of  $u\bar{u}$  and  $d\bar{d}$  quark combinations:

$$|\pi^0\rangle = \frac{1}{\sqrt{2}} [ |d\bar{d}\rangle - |u\bar{u}\rangle ]$$

It is a short-lived meson with a mass of  $m_\pi = 134.98$  MeV and a mean life time of  $\tau_\pi = (8.4 \pm 0.4) \times 10^{-17}$  s [14]. Even if one assumes speed of light in vacuum  $c_0$  as the pion's speed, its range  $r = c_0 \tau_\pi \gamma \approx \gamma \cdot 25$  nm is only some nanometers. This distance is below spatial resolution of any particle detector. One can assume that a neutral pion always decays at the point of its creation. Relevant decay modes of the neutral pion are [14]:

$$\begin{aligned} \pi^0 &\rightarrow \gamma + \gamma && (\sim 98.8\% \text{ branching ratio}) \\ \pi^0 &\rightarrow \gamma + e^- + e^+ && (\sim 1.2\% \text{ branching ratio}) \end{aligned}$$

Especially the dominant decay mode into two photons poses a real complication to experiments searching for  $\bar{\nu}_e$  appearance in a  $\bar{\nu}_\mu$  beam. These problems are related to the behavior of photons in the detector material and the kinematics of neutral pion decay.

The neutral pion's two-body decay in two photons enforces an opening angle of  $\alpha' = \pi$  between the secondary particles in the rest frame of the pion. In the laboratory reference frame, the opening angle  $\alpha$  ranges from  $\alpha = \pi$  to  $\alpha = 2 \arcsin \frac{m_\pi}{E_\pi} = 2 \arcsin \frac{1}{\gamma}$  for a pion with energy  $E_\pi$  as explained in Appendix A. The last case corresponds to the minimum angle which is possible between the photons (see Equation A.2). It decreases with rising pion energy and therefore makes it more and more difficult to detect the photons separately.

Another problematic scenario is the emission of photons with a maximum angle of  $\alpha = \pi$  in the laboratory frame. Although both photons are spatially separated, the pion's total energy  $E_\pi$  is distributed strongly asymmetric between the photon energies  $E_i$ ,  $i = 1, 2$  (see Equation A.3):

$$\frac{E_i}{E_\pi} = \frac{1}{2} \left( 1 \pm \sqrt{1 - \frac{1}{\gamma^2 \sin^2 \frac{\alpha}{2}}} \right), \quad \sin^2 \frac{\alpha}{2} \in \left[ \frac{1}{\gamma^2}, 1 \right]. \quad (4.1)$$

This circumstance allows that the photon with lower energy misses detection as a separate particle in presence of the photon with much higher energy. Probability for this case even rises with increasing pion energy, as the difference between the photon energies grows larger.

Both discussed scenarios show that one of two photons from neutral pion decay can miss identification as separate particle and therefore only a single particle is observed by the detector. This induces a background to  $\bar{\nu}_e$  search via detection of electrons from  $\nu_e$  CC interactions, as both particles, photons and electrons, have similar event signatures: When a photon or electron passes through the detector, the particle transfers momentum to the (charged) constituents of matter due to various possible scattering processes. If the energy

of the primary particle is high enough, a cascade of charged particles can develop (see for example [60]). Passage of a single charged particle or an entire electromagnetic shower through the target material is detected and subsequently identified as an event. As a result, a neutral pion decay in two photons can be falsely identified as a single electron if the photons are not identified as distinct particles. This distorts measurement of  $\bar{\nu}_e$  event rates and finally the determination of neutrino oscillation mixing parameters.

### 4.2.3 Particle track reconstruction & identification of neutral pion events

In this section, possible methods for reconstruction of particle tracks and identification of neutral pion events with three different detector types are discussed. These three types base on liquid argon, Cerenkov techniques and liquid scintillator. The feasibility of electron and neutral pion discrimination is strongly coupled to the detector's sensitivity to detect charged particles and the possibilities to reconstruct their trajectories.

#### Liquid argon

Detectors using liquid argon as active detector material exploit the physical effect that in highly purified liquid argon an ionization track, created by passage of a charged particle, can drift over distances of several meters. These ionization tracks consist of free electrons. If the drifted ionization signal is read out non-destructively by charge induction on a two dimensional grid of thin wires, one gets a two dimensional projection of the particle event. Further addition of electron drift time information allows to reconstruct a three dimensional image of the event's vertex and related particle tracks [30]. Electron and neutral pion events can be discriminated on the basis of the spatial reconstruction of events, calorimetric measurements of a particle's energy loss  $dE/dx$  and determination of the invariant mass [61]. The latter is calculated for two photons in Appendix A.

#### Cerenkov technique

The Cerenkov effect can be used to detect the passage of a high-energy charged particle through a dielectric medium like water or mineral oil. It bases on the physical fact that the propagation speed of light in matter  $c'$  can be significantly reduced with respect to the speed of light in vacuum  $c_0$ ,  $c' = c_0/n$ .  $n$  is the refractive index of the medium. A charged particle which propagates through a dielectric medium with speed  $v$  and exceeds the local phase velocity of light,  $v/c = \beta > c'$ , distorts the local electromagnetic field. As the insulator restores the locally disrupted equilibrium state, photons are spherically emitted along the particles path. The corresponding light waves would interfere destructively, but as the distortion moves faster than the local speed of light, a Cerenkov light cone is formed by the waves.

The half opening angle  $\theta$  of the cone is related to the particles's speed  $\beta$  according to

$$\cos \theta = \frac{1}{n\beta}. \quad (4.2)$$

If one further adds the correlation between the particle's direction of motion and the Cerenkov cone's alignment in space, tracking of charged particles is possible by detecting the Cerenkov light cone. In order to detect secondary particles from neutrino interactions, the

incident neutrino must deposit a minimum energy to accelerate other particles beyond the Cerenkov threshold  $\beta_{\text{thr}} = 1/n$  [34].

Particle detectors, which rely on the Cerenkov technique, use directionality of the Cerenkov light in order to reconstruct a charged particle's track. Intersection of the light cone with the detector surface creates a characteristic, ring-like pattern, which can be detected by photosensors. Due to the showering character of electrons and high-energy photons, Cerenkov cones from several particles are superimposed and thus form a diffuse ring pattern. In order to discriminate neutral pion and electrons events, a likelihood analysis like in MiniBooNE<sup>1</sup> [62] can be done. Different likelihoods are obtained by fitting the detected light distribution to different particle hypotheses. Each hypothesis is characterized by an assumed number of tracks, event variables, e. g. energies, positions and directions, and related Cerenkov cones. The fit procedure returns the highest likelihood for the particle hypothesis best fitting the event's real light pattern with the corresponding hypothetical light distribution [63].

### Liquid scintillator

Starting conditions for reconstruction of particle tracks in liquid-scintillator are very different compared to the former mentioned techniques for detection of charged particles. The reason is that scintillation light is emitted isotropically when a charged particle passes through scintillating matter (see Section 3.2.1). No directionality is inherent to scintillation light production, contrary to the case of Cerenkov light. Due to this complication for high-energy applications, which require reconstruction of extended particle tracks, liquid scintillator detectors have only been used for low-energy measurements with some tens of MeV.

The only information available for reconstruction of particle tracks in liquid scintillator is the time distribution of photon hits at the photosensors [5]. While a charged particle passes through liquid scintillator, photons are emitted isotropically along its trajectory. A surface containing all photons which possibly do a first photon hit to photosensors can be constructed by superposition of spherical waves with origins along the particle's track (see Figure 4.2). Information on the characteristic shape and directionality of the first photon surface is stored in the spatial arrival pattern and time distribution of first photon hits at the photosensors. This information was used in [7] for reconstruction of lepton tracks in liquid scintillator.

Investigation of feasibility to discriminate electron and neutral pion events in the liquid scintillator detector LENA is subject to this thesis. One possible approach to identify the different event types could be a likelihood analysis based on fits to the particle tracks. This would be comparable to the analysis done in MiniBooNE. However, track reconstruction is difficult for electromagnetic showers from electrons and high-energy photons [7]. Therefore, discrimination of events was done on basis of a multivariate analysis (see Chapter 6) with event variables derived from first photon hits (see Chapter 5).

---

<sup>1</sup>BooNE: Booster Neutrino Experiment

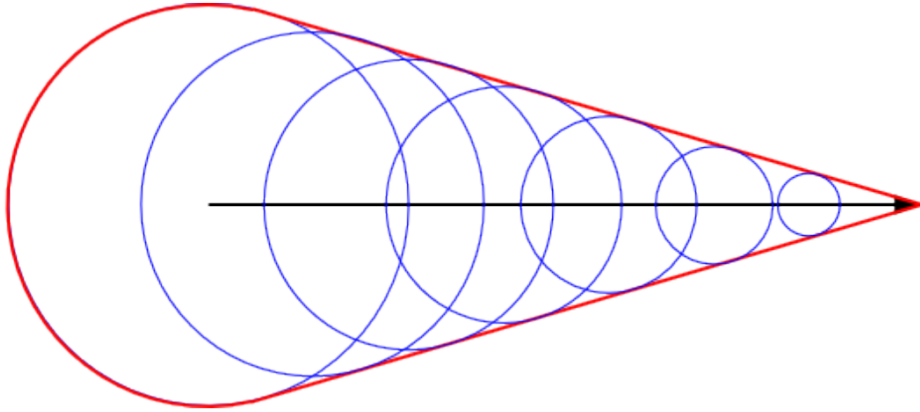


**Figure 4.2:** The first photon surface (red) of a charged particle passing through liquid scintillator (black) can be constructed by a superposition of spherical waves (blue) distributed along the particle's track. Figure taken from [7].

### 4.3 Long-baseline oscillation experiment with LENA

In this section, the performance of LENA in  $\bar{\nu}_e$  neutrino oscillation appearance search with a superbeam experiment is discussed. This analysis primarily aimed to assess the impact of NC background on the sensitivity concerning neutrino mixing parameters (see Section 2.4) and was done with the GLoBES<sup>1</sup> software package [64] [65] within the scope of this thesis.

Section 4.3.1 covers the assumed properties of a specific experimental setup for the baseline CERN–Pyhäsalmi (see Section 3.1.2). Results of the sensitivity analysis regarding the mixing parameters  $\theta_{13}$ ,  $\delta_{CP}$  and the neutrino mass hierarchy will subsequently be presented in Section 4.3.2.

#### 4.3.1 LENA as a far detector

GLoBES is a software package which is primarily designed for the simulation of long-baseline neutrino oscillation experiments on the basis of some parameters describing the experimental setup. These parameters describe properties concerning the neutrino beam, the experiment's baseline and detector characteristics. Other sensitivity studies have already been done specifically for LENA [66] or in the general framework of LAGUNA [20] [47]. Some information for the assumed experimental setup were taken from these references.

#### Baseline

The chosen baseline for the assumed neutrino oscillation experiment was the CERN–Pyhäsalmi baseline with a distance of 2288 km (see Section 3.1.2). Although the matter density distribution along the baseline has already been studied in detail [67], the PREM<sup>2</sup> [68] included in GLoBES was used to save computation time. The uncertainty on matter density was assumed to be 1%.

<sup>1</sup>GLoBES: General Long Baseline Experiment Simulator

<sup>2</sup>PREM: Preliminary Reference Earth Model

### Neutrino superbeam

The creation of a  $(\bar{\nu}_\mu)$  beam was presumed to be done in the conventional way, with high-energy protons (see Section 4.1.2). The specific implementation was a 50 GeV HP-PS2<sup>1</sup> [30] with a run time of 200 days per calendar year and delivering integrated  $3 \times 10^{21}$  POT per year. The corresponding  $\nu$  and  $\bar{\nu}$  fluxes have been computed in [69] [70] and optimized for the baseline to have a peak at the first oscillation maximum around 4.5 GeV (see Figure 4.3). The run time of the neutrino superbeam was set to 5 years with PHF, corresponding to a dominant  $\nu_\mu$  flux, and 5 years with NHF, corresponding to a dominant  $\bar{\nu}_\mu$  contribution to the total flux.

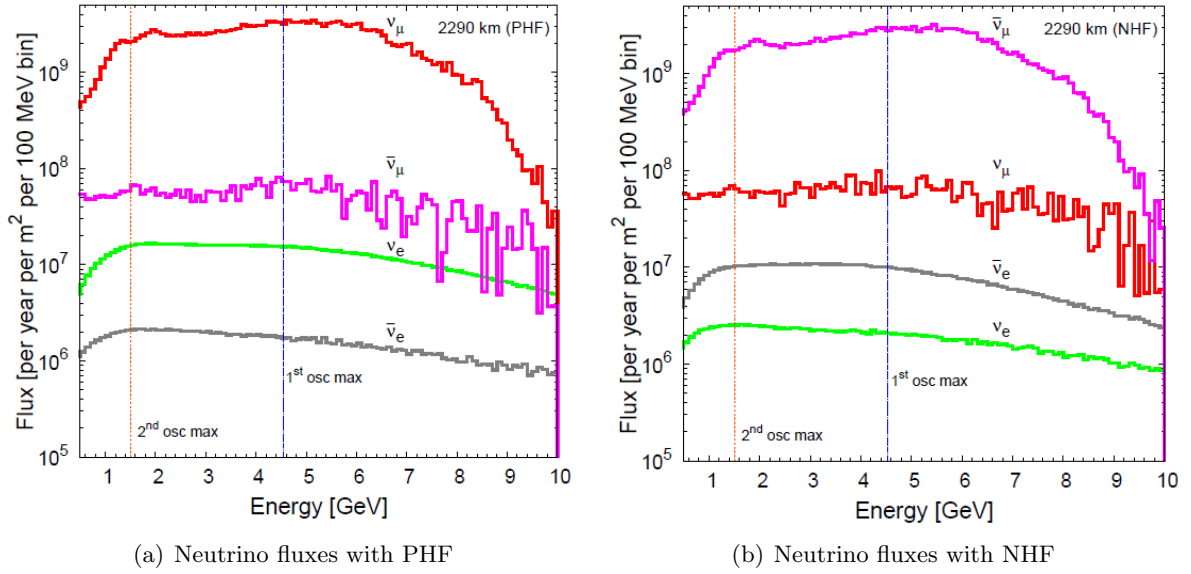


**Figure 4.3:** Un-oscillated superbeam neutrino flux spectra with (a) PHF (b) NHF, at a distance of 2290 km (CERN–Pyhäsalmi) from the beam source. The fluxes were calculated and optimized in [69] to be maximal at the first oscillation maximum around 4.5 GeV (right dashed line). Figure taken from [20].

### Detector characteristics

A fiducial mass of 50 kt was assumed as the target mass of LENA. The detector’s energy resolution was conservatively set to  $\delta E = 5\% \cdot E$ . The primary oscillation channel used for analysis was  $(\bar{\nu}_\mu) \rightarrow (\bar{\nu}_e)$ . Background to this channel was set to come from intrinsic contamination of the neutrino beam with  $\nu_e / \bar{\nu}_e$ , but dominantly from NC events. Furthermore, information from the disappearance channel  $(\bar{\nu}_\mu) \rightarrow (\bar{\nu}_\mu)$  was added.

The baseline of 2288 km requires neutrino energies of several GeV in order to reach the first oscillation maximum at about 4.5 GeV. This energy range is the domain of deep-inelastic scattering processes, which are not fully understood in event reconstruction methods for liquid scintillator: So far, the only available values on lepton identification efficiencies in liquid scintillator for these energies come from [6]. Rejection of the single neutral pion contribution to NC background is the topic of this thesis, but only covers an energy range up

<sup>1</sup>HP-PS: High Power Proton Synchrotron

to 1 GeV. Unfortunately, no data on expected NC rejection efficiencies at the energy range of interest are available.

Due to these circumstances, the CC muon detection efficiency was set to 90%. In order to take the decreasing fiducial volume for longer tracks into account, the muon efficiency was assumed to go linearly to zero from 3 GeV to 7 GeV. The rejection efficiency for NC background was set to 99% and the CC signal efficiency for electron detection was varied during analysis. This is equal to fixing the CC signal efficiency and varying the NC background rejection.

Furthermore, a signal and background normalization error of 5% was assumed for all channels. NC and CC cross-section data for isoscalar targets were taken from [71] [57].

### 4.3.2 Sensitivity to mixing parameters & impact of neutral current background

Different simulations with the GLOBES software were made in order to assess the sensitivity of LENA regarding measurement of  $\theta_{13}$ ,  $\delta_{CP}$  or the neutrino mass hierarchy. A GLOBES simulation bases on numerical calculation of energy-dependent, oscillated event rates for each neutrino flavor and uses the information on neutrino flux, baseline and detector response. The underlying oscillation parameters constitute the set of "true" parameters. A second parameter set includes the "test" values, which are used to formulate hypotheses to be tested on the simulated data. The result of the statistical comparison is a minimized  $\Delta\chi^2$  value, which has to get meaning by connection to corresponding confidence levels. Its calculation includes contributions from systematic effects and the  $1\sigma$  uncertainties of the mixing parameters. Detailed information regarding the calculation of the  $\chi^2$  values can be found in [64] [65].

The oscillation parameters from Section 2.4.1 were used as true values in all simulations and varied within their  $1\sigma$  ranges during minimization of  $\Delta\chi^2$ .  $\theta_{13}$  and  $\delta_{CP}$  were allowed to vary freely despite first measurements setting limits on the value of  $\theta_{13}$  [19]. The impact of parameter degeneracies (see Section 2.4.4) was taken into account in the analysis: In the case of the  $\text{sgn}(\Delta m_{31}^2)$  degeneracy, the results obtained with the set of true parameters were fitted with two different sets of test values for normal and inverted mass hierarchy. The same procedure was used for the  $\theta_{23}$ ,  $\pi/2 - \theta_{23}$  degeneracy. Two sets of test values with the degenerated values for  $\theta_{23}$  were fitted to the true data. The smallest  $\Delta\chi^2$  value of all fits was used as final result.

The following results describe the sensitivity of the long-baseline oscillation experiment with LENA to the investigated parameters as a function of the true values for  $\sin^2 2\theta_{13}$  and  $\delta_{CP}$  for different CC electron detection (signal) efficiencies. Furthermore, the experiment was defined to make a discovery at a specific point in the  $(\sin^2 2\theta_{13}, \delta_{CP})$ -plane if the obtained  $\Delta\chi^2$  exceeds the value corresponding to a  $3\sigma$  CL. In addition, the  $\delta_{CP}$ -coverage, defined as the fraction of  $\delta_{CP}$  values the experiment is sensitive for, is shown as a function of  $\sin^2 2\theta_{13}$ .

#### Sensitivity to $\theta_{13}$

In order to assess the sensitivity of LENA to the mixing angle  $\theta_{13}$ , the true values  $\theta_{13}^{\text{true}}$  and  $\delta_{CP}^{\text{true}}$  were varied and fitted with the hypothesis  $\theta_{13}^{\text{test}} = \delta_{CP}^{\text{test}} = 0$ . The hypothesis was rejected

if  $\Delta\chi^2$  exceeded the value corresponding to a  $3\sigma$  CL.

Results for the sensitivity regions and  $\delta_{CP}$ -coverages are shown in Figure 4.4 and Figure 4.5 for different values of the CC electron detection (signal) efficiency. As one can see from Figure 4.4, the sensitivity strongly depends on the value of  $\delta_{CP}^{\text{true}}$  as indicated by the curved shape of the  $3\sigma$  sensitivity boundary. This is contrary to experiments which measure  $\theta_{13}$  with reactor neutrinos (see Section 3.3.3). These experiments are not sensitive to  $\delta_{CP}$  and therefore have a straight line as sensitivity boundary. The impact of NC background is best seen from the  $\delta_{CP}$ -coverages in Figure 4.5. For CC signal efficiencies between 90 % and 15 % the minimum values of  $\sin^2 2\theta_{13}$  for a sensitivity of the experiment at 50 %  $\delta_{CP}$ -coverage range from 0.002 to 0.01 .

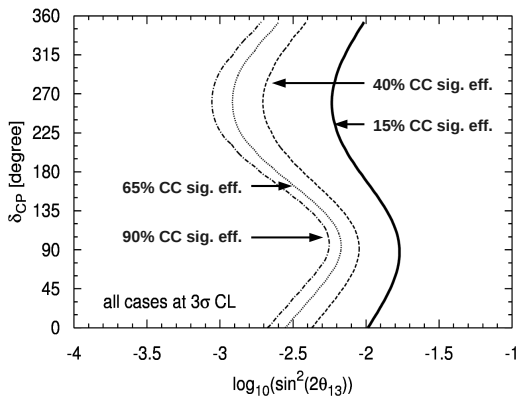


**Figure 4.4:** Sensitivity to  $\theta_{13}$  at  $3\sigma$  CL for different values of CC signal efficiencies (CC sig. eff.).

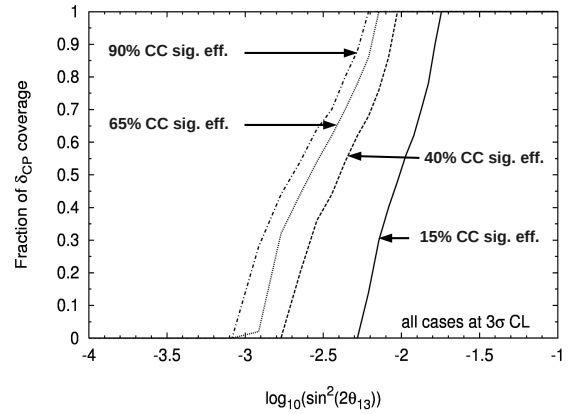


**Figure 4.5:**  $\delta_{CP}$ -coverages for sensitivity on  $\theta_{13}$  at  $3\sigma$  CL.

### Sensitivity to $\delta_{CP}$

The sensitivity of LENA to the CP-violating phase was estimated by fitting the hypotheses  $\delta_{CP}^{\text{test}} = 0, \pi$  to the data simulated with varying true values of  $\theta_{13}^{\text{true}}$  and  $\delta_{CP}^{\text{true}}$ . Figure 4.6 shows the obtained sensitivity regions at  $3\sigma$  CL. As one can see from the results, the sensitivity to CP-violation decreases for values of  $\delta_{CP}^{\text{true}}$  close to  $0^\circ$ ,  $180^\circ$  and  $360^\circ$ . This can be explained with the decreasing contribution of the CP-violating term, which is proportional to  $\sin \delta_{CP}$ , to the oscillation probability  $P_{\mu e}$  (see Equation 2.14). As a consequence, smaller effects from possible CP-violation require more efficient rejection of NC background in order to be sensitive enough. This is best seen from the  $\delta_{CP}$ -coverages in Figure 4.7. CP-violation can be discovered at  $3\sigma$  CL for at least 50 % of possible  $\delta_{CP}$  values and a signal efficiency of 90 % if  $\sin^2 2\theta_{13}$  is greater than 0.016. For a signal efficiency of 40 %,  $\sin^2 2\theta_{13}$  must be greater than 0.079 in order to make a discovery at  $3\sigma$  CL.

### Sensitivity to the neutrino mass hierarchy

Estimation of the experiments sensitivity to the neutrino mass hierarchy was done by fitting the hypothesis of an inverted neutrino mass hierarchy to simulated data for varied

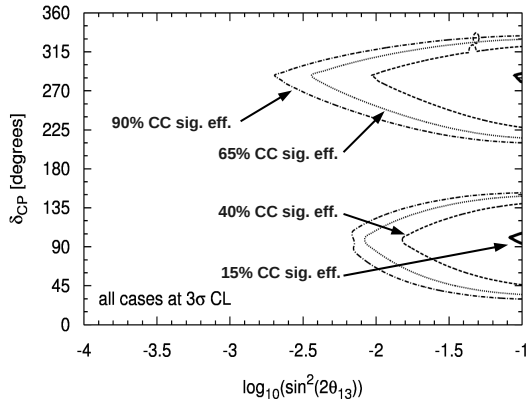


**Figure 4.6:** Sensitivity to CP-violation at  $3\sigma$  CL for different values of CC signal efficiencies (CC sig. eff.).

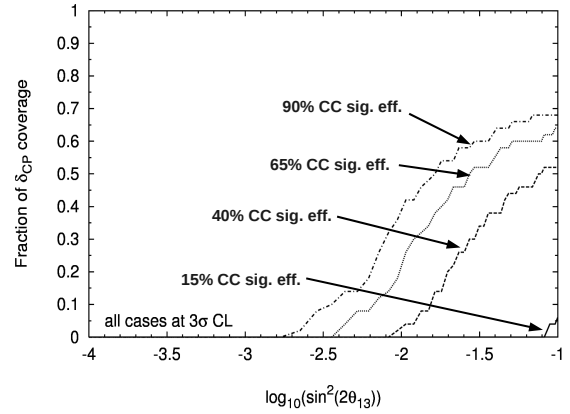


**Figure 4.7:**  $\delta_{CP}$ -coverages for sensitivity on  $\delta_{CP}$  at  $3\sigma$  CL.

true values of  $\theta_{13}^{\text{true}}$  and  $\delta_{CP}^{\text{true}}$ . The simulation of the true data assumed a normal mass hierarchy. Obtained regions for the discovery potential at  $3\sigma$  CL are shown in Figure 4.8. The sensitivity to the neutrino mass hierarchy depends on the value of  $\delta_{CP}^{\text{true}}$ , as indicated by the curved  $3\sigma$  discovery boundary. Figure 4.9 shows the fractions of  $\delta_{CP}$  values covered by the sensitivity regions for different CC signal efficiencies. The minimum values of  $\sin^2 2\theta_{13}$  range from 0.003 to 0.013 for signal efficiencies from 90% to 15% in order to measure the mass hierarchy at  $3\sigma$  CL for at least 50% of possible  $\delta_{CP}$  values.

All three analyses for the sensitivity of a long-baseline experiment with LENA as a far detector show the importance of efficient rejection of NC background events. The following chapters cover an approach to identify neutral pion events from NC single pion production processes, which constitute an important background the  $\bar{\nu}_e$  appearance search in a  $\bar{\nu}_\mu$  beam.

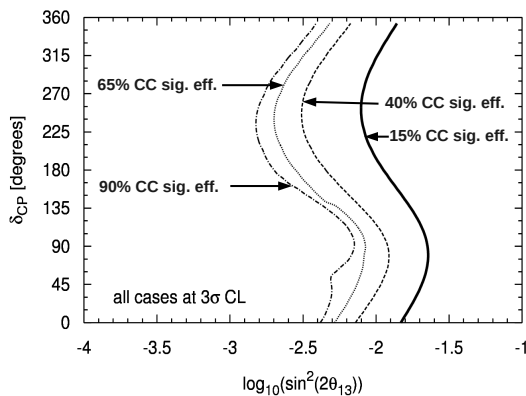


**Figure 4.8:** Sensitivity to neutrino mass hierarchy at  $3\sigma$  CL for different values of CC signal efficiencies (CC sig. eff.).

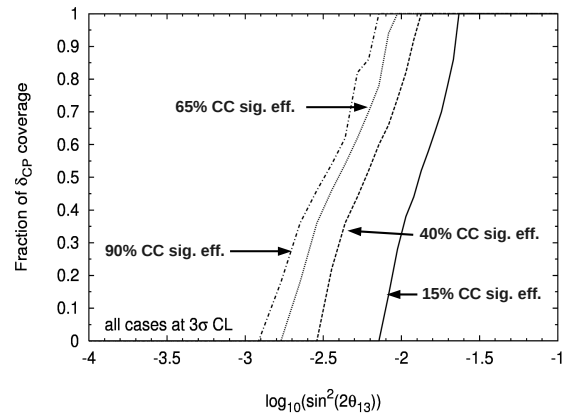


**Figure 4.9:**  $\delta_{CP}$ -coverages for sensitivity on the neutrino mass hierarchy at  $3\sigma$  CL.



# Chapter 5

## Variables for multivariate analysis

Discrimination of single neutral pion events from single electron events in LENA using a MVA<sup>1</sup> technique for classification is subject of this thesis. In the given context a MVA observes and analyzes several statistical, event-based variables in order to use their interrelations for classification as signal (electron) or background (neutral pion) event. While the actually applied MVA method and its results are treated in the subsequent chapter, used variables for event classification are discussed in the following sections. Starting in Section 5.1 with a description of the performed Monte Carlo simulations for this study, the single MVA variables are introduced in Section 5.2 to Section 5.5. The selection of these variables was part of this work, but software implementations to extract them from event data partially profited from existing code already developed in [7].

### 5.1 Monte Carlo simulation

In this section the Monte Carlo simulation used to generate events for the MVA is discussed. The first part covers information on detector setup and physics properties included in the simulation. Details concerning generated events for the MVA are given in the second part.

#### 5.1.1 Simulation setup

The performance of LENA to discriminate single neutral pion events from single electron events with a MVA method was evaluated using simulated events from a LENA detector simulation. It bases on **GEANT4**<sup>2</sup> [72], an object-oriented Monte Carlo simulation framework developed at CERN. The **GEANT4** simulation of LENA involves a simplified geometry of the detector given by a shell structure of different concentric cylinder volumes (cf. Figure 5.1). The innermost volume forms the inner vessel with a radius of 13 m and is filled with PXE-based liquid scintillator<sup>3</sup>. It is surrounded by the buffer volume containing non-scintillating liquid with a radius of 15 m. These inner volumes are enclosed by a 4 cm thick steel tank holding the PMTs. The last outer layer is the muon veto with a radius of 17.04 m and filled

---

<sup>1</sup>MVA: Multivariate analysis

<sup>2</sup>GEANT: Geometry and Tracking

<sup>3</sup>LAB is more likely to be used as liquid scintillator solvent in a future realization of LENA [73]. However, PXE was used for simulation due to its superior timing properties for high-energy applications [32].

with water. All cylinders are 100 m high and their coinciding symmetry axes determine the detector's  $z$ -axis. The origin of the coordinate system is the center of the detector.

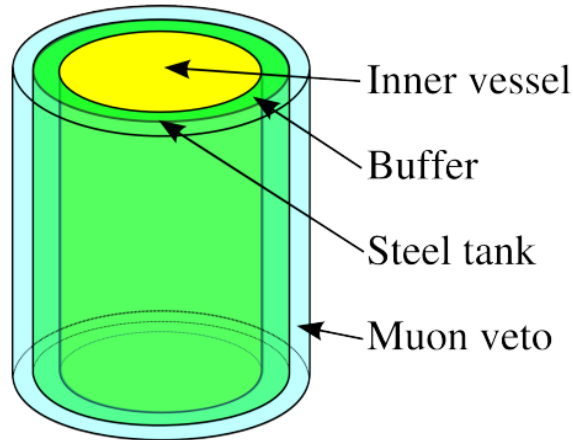


**Figure 5.1:** Schematic view of the simulated detector set up used in the LENA simulation. The inner vessel (yellow) with a radius of 13 m is the central part and contains liquid scintillator based on PXE as solvent. Adjacent to it is a volume of 15 m radius and filled with buffer fluid (green). A 4 cm thick steel tank encloses the inner volumes and separates them from a water filled muon veto (blue) with a radius of 17.04 m. The simulated PMTs at the inner side of the steel tank are not shown. Figure taken from [7].

Core element of the LENA detector is the liquid scintillator with PXE solvent in the inner vessel. Its physical properties (cf. Section 3.2.1) affect the propagation of particles and scintillation light in the active volume. These properties include absorption length, Rayleigh scattering length and absorption-reemission length. A list of relevant quantities incorporated in the LENA simulation is given in Table 5.1.

**Table 5.1:** Properties of the PXE-based liquid scintillator used in the GEANT4 simulation of LENA. The given values are identical to values used in [7].

Scintillator property	Value
Light yield	$2 \times 10^3 \text{ MeV}^{-1}$
Quantum efficiency of PMTs	100 %
Fast fluorescence decay constant	2.9 ns
Slow fluorescence decay constant	29 ns
Weight of fast component	0.8
Refractive index	1.565
Absorption length	20 m
Rayleigh scattering length	51 m
Absorption / Reemission scattering length	40 m
Reemission decay constant	1.2 ns
Birks' constant	$0.15 \text{ mm MeV}^{-1}$

The light transport over macroscopic distances is treated as wavelength independent. Effective

values for a wavelength of 430 nm are used, corresponding to the wavelength shifter's peak emission. In order to reduce computation time by minimizing the number of tracked photons, the effective light yield of the scintillator is reduced from a realistic value of about  $10^4$  photons per MeV to one fifth being  $2 \times 10^3$  photons per MeV. To compensate for this change, the quantum efficiency of the simulated PMTs is increased to 100 % instead of using 20 % as a more realistic value.

Simplified disc-shaped PMTs are simulated for detection of scintillation light. Using only 13 742 PMTs with 20 inch diameter allows further minimization of computation time while reaching the baseline value of 30 % OC for LENA. The photocathode of a single PMT is placed 50 cm off the steel tank's wall, pointing towards the inner vessel. A Gaussian shape with  $\sigma_t = 1$  ns represents the simulated time jitter of a PMT. Important simulation parameters regarding signal readout with PMTs are summarized in Table 5.2.

**Table 5.2:** Properties of scintillation light detection with PMTs for the simulated cylindrical detector.

Readout property	Value
Total number of PMTs	13 742
PMTs at top / bottom cap	871
PMTs at lateral area	12 000
PMT rings at lateral area	120
PMTs per lateral ring	100
PMT diameter	20 inch
Winston cones on PMTs	no
PMT time jitter (Gaussian shape with $\sigma_t$ )	1 ns

Further PMT-effects, e. g. pre-, after- and late pulses, as well as effects from readout electronics, are not simulated.

The output of the simulation is optimized for analysis with the object-oriented ROOT data analysis framework [74] from CERN and comprises the jittered hit time for every detected photon with its corresponding PMT number. The number can be linked to the PMT position in the detector after simulation.

The MVA based only on variables derived from the total collected charge and the times of the first PMT hits. Therefore, it did not make use of the full potential of the ideally simulated FADC-based signal readout.

### 5.1.2 Simulation of signal and background events

The entire analysis based on simulated primary particles which started from the center of the detector. Their momentum direction was along the negative  $x$ -axis. Primary particles are electrons and neutral pions. They were generated directly, meaning that no neutrino interaction vertex creating these particles was simulated or considered.

Two types of event samples were created. The samples used for the MVA consist of:

- 210 000 neutral pions with a flat kinetic energy spectrum between 0 MeV and 865 MeV
- 213 676 electrons with a flat kinetic energy spectrum between 135 MeV and 1 GeV

If one takes the pion's rest energy of approximately 135 MeV into account, both spectra cover the same range of deposited energy. Samples of the second type consist of 20 k monoenergetic particle events each and were used to determine distributions of MVA variables at a given energy with more statistics. The simulated kinetic energies include:

- 400 MeV, 500 MeV and 600 MeV for electrons
- 265 MeV, 365 MeV and 465 MeV for neutral pions

The deposited energies of neutral pions and electrons become equal if one takes again the pion's rest energy into account.

Decay of the instable neutral pion was done by the `GEANT4` simulation. The produced pion samples were not cleaned, that means they comprise approximately 1.2% of sub-dominant  $\pi^0 \rightarrow e^+ + e^- + \gamma$  decays (see Section 4.2.2).

## 5.2 Time-of-flight-corrected first hit time

The TOF-corrected<sup>1</sup> first hit time of an event is the smallest first hit time value of a PMT after a TOF-correction was done to all first photon hits at PMTs. A TOF-correction removes dependencies from the photon hit time data on the event's spatial position by subtracting the photon's propagation time from its detection time. Unfortunately, in liquid scintillator it is impossible to reconstruct the creation time and location for every single photon of a spatially extended high-energy event. This is due to the fact that the initial four-dimensional event information including time evolution becomes projected onto the effectively two-dimensional PMT plane by isotropical scintillation light. As a result of the projection some spatial information gets lost. Furthermore, the amount of extracted information from the time dimension depends on the capabilities of the readout electronics. The simulated FADC-based signal readout marks the best possibility to gather information from the event timing.

### 5.2.1 Barycenter reconstruction

In order to do a TOF-correction to the photon hit times it has to be done with respect to a distinguished point representing the event's position in space. One gets an approximation of the event position if it is assumed that the scintillation light has been isotropically emitted from a point-like source, creating the same spatial charge pattern at the PMTs as the extended event. A first estimate for this point is given by the charge weighted barycenter  $\mathbf{x}_p$  of the  $N_{\text{PMT}}$  PMT positions:

$$\mathbf{x}_p = \sum_{i=1}^{N_{\text{PMT}}} \mathbf{x}_i q_i, \quad (5.1)$$

where  $\mathbf{x}_i$  and  $q_i$  denote the position and collected charge of the  $i^{\text{th}}$  PMT. For this approach, a single PMT's expected charge deviates more from the actually collected charge with increasing distance of the PMT to the barycenter. The reason are effects like scattering and absorption, which affect photons that have to propagate long distances through the detector. Especially for event positions at larger radii this becomes an important factor. Therefore, the barycenter

---

<sup>1</sup>TOF: Time-of-flight

position has to be determined by fit more accurately, respecting relevant optical properties of the scintillator. An algorithm<sup>1</sup> was developed in [7] for this purpose. It was used in this work and bases on minimization of a "negative logarithmic likelihood"  $\mathcal{L} = -\ln[L(\mathbf{x}_p|\mathbf{q})]$ . The likelihood function  $L(\mathbf{x}_p|\mathbf{q}) := P(\mathbf{q}|\mathbf{x}_p)$  is comprised of the total probability  $P(\mathbf{q}|\mathbf{x}_p)$  to find a given PMT charge distribution  $\mathbf{q}$  for a specific barycenter  $\mathbf{x}_p$ . The total probability is the product of the single probabilities for each PMT  $i$  to collect the charge  $q_i$  assuming a Poisson distribution. For the  $i^{\text{th}}$  PMT the expected mean charge is given by

$$\mu_i \propto \frac{1}{|\mathbf{x}_p - \mathbf{x}_i|^2} \cdot \left( \frac{\mathbf{x}_p - \mathbf{x}_i}{|\mathbf{x}_p - \mathbf{x}_i|} \cdot \hat{\mathbf{n}}_i \right) \cdot \exp\left(-\frac{|\mathbf{x}_p - \mathbf{x}_i|}{\lambda_{\text{abs}}}\right). \quad (5.2)$$

$\lambda_{\text{abs}}$  denotes the absorption length,  $\mathbf{x}_i$  is the position of the  $i^{\text{th}}$  PMT and  $\hat{\mathbf{n}}_i$  its normal vector pointing outwards.

### 5.2.2 Time-of-flight correction

The TOF-correction of the photon hits is done with respect to the fitted barycenter  $\mathbf{x}_p$ :

$$t_i^{\text{TOF}} := t_i - \frac{|\mathbf{x}_p - \mathbf{x}_i|}{c/n}, \quad (5.3)$$

with speed of light in vacuum  $c$  and refractive index  $n$ . After the TOF-correction has been applied to all photon hit times, the smallest time value determines the TOF-corrected first hit of the event. The corresponding PMT is likely to be found in the opposite direction of the particle track<sup>2</sup> and has a negative TOF-corrected first hit time. This is illustrated in Figure 5.2.

The track of a particle starts at  $\mathbf{x}_s$  and ends at  $\mathbf{x}_e$ . A PMT located at  $\mathbf{x}_1$  gets its first hit by photons originating  $\mathbf{x}_s$ . The hit time  $t^{\mathbf{x}_1}$  with respect to the start time of the event<sup>3</sup>  $t_0 = 0$  is given by

$$t^{\mathbf{x}_1} = \frac{n}{c} |\mathbf{x}_s - \mathbf{x}_1| - t_0 = \frac{n}{c} |\mathbf{x}_s - \mathbf{x}_1|. \quad (5.4)$$

A TOF-correction with respect to the barycenter  $\mathbf{x}_p$  yields

$$t_{\text{TOF}}^{\mathbf{x}_1} = \frac{n}{c} (|\mathbf{x}_s - \mathbf{x}_1| - |\mathbf{x}_p - \mathbf{x}_1|). \quad (5.5)$$

From Figure 5.2 it is obvious that  $|\mathbf{x}_s - \mathbf{x}_1| < |\mathbf{x}_p - \mathbf{x}_1|$  and thus  $t_{\text{TOF}}^{\mathbf{x}_1} < 0$ . Furthermore,  $t_{\text{TOF}}^{\mathbf{x}_1}$  is minimal if  $\mathbf{x}_1$  is located on a straight line with  $\mathbf{x}_p$  and  $\mathbf{x}_s$  in the opposite direction of the particle track. One also finds that  $t_{\text{TOF}}^{\mathbf{x}_2} > t_{\text{TOF}}^{\mathbf{x}_1}$  always holds as explained in [7]. The reason is that one has to take the particle's TOF between  $\mathbf{x}_s$  and  $\mathbf{x}_e$  into account.

<sup>1</sup>The algorithm bases on a fit using the MIGRAD minimization algorithm from MINUIT package [75] integrated into the ROOT analysis framework [74]. Only light absorption in the scintillator is considered to keep the fitting procedure fast.

<sup>2</sup>High-energy electrons and photons create electromagnetic showers in liquid scintillator. As the energy-loss occurs spatially extended, it is impossible to define and reconstruct a distinct particle track. Nevertheless, the term "track" is used for illustration.

<sup>3</sup>Determination of an event's start time in liquid scintillator is a non-trivial issue. It is related to reconstruction of the event's primary vertex. Details can be found in [7]. For the simulated events used in this work the start is always  $t_0 = 0$ .

Equation 5.5 also allows for an ostensive interpretation of the TOF-corrected first hit time, at least in case of particle tracks in the  $x$ - $y$ -plain:

If the PMT with the event's TOF-corrected first hit  $\mathbf{x}_{\text{fh}}$  is in line with the track, but in the opposite direction, the modulus of the TOF-corrected first hit time  $|t_{\text{TOF}}^{\mathbf{x}_{\text{fh}}}|$  is a measure for the "track length"  $|\mathbf{x}_p - \mathbf{x}_s|$  according to

$$|t_{\text{TOF}}^{\mathbf{x}_{\text{fh}}}| \propto |\mathbf{x}_p - \mathbf{x}_{\text{fh}}| - |\mathbf{x}_s - \mathbf{x}_{\text{fh}}| \approx |\mathbf{x}_p - \mathbf{x}_s| . \quad (5.6)$$

The situation is different for tracks with large incident angles towards the  $z$ -axis of LENA. With increasing incident angle of the track the probability rises that expected and actual point of first photon hit differ. This is due to the fact that the expected first hit photons are more likely to become absorbed on their long way through scintillator (see Figure 5.3).

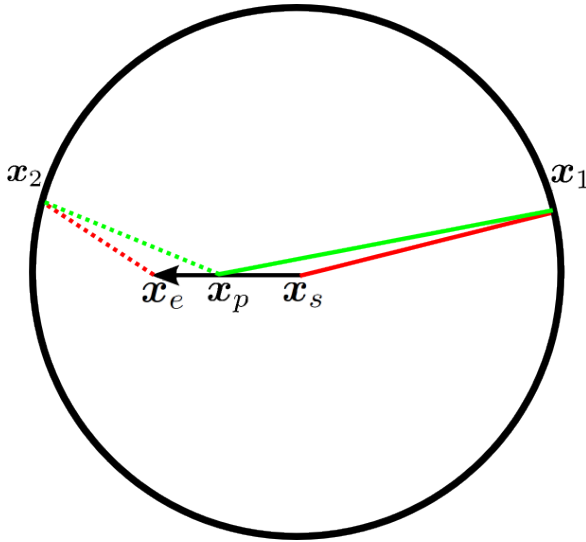


**Figure 5.2:** Schematic view to emphasize the influence of a PMT position and the track direction on the PMT's TOF-corrected hit time. The first hit photon for a PMT at  $\mathbf{x}_1$  originates  $\mathbf{x}_s$  and its TOF is given by the time to travel from  $\mathbf{x}_s$  to  $\mathbf{x}_1$  (solid red line). The TOF-correction is done with respect to the TOF between  $\mathbf{x}_p$  and  $\mathbf{x}_1$  (solid green line). For the TOF-corrected hit time of a PMT at  $\mathbf{x}_2$  (dashed lines) one has to take the TOF between  $\mathbf{x}_s$  and  $\mathbf{x}_e$  into account. As a consequence, the TOF-corrected hit time of  $\mathbf{x}_1$  is smaller than the TOF-corrected hit time of  $\mathbf{x}_2$ . Figure taken from [7].

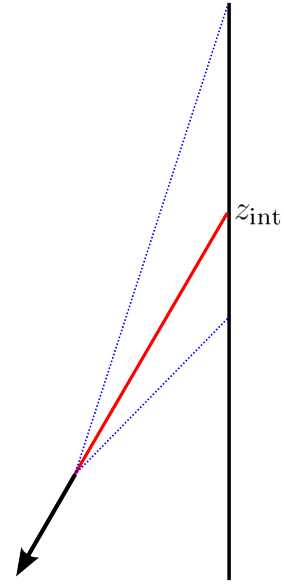


**Figure 5.3:** Impact of a track's incident angle towards the  $z$ -axis on the  $z$ -position of an event's first photon hit. Photons above the expected TOF-corrected first hit point at  $z_{\text{int}}$  (upper blue dashed line) have to travel longer ways through scintillator than photons below  $z_{\text{int}}$  (lower blue dashed line). Therefore, the upper photons are more likely to be absorbed than the lower ones. Figure taken from [7].

### 5.2.3 Time-of-flight-corrected first hit time as event variable

A distribution of TOF-corrected times for the events' first PMT hits is shown in Figure 5.4 for electron and neutral pion events with a true deposited energy of 500 MeV . For a given true energy, the distribution's maximum for electrons is shifted to lower values with respect

to the distribution maximum for pions. Although both distributions partially overlap, the TOF-corrected first hit time yields valuable contributions to particle classification due to the unique features of the distributions like the separated maxima. Although it is not intended to discuss the distributions of all MVA variables in detail, some general information on influencing effects are given in the case of the event's TOF-corrected first hit time.

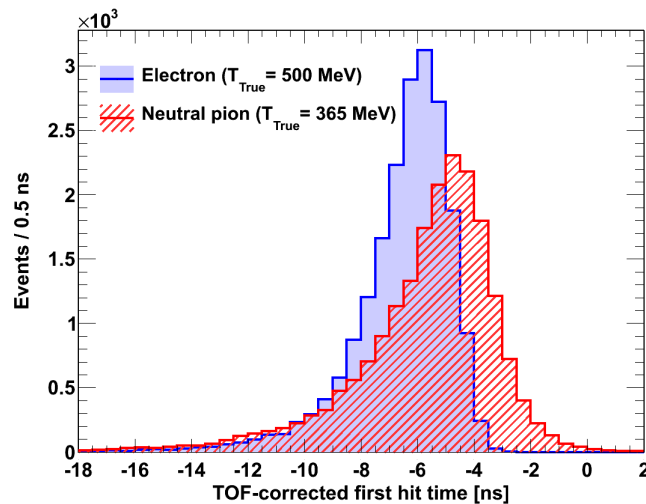


**Figure 5.4:** Distributions of an event's TOF-corrected first PMT hit time for 20k electrons and 20k neutral pions with 500 MeV true deposited energy.

High-energy electrons and the photons from neutral pion decay can create cascades of secondary particles when interacting with the liquid scintillator<sup>1</sup>. This is due to multiple interaction processes like bremsstrahlung, Compton scattering or pair-production. These electromagnetic showers have no defined track and suffer stronger event by event fluctuations compared to a muon [7]. Nevertheless, a corrected barycenter can be determined from the produced scintillation light of charged particles in the showers.

In the electron case, the direction of the shower is roughly determined by the electron's (initial) direction of motion. The electron is likely to change its momentum direction in interactions with matter due to its low mass. Only kinematic focusing approximately keeps the electron's initial direction of motion. The same holds for high-energy secondary electrons from interactions in the shower. In the given analysis scenario, electrons have their initial momentum direction in negative  $x$ -direction. Therefore, the track length  $|\mathbf{x}_p - \mathbf{x}_s|$  and thus  $|t_{\text{TOF}}^{\text{th}}|$  (see Equation 5.6) is basically determined by the electron's starting energy, but influenced by strong event-based fluctuations (see [7]).

In the neutral pion case, the number of degrees of freedom affecting electromagnetic shower creation is larger than in the electron case. The main reason is of course the number of

<sup>1</sup>Creation of particle cascades occurs as long as the energy of the primary and secondary particles is above a material-dependent critical energy. The initial energy of the primary particle therefore determines the number of "particle generations" included in a cascade (cf. [60]). If the primary energy is too low to create several generations, no fully extended cascade can be created. This is especially true for energies below 1 GeV and leads to strong event by event fluctuations of the cascades.

involved particles. Two photons<sup>1</sup> from neutral pion decay against a single electron. Two-body decay kinematics constraints the photons' energies and directions of momenta<sup>2</sup>. In the laboratory frame the angle between the photons can be between  $\pi$  and an energy-dependent minimal angle (see Section 4.2.2). Therefore, the position of the event's barycenter  $\mathbf{x}_p$  is determined by two different electromagnetic showers with different energy contents. In addition, a photon from pion decay does not produce scintillation light right from the start of its propagation. It becomes only indirectly visible if it transfers momentum to a charged particle which subsequently produces detectable scintillation light. Hence, a photon can cover some distance invisible to the detector. This introduces distinct starting points for electromagnetic showers from two photons originating neutral pion decay<sup>3</sup>. All mentioned effects influence the track length  $|\mathbf{x}_p - \mathbf{x}_s|$  as they affect the barycenter position  $\mathbf{x}_p$  and / or the starting position  $\mathbf{x}_s$  for shower creation.

As a result, more fluctuations in neutral pion events are possible than in electron events due to a higher number of degrees of freedom in the former case. This translates into a wider distribution of the event's TOF-corrected first PMT hit for neutral pions.

The distributions of times from first PMT hit are expected to change significantly if the simplified analysis conditions with primary particles bound to  $x$ - $y$ -plane and no real neutrino interaction vertex are abandoned. As discussed in Section 5.2.2, larger incident angles of particle tracks towards the  $z$ -axis increase probability that expected and actual point of first photon hit differ. As a consequence of this,  $|t_{\text{TOF}}^{\text{fh}}|$  can no longer be interpreted as measure for the track length according to Equation 5.6. Furthermore, the consideration of a primary neutrino interaction with nuclei possibly introduces an additional energy deposition at the vertex due to knocked out nucleons. Scintillation photons from this energy deposition could include the event's first hit photon and thus yield new contributions to the distribution of the event's TOF-corrected first PMT hit.

### 5.3 Reconstructed energy

Energy reconstruction<sup>4</sup> in liquid scintillator bases on counting of scintillation photons in photosensors. The total number of detected photons  $N_{\gamma}^{\text{det}}$  is proportional to the total number of produced photons which again is proportional to the deposited energy (Section 3.2.1). In order to reconstruct the deposited energy, all constants of proportionality and effects influencing the number of detected scintillation photons must be known. Some of these factors, like the overall efficiency for light detection (Section 3.2.2), are static parameters. Effects like quenching and absorption (Section 3.2.1) introduce dependencies on event properties like particle type and spatial position in the detector. Especially in case of large detectors like LENA, absorption has a notable impact on the number of detected scintillation photons. The absorption probability of photons increases with larger distances the scintillation light

<sup>1</sup>The neutral pion decay mode  $\pi^0 \rightarrow \gamma + e^+ + e^-$  contributes only with 1.2% and is therefore neglected.

<sup>2</sup>Contrary to the direction of the neutral pion, the starting directions of the photons are not bound to the  $x$ - $y$ -plane. These directions were set randomly by GEANT4 according to neutral pion decay kinematics

<sup>3</sup>These starting points of electromagnetic showers induced by high-energy photons can also differ from a considered neutrino interaction vertex.

<sup>4</sup>Reconstruction of an event's energy means to derive the actually deposited energy from the gathered data (number of detected photons) systematically.

has to cover. In order to take this effect into account, the spatial structure of an event has to be considered in energy reconstruction. This leads to a time-consuming global fit, which aims for determination of the involved particles with their kinetic properties at their vertex (cf. [7]).

Due to the complexity of a global fit, a less accurate but much faster determined result was chosen as energy variable for the MVA. The procedure was developed as an energy estimate for the global fit in [7]. One assumes a point-like energy deposition at the barycenter of the event. Together with a fitted radial<sup>1</sup> dependence of the detected photon number one can calculate an estimate for the deposited energy:

$$E_{\text{reco}} = a \cdot \left( \frac{N_{\gamma}^{\text{det}}(\rho_0 = 0)}{N_{\gamma}^{\text{det}}} \right) (\rho_0) \cdot N_{\gamma}^{\text{det}}, \quad (5.7)$$

where  $\rho_0$  denotes the radial event position.  $\left( \frac{N_{\gamma}^{\text{det}}(\rho_0 = 0)}{N_{\gamma}^{\text{det}}} \right) (\rho_0)$  is determined by the fitted radial dependence of the detected photon number.  $a = 6 \times 10^{-3} \text{ MeV}$  is a constant of proportionality.

A distribution of reconstructed energies for 20k electrons with a true<sup>2</sup> kinetic energy of 500 MeV is shown in Figure 5.5.

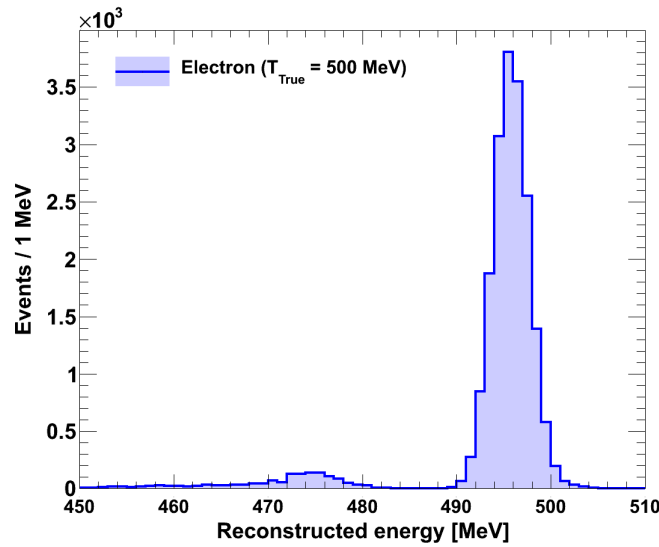


**Figure 5.5:** Distribution of reconstructed energies for 20k electrons with true deposited energy of 500 MeV. A Gaussian fit to the main peak yielded  $(495.81 \pm 1.9) \text{ MeV}$ .

The distribution includes two distinct peaks. A high, narrow peak has its maximum close to the true value of 500 MeV, but is slightly shifted to lower energies. This systematic shift is due to the assumption of a point-like energy deposition. Furthermore, modifications to the

<sup>1</sup>The number of detected photons also depends on the  $z$ -coordinate of the event. Nevertheless, this effect is neglected due to the detector height compared to the limited area around the center where events were simulated.

<sup>2</sup>The true value refers to the value truly set by Monte Carlo simulation.

**Table 5.3:** Summary of quantities derived from the reconstructed energy distributions of 20 k electrons for different true deposited energies. Mean reconstructed energy  $E_{\text{reco}}$  and standard deviation  $\sigma_E$  were determined by a Gaussian fit to the main peak of the distribution.

Quantity	True deposited energy $E_{\text{true}}$ for electrons		
	400 MeV	500 MeV	600 MeV
Mean reconstructed energy $E_{\text{reco}}$	396.69 MeV	495.81 MeV	594.90 MeV
Standard deviation $\sigma_E$	1.70 MeV	1.90 MeV	2.11 MeV
Energy resolution $\sigma_E/E_{\text{reco}}$	0.43 %	0.38 %	0.35 %
Fraction of events below ( $E_{\text{true}} - 15$ MeV)	6.67 %	8.25 %	9.86 %

**Table 5.4:** Summary of quantities derived from the reconstructed energy distributions of 20 k neutral pions for different true deposited energies. Mean reconstructed energy  $E_{\text{reco}}$  and standard deviation  $\sigma_E$  were determined by a Gaussian fit to the main peak of the distribution.

Quantity	True deposited energy $E_{\text{true}}$ for neutral pions		
	400 MeV	500 MeV	600 MeV
Mean reconstructed energy $E_{\text{reco}}$	396.50 MeV	495.57 MeV	594.68 MeV
Standard deviation $\sigma_E$	1.76 MeV	1.97 MeV	2.19 MeV
Energy resolution $\sigma_E/E_{\text{reco}}$	0.44 %	0.40 %	0.37 %
Fraction of events below ( $E_{\text{true}} - 15$ MeV)	6.81 %	8.60 %	10.48 %

barycenter determination procedure (see Section 5.2.1) have not been translated to a revision of the energy estimation and possibly contribute to the systematic shift as well [76].

The second peak is lower and wider. It is located  $\sim 20$  MeV below the main peak and has a tail towards lower energies. This smaller peak probably corresponds to the giant resonance [77] of carbon from liquid scintillator in combination with emitted, highly quenched nucleons<sup>1</sup> [76]. A giant resonance can be macroscopical interpreted as a nuclear excitation with a collective oscillation of all protons against all neutrons. Its decay modes include nucleon emission and thus missing energy can be explained by losses due to nuclear binding energy and quenching. However, giant resonance as the real cause for the smaller peak in the distribution of reconstructed energies was not checked.

The width of the main peak  $\sigma_E$  and its mean position  $E_{\text{reco}}$  were determined from a Gaussian fit in the range of  $E_{\text{true}} \pm 15$  MeV from the true energy value  $E_{\text{true}}$ . Furthermore, the fraction of events below  $E_{\text{true}} - 15$  MeV was investigated. Results from all high-statistics event samples (see Section 5.1.2) are summarized in Table 5.3 for electrons and in Table 5.4 for neutral pions.

<sup>1</sup>Kinetic energy of a neutron is indirectly quenched if it transfers momentum to a proton by collision. The proton's kinetic energy subsequently underlies quenching.

## 5.4 First hit pulse shape variables

A set of variables for the MVA to discriminate neutral pion and electron events was extracted from the TOF-corrected first hit pulse shape of an event. If one considers the two different cases of two high-energy photons from pion decay or a single electron propagating through the detector, one naively expects a difference in the time distribution of first photon hits at the PMTs. This expectation emerges from the assumption of different detector responses for both event types due to differences in the initial particle count and therefore in the spatial extent of induced electromagnetic showers. Because of the energy-dependent minimal angle between the photons from neutral pion decay (see Section 4.2.2), the induced electromagnetic showers are probably more spread around the combined barycenter compared to a shower from a single electron. Therefore, the showers from pions deviate more from the assumption of a point-like energy deposition. As a consequence, the time structure of first PMT hits is presumably different for electrons and two high-energy photons.

### 5.4.1 First hit pulse shape & Adaptive kernel estimation

The time distribution of first photon hits at the PMTs is the first hit pulse shape of an event. If a TOF-correction is applied to the hit times with respect to the event's barycenter according to Equation (5.3), one gets the TOF-corrected first hit pulse shape. This shape is less dependent on the event position in the detector. A comparison of averaged TOF-corrected first hit pulse shapes for electrons and neutral pions is shown in Figure 5.6(a).

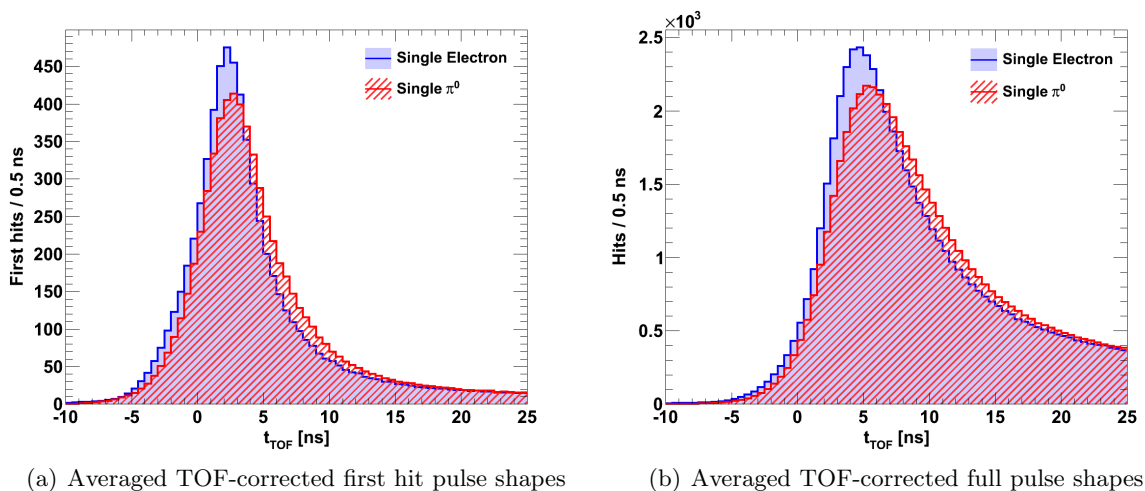


**Figure 5.6:** TOF-corrected pulse shapes for electrons and neutral pions including (a) only first photon hits (b) all photon hits. It was averaged over 100 events of each particle type with a true energy of 500 MeV.

Differences between both averaged TOF-corrected first-hit pulse shapes exist and motivate extraction of event variables for the later MVA. As one can also see in Figure 5.6(a), the disparity between both averaged pulse shapes is small. Therefore, it is hard to determine the variables from a histogram while capturing the unique features of an event's pulse shape.

A comparable wide histogram binning smears out the features of a pulse shape and thus the basis for event classification. Narrow binning introduces strong fluctuations of the bin content and artificial features to the pulse shape, making it difficult to reasonably determine the desired quantities. A parameterized fit to the pulse shape is difficult due to lack of an adequate model, which reliably captures distinct event by event variations. This is why a non-parametrized fitting technique was used to approximate the pulse shape.

AKE<sup>1</sup> [78] provides a non-parametric estimate for a probability density function from the set of underlying data. In FKE<sup>2</sup> the parent distribution is approximated by

$$\hat{f}_0(x) = \frac{1}{nh} \sum_{i=1}^n K\left(\frac{x-t_i}{h}\right), \quad (5.8)$$

with  $\{t_i\}$  as the underlying data set and  $h$  as smoothing parameter.  $K$  is the kernel function. It spreads out the contribution of each data point to the parent distribution's estimate. AKE replaces the global smoothing parameter  $h$  by a local parameter  $h_i = h/\sqrt{f(t_i)}$ . As a result, the parent distribution is estimated by narrow kernels in regions with high (data point) density and by wide kernels in regions with low (data point) density:

$$\hat{f}_1(x) = \frac{1}{n} \sum_{i=1}^n \frac{1}{h_i} K\left(\frac{x-t_i}{h}\right). \quad (5.9)$$

As implementation of AKE the TKDE-class from the ROOT analysis framework was used. The kernel function  $K$  was chosen to be a Gaussian function and a parameter affecting the kernel function's width was set to 0.6. Only up to a pulse shape value of 30 ns was fitted in order to save some computation time per event.

The resulting fit function sufficiently smooths the pulse shape while keeping its unique features (cf. Figure 5.7). A drawback of this algorithm is the overall increase in computation time as some thousands of Gaussian functions have to be summed up and evaluated.

The following sections introduce the quantities which were determined from the AKE-fit or underlying data as MVA variables.

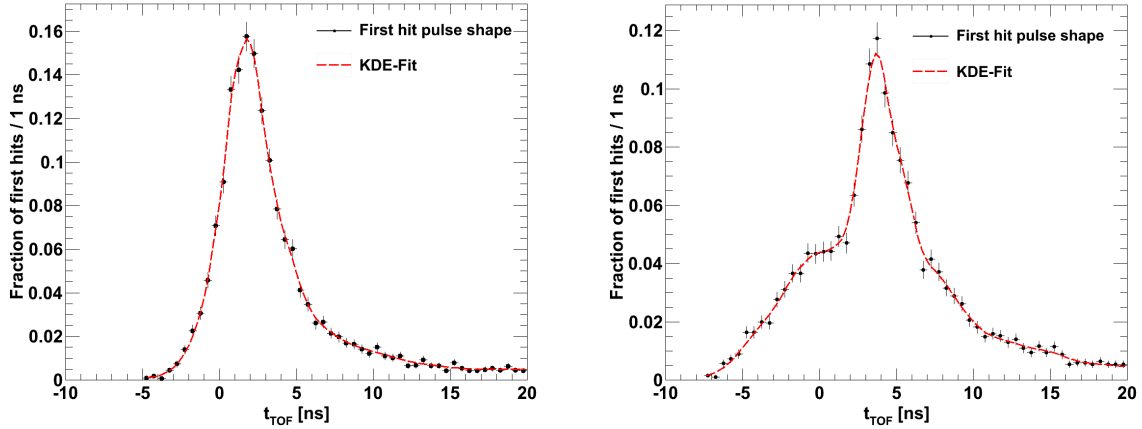
### 5.4.2 Maximum pulse height

The TOF-corrected first hit pulse shape was normalized with respect to the integral over the pulse shape, corresponding to the total number of active PMTs. Motivated by the slight difference between maximum values of averaged pulse shapes (see Figure 5.6(a)), the maximum pulse height was determined from the AKE-fit and used as MVA variable. A distribution of the maximum pulse heights for is shown in Figure 5.8(a).

---

<sup>1</sup>AKE: Adaptive Kernel Estimation

<sup>2</sup>FKE: Fixed Kernel Estimation



(a) TOF-corrected first hit pulse shape close to the average shape of 5.6(a)

(b) TOF-corrected first hit pulse shape with deviation from the average shape of 5.6(a)

**Figure 5.7:** TOF-corrected first hit pulse shapes for electrons, normalized with respect to the event's total number of active PMTs. The KDE-fit successfully works for (a) pulse shapes close to the averaged shape of 5.6(a) and (b) pulse shapes with strong deviations from the averaged shape.

### 5.4.3 Pulse fall

The fall of the hit pulse is defined as time span  $\Delta t = t_1 - t_0$ ,  $t_0 < t_1$ , the first hit pulse needs to fall from an upper level  $l_{\text{up}}(t_0)$  to a lower pulse level  $l_{\text{low}}(t_1)$  after the pulse reached its maximum value. The evaluation levels for pulse fall were set to  $l_{\text{low}} = 20\%$  and  $l_{\text{up}} = 90\%$ . A distribution of pulse falls is shown in Figure 5.8(b).

### 5.4.4 Pulse rise

The pulse rise is defined as time span  $\Delta t = t_1 - t_0$ ,  $t_0 < t_1$ , the first hit pulse needs to rise from a lower level  $l_{\text{low}}(t_0)$  to an upper pulse level  $l_{\text{up}}(t_1)$  before the pulse reaches its maximum value. The evaluation levels were set to  $l_{\text{low}} = 20\%$  and  $l_{\text{up}} = 90\%$ . A distribution of pulse rises for electrons and neutral pions with a true deposited energy of 500 MeV is shown in Figure 5.8(c).

### 5.4.5 Pulse width

The evaluation of the first hit pulse width was done at a certain pulse level with respect to the pulse maximum as distinguished point. The evaluation level was optimized for 20 k electrons and neutral pions at energies of 400 MeV and 600 MeV in order to achieve maximum separation of pulse width distributions. As quantity for optimization the separation  $\langle S^2 \rangle$  [79] defined by

$$\langle S^2 \rangle = \frac{1}{2} \int \frac{(\hat{y}_S - \hat{y}_B)^2}{\hat{y}_S + \hat{y}_B} dy, \quad (5.10)$$

with  $\hat{y}_S$  and  $\hat{y}_B$  as signal and background distributions of variable (pulse width)  $y$ , was used.  $\langle S^2 \rangle$  is zero for identical shapes and one for no overlap. The pulse widths of electron and neutral pion pulse shapes were evaluated at levels between 20 % and 90 % in steps of 5 % with

respect to the maximum pulse height. Both true energy values yielded best separation for evaluation of the pulse width at 80% level. A distribution of the pulse width is shown in Figure 5.8(d) for electrons and pions with a true deposited energy of 500 MeV.

#### 5.4.6 Pulse mean time

An analysis of low-energy muons in Borexino [3] extracts information from the mean time of a pulse [73]. Inspired by this, the mean time of the TOF-corrected first hit pulse was determined from the underlying first hit times directly and used as variable. Further motivation for this quantity to be used as MVA variable is a slight offset of the maxima of the averaged first hit pulse shapes (see Figure 5.6(a)). As one can see in Figure 5.8(e), this offset translates to separation of the mean time distributions for electrons and neutral pions and therefore yields information for event type classification. Furthermore, the distributions' maxima are in the range of some nanoseconds, but some outliers exist with mean times of several microseconds. A possible explanation could be a delayed decay of an excited nuclear state. However, this phenomenon was not further investigated.

As all of the mentioned quantities rely on the basic information of first hit times, one has to anticipate strong correlations between the different variables. Correlations between variables in the data sets used for the MVA are discussed in Section 6.2.

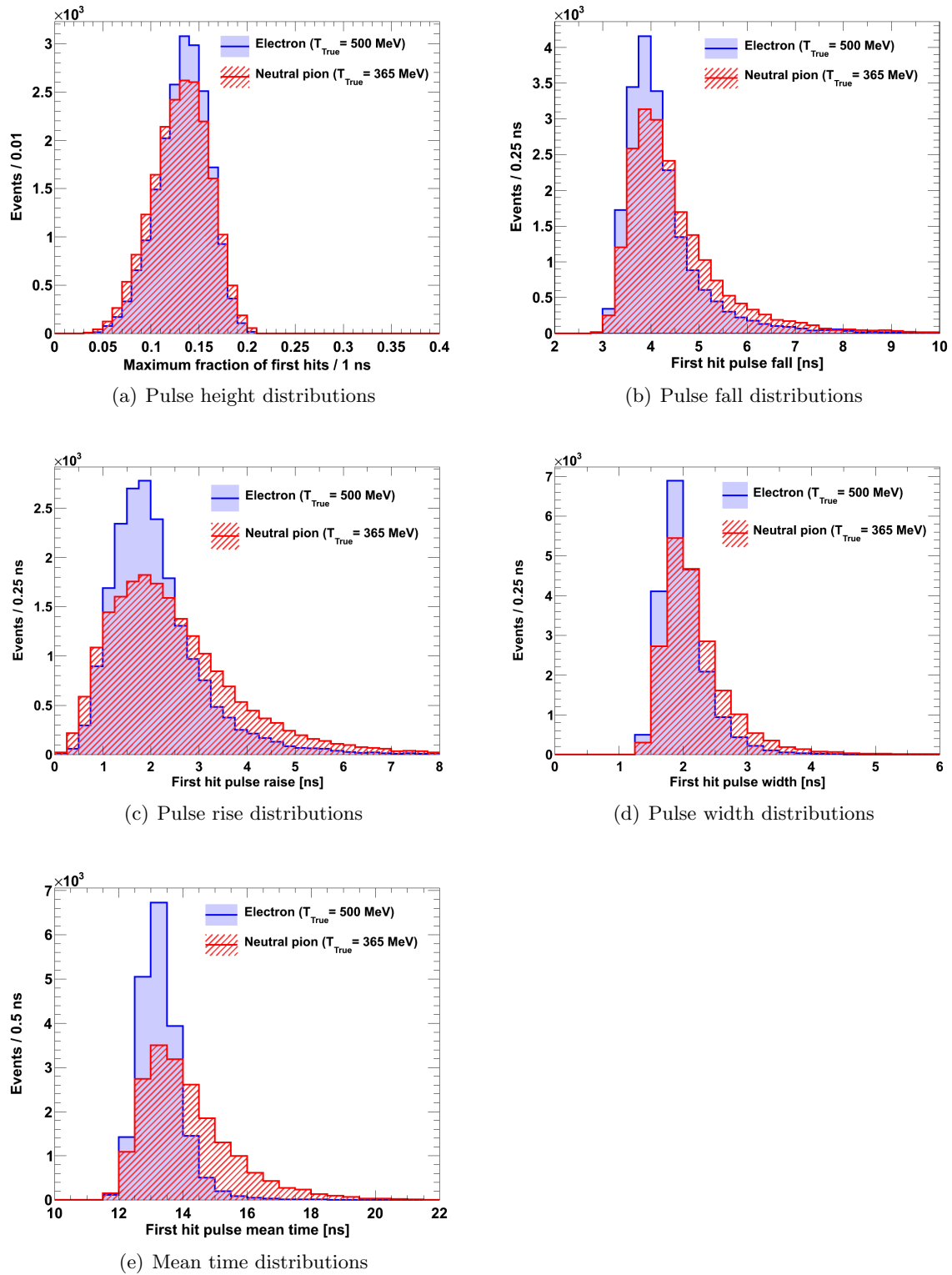


**Figure 5.8:** Distributions of (a) pulse height (b) pulse fall (c) pulse rise (d) pulse width (e) mean time from first hit pulses of 20 k electrons and 20 k neutral pions with 500 MeV true deposited energy.

## 5.5 First hit pulse evolution variables

The pulse shape variables introduced in Section 5.4 rely on the time evolution of the total number of first hits. Motivation to use these variables bases on the expectation of different detector responses for electron and neutral pion events due to differences in the spatial extent of induced electromagnetic showers. Instead of just examining the time development of the total first hit number, one can try to deduce more event information by additionally taking the time-dependent spatial distribution of the first PMT hits into account. Evolution of the first hit pattern at the detector mantle<sup>1</sup> in space and time is referred to as "first hit pulse evolution" in this thesis. It will be further distinguished by evolution along ( $z$ -evolution) and around ( $\varphi$ -evolution) the  $z$ -axis of LENA.

The general idea to use pulse evolution variables for the MVA and the implementation to extract them from underlying data were developed in this work and are discussed in this section.

### 5.5.1 Description of pulse evolution

Figure 5.9 schematically shows the time evolution of a TOF-corrected first hit pattern in the unfolded LENA detector. This pattern is typical for particles propagating in the  $x$ - $y$ -plane. Starting from the PMT with the TOF-corrected first photon hit (FH), the area containing hit PMTs increases in  $\varphi$ - and  $z$ -direction over time (FH  $\rightarrow t_1 \rightarrow t_2$ ) and forms a belt around FH ( $t_3$ ). If the belt is closed, the successive TOF-corrected first hits occur diffuse around the  $z$ -axis.

In order to extract a variable for event classification from first hit pulse evolution, the spatial expansion in  $z$ - and  $\varphi$ -direction of the first hit pulse must be defined and determined at different times. This was realized as follows:

The standard deviations  $\sigma_z$  and  $\sigma_\varphi$  of the  $z$ - and  $\varphi$ -distributions of hit PMTs relative to the point of TOF-corrected first photon hit<sup>2</sup> was used as measure for the pulse's spatial extent in the particular direction. The number of active PMTs ranges from 3500 to 10 000 for deposited energies between 50 MeV and 1 GeV. Therefore, it is difficult to determine  $\sigma_z$  and  $\sigma_\varphi$  after fixed time steps: a small step width leads to little statistics for the first steps, and thus to fluctuations in the determined  $\sigma$ , while larger time steps smear out information. In order to avoid the problem, the first hit times from the PMTs were sorted in ascending order and then divided into ten equal sections  $n_i$ ,  $i = 1, \dots, 10$ . Therefore, each sections  $n_i$  comprised 10 % of the total number of first hits.  $\sigma_z^i(n_i)$  and  $\sigma_\varphi^i(n_i)$ , as well as the mean time of the first hits  $\tau_i(n_i)$  and its standard deviation  $\sigma_\tau^i(n_i)$ , were determined for each sections  $n_i$ .

Figure 5.10(a) and Figure 5.10(b) show examples for part-wise determined  $\sigma_z^i$  and  $\sigma_\varphi^i$  from  $z$ - and  $\varphi$ -distributions of hit PMTs plotted against a section's corrected mean time  $\tau_i^{\text{corr}}(n_i) = \tau_i(n_i) - t_{\text{TOF}}^{\text{fh}}$ . The correction was done with respect to the event's TOF-corrected first PMT hit time  $t_{\text{TOF}}^{\text{fh}}$  in order to shift the evolutions to  $\tau_0^{\text{corr}} = 0$ ,  $\sigma_{z,\varphi}^0 = 0$ . The error of

<sup>1</sup>PMTs at top and bottom caps are not included.

<sup>2</sup>It is important that  $\sigma_z$  and  $\sigma_\varphi$  refer to the PMT with the first TOF-corrected photon hit. Otherwise the standard deviations would depend on the absolute position of the first hit pulse at the detector mantle.

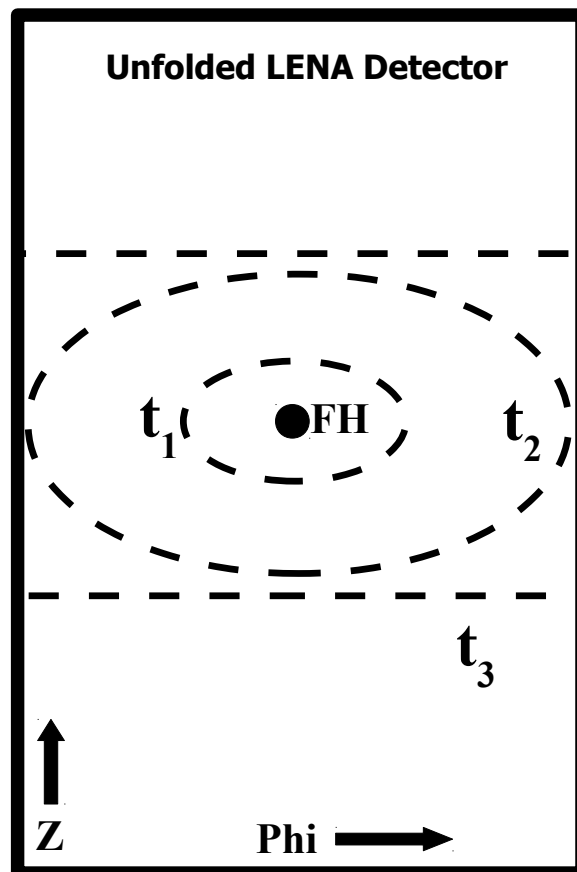


**Figure 5.9:** Schema to describe the time evolution of the TOF-corrected first hit pattern typical for particles propagating in the  $x$ - $y$ -plane. The PMT with the TOF-corrected first photon hit (FH) marks the spatial starting point for the TOF-corrected first hit pulse along the detector mantle. Subsequent TOF-corrected first photon hits to other PMTs occur spatially extended in  $\varphi$ - and  $z$ -direction over time (FH  $\rightarrow$   $t_1$   $\rightarrow$   $t_2$ ). The final TOF-corrected first hit pattern is a belt around FH ( $t_3$ ). Figure not to scale.

the corrected mean time is given by  $\sigma_\tau^i$ .

$z$ -evolution unsteadily rises with increasing  $\tau(n_i)$ . This is due to the fact that almost all of the PMTs at the detector mantle get a first photon hit along the  $z$ -axis consecutively. If the PMT with the first photon hit is located at the center of the detector wall, the pulse of first hits evolves in positive and negative  $z$ -direction, but unlikely reaches all PMTs at the upper and lower side due to the large height of LENA and increasing photon absorption.

For  $\varphi$ -evolution the situation looks differently. Starting from the PMT with the first photon hit, the pulse evolves fast along  $\varphi$ -direction until the other side of the detector wall is reached. This phase corresponds to the rising flank of the  $\varphi$ -evolution in Figure 5.10(b). The evolution's maximum coincides with the section  $n_i$  containing the remaining first PMT hits, which occur on the other side of the detector mantle. These hits correspond to a maximum of  $\sigma_\varphi$ . Diffuse first hits around  $z$ -axis form the tail of  $\varphi$ -evolution.

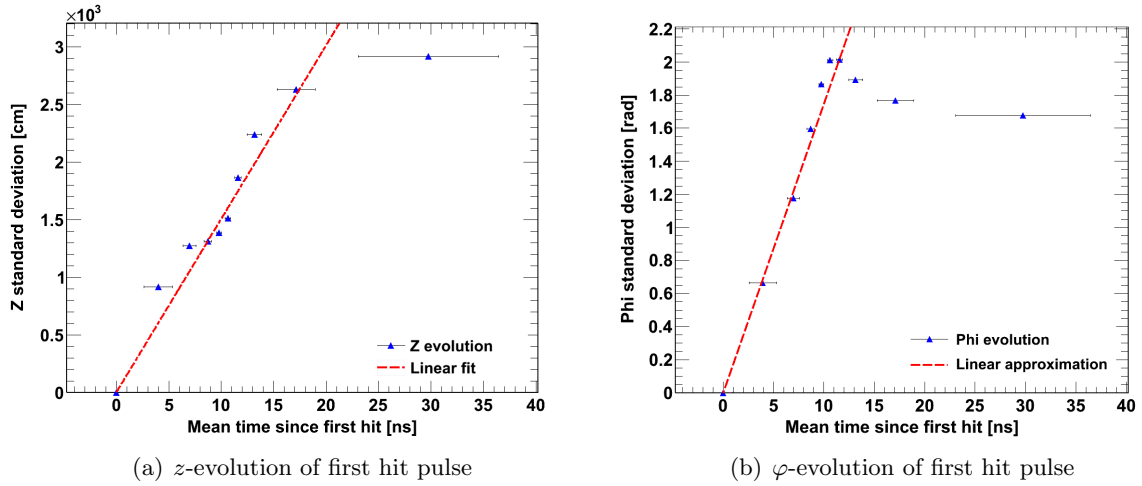


**Figure 5.10:** First hit pulse evolution in (a)  $z$ -direction (b)  $\varphi$ -direction with linear fit / approximation. For details on the idea of pulse evolution see text of Section 5.5.1. The linear fit / approximation is described in Section 5.5.2.

### 5.5.2 Determination of variables from pulse evolution

In order to extract a variable for later MVA classification from pulse evolution, while keeping the algorithm simple for this basic study, the evolutions' relevant sections were linearly approximated. In case of the rising  $z$ -evolution, a linear fit with fixed starting point at  $\tau_0 = 0$ ,  $\sigma_z^0 = 0$  was done taking  $\sigma_\tau^i$  into account. The slope of the linear fit to the  $z$ -evolution was used as MVA variable.

A slightly less computationally intensive procedure was used to obtain the MVA variable for  $\varphi$ -evolution by avoiding the linear fit. The ratio of  $\sigma_\varphi^{\max}/\tau_{\max}(n_{\max})$  of the  $\varphi$ -evolution's maximum value  $\sigma_\varphi^{\max}(n_{\max}) = \max\{\sigma_\varphi^i(n_i)\}$  defines a mean slope for the  $\varphi$ -evolution's rising flank. This mean slope was used as MVA event variable from  $\varphi$ -evolution.

Figure 5.11(a) and Figure 5.11(b) show distributions of the  $z$ - and  $\varphi$ -evolution MVA variables for electrons and neutral pions with a true deposited energy of 500 MeV.

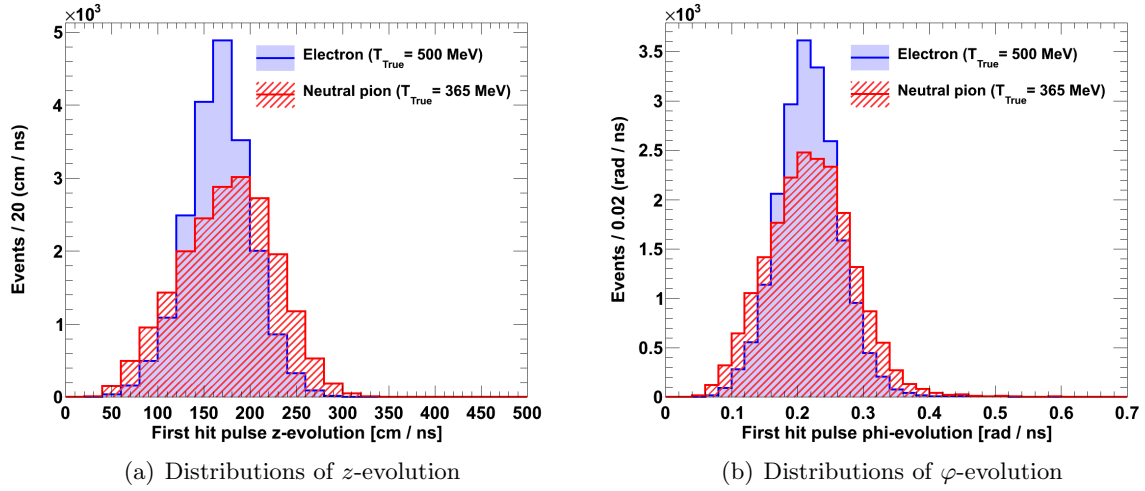


**Figure 5.11:** Distributions of (a)  $z$ -evolution (b)  $\varphi$ -evolution for 20k electrons and 20k neutral pions with a true deposited energy of 500 MeV.

The results indicate that the general idea to use differences in the spatial evolution of first hit pattern for construction of classification variables works and yields useful information. However, a revised version of the algorithm taking into account more details of the pulse evolution than just the linear approximation might improve performance of the evolution variables in MVA. Additionally, an improvement of the algorithm's performance seems possible by doing adjustments to the hardware of the (simulated) detector. As stated in Table 5.2, the used simulation of LENA included 13 742 20 inch PMTs with 12 000 of them distributed at the detector mantle. An increased granularity of the detector's photosensitive area due to more but smaller PMTs would result in an improved spatial resolution. This would help to resolve much smaller differences in the anyway small spatial extents of showering events compared to the large dimensions of LENA.



## Chapter 6

# Multivariate analysis with Boosted Decision Trees

Evaluation of feasibility to use a multivariate analysis technique for discrimination of electron (signal) and neutral pion (background) events in LENA is a major goal of this thesis. The classification of event types bases on a set of variables, which were motivated and introduced in Chapter 5. Different machine-based learning algorithms for MVA exist and distinguish themselves in properties like speed, handling, comprehensibility and performance.

The selection and application of an appropriate classification method was part of this work and is discussed in this chapter. The chosen classifier is an implementation of the BDT<sup>1</sup> algorithm and discussed in Section 6.1. The subject of Section 6.2 are the correlations between the variables used for MVA-based classification introduced in the former chapter and the possible effect on discrimination performance. The final MVA results from two different analysis variants are presented in Section 6.3.

### 6.1 Boosted Decision Trees

BDTs implement a specific machine-based learning algorithm for classification purposes, which uses sequenced cuts on variables to discriminate two or more event classes. They were already used successfully for particle identification in high-energy physics experiments. One example is MiniBooNE [62] at FNAL<sup>2</sup>, which investigated hints for existence of sterile neutrinos [12] by observing electron-neutrino appearance in a muon-neutrino beam. In this case BDTs were used to discriminate background  $\nu_\mu$  events from signal  $\nu_e$  events [80]. The following discussion is mainly based on information given in the last reference.

#### 6.1.1 Functionality of decision trees

A binary decision tree works with a branched sequence of cuts on given event variables  $\mathbf{x}$  (see Figure 6.1). Starting from a root node, the particle events of an analyzed sample are sent through the tree structure until they reach a leaf node, which classifies the event as signal or background like. Before the BDT can be applied to a set of real event data, the tree has

---

<sup>1</sup>BDT: Boosted Decision Tree

<sup>2</sup>FNAL: Fermi National Accelerator Laboratory

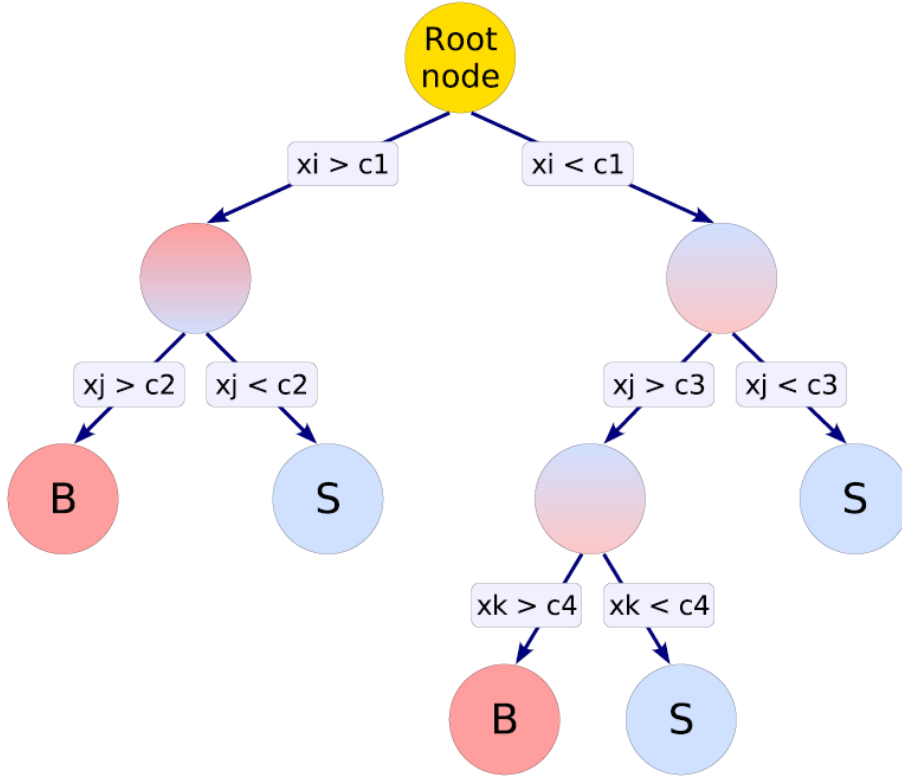


**Figure 6.1:** Starting from the root node of a decision tree, the single nodes are subsequently split into further nodes by cuts on the event variables. The end of a tree's branch is a leaf node, which is either a signal leaf (S) or a background leaf (B). Events are classified according to the leaf node they land on after they were sent through the tree structure. Details about training of decision trees are given in the text. Figure taken from [79].

to be "grown" (trained) by assessing the best branch structure and cut sequence based on a large sample of events of known classes. These signal and background events for the training phase are usually obtained from Monte Carlo simulations. The best structure for a decision tree is defined as a branched sequence of cuts that yields the best separation of signal and background events for the training sample. A criterion describing the quality of separation is the "Gini-index", which is based on the purity  $P$  of a distinct tree node. If one considers a sample of events with unique weights  $w_i$  (see Section 6.1.2), the purity of a node is defined by

$$P = \frac{\sum_s w_s}{\sum_s w_s + \sum_b w_b}, \quad (6.1)$$

where  $\sum_s$  and  $\sum_b$  denote the sums over all signal and background events. From this it follows that  $P(1 - P) = 0$  for a pure signal or background accumulation in the given node. The Gini-index  $G$  of a node with  $n$  events is defined as

$$G = \left( \sum_{i=1}^n w_i \right) \cdot P(1 - P). \quad (6.2)$$

The increase in separation quality by splitting a "father node" into two "child nodes" is

determined by maximization of  $\Delta G$ :

$$\Delta G = G_{\text{father}} - G_{\text{left child}} - G_{\text{right child}} \quad (6.3)$$

For a given Gini-index  $G_{\text{father}}$  of the father node,

$$G_{\text{left child}} + G_{\text{right child}} \quad (6.4)$$

has to be minimized by an appropriate choice for the next cutting variable and value. Splitting of tree nodes ends if the purity of a leaf node reaches a preselected value, usually 0.5. The  $i^{\text{th}}$  event with variable set  $\mathbf{x}_i$  is identified as signal if it ends on a signal leaf. In this case the single decision tree returns a score of  $T(\mathbf{x}_i) = 1$  as response. Otherwise the event is identified as background and the tree returns  $T(\mathbf{x}_i) = -1$ .

Despite the high potential for classification, application of simple decision trees includes a major risk: They are unstable, meaning that they are easily affected by statistical fluctuations in the training sample. If the tree structure is adapted to these fluctuations, the classification performance for test or real data is deteriorated with respect to training data. In this case the classifier is considered "overtrained". This potential problem is avoided by using the responses of several different decision trees, a "forest", basing classification on a "majority vote".

### 6.1.2 Boosting of decision trees

The performance of decision tree forests can be improved by using the output of grown decision trees for training of subsequent trees. All decision trees are trained on basis of the same training events forming the training sample. If an event is misidentified in the growing phase of a tree, its weight is increased (boosted). The same training sample with renormalized, new event weights is then used to train the next tree. This procedure is referred to as boosting of decision trees. Several methods for boosting exist and they differ in calculation of the new event weights (cf. [80]).

AdaBoost<sup>1</sup> [81] is one possible boosting algorithm and was applied to the BDTs used in this work.  $M$  decision trees, individually indexed by  $m$ , shall be trained with a sample of  $N$  events, initially weighted by  $1/N$ . The following denotations are defined:

- $\mathbf{x}_i$  is the set of variables for the  $i^{\text{th}}$  event.
- $y_i$  is 1 if the  $i^{\text{th}}$  event is a signal event, and  $-1$  if it is a background event.
- $w_i$  is the weight of the  $i^{\text{th}}$  event.
- The result of the  $m^{\text{th}}$  tree,  $T_m(\mathbf{x}_i)$ , is 1 if the variables of the  $i^{\text{th}}$  event make it end on a signal leaf of the  $m^{\text{th}}$  tree, and is  $-1$  if it ends on a background leaf.
- $I(y_i \neq T_m(\mathbf{x}_i))$  describes a misidentification by the  $m^{\text{th}}$  tree and is 1 if  $y_i \neq T_m(\mathbf{x}_i)$ , and 0 if  $y_i = T_m(\mathbf{x}_i)$ .

---

<sup>1</sup>AdaBoost: Adaptive Boost

The misclassification rate  $\text{err}_m$  of the  $m^{\text{th}}$  tree is defined as

$$\text{err}_m = \frac{\sum_{i=1}^N w_i I(y_i \neq T_m(\mathbf{x}_i))}{\sum_{i=1}^N w_i}. \quad (6.5)$$

It is used to calculate the "boost weight"  $\alpha_m$  coming from the  $m^{\text{th}}$  tree:

$$\alpha_m = \beta \times \ln((1 - \text{err}_m)/\text{err}_m), \quad (6.6)$$

where  $\beta$  is a parameter to adjust the boosting from outside the algorithm<sup>1</sup>. The boost weight  $\alpha_m$  changes the weight of each event  $i$ ,  $i = 1, \dots, N$ , according to

$$w_i \mapsto w_i \times \exp(\alpha_m I(y_i \neq T_m(\mathbf{x}_i))). \quad (6.7)$$

All event weights are renormalized with respect to the sum over all new and old weights,

$$w_i \mapsto \frac{w_i}{\sum_{i=1}^N w_i}. \quad (6.8)$$

The total result for a given event  $i$  is the weighted sum of the results (scores) of the individual trees:

$$T(\mathbf{x}_i) = \sum_{m=1}^M \alpha_m T_m(\mathbf{x}_i). \quad (6.9)$$

The scores for all  $N$  training events can always be normalized to be in the interval  $[-1, 1]$ :

$$T_{\text{norm}}(\mathbf{x}_i) = \frac{\sum_{m=1}^M \alpha_m T_m(\mathbf{x}_i)}{\sum_{m=1}^M \alpha_m}. \quad (6.10)$$

Discrimination of signal and background events is then done statistically by defining a cut  $c \in [-1, 1]$  on the output distribution of the BDT classifier:

$$\begin{aligned} T_{\text{norm}}(\mathbf{x}_i) < c &\implies i^{\text{th}} \text{ event is background} \\ T_{\text{norm}}(\mathbf{x}_i) \geq c &\implies i^{\text{th}} \text{ event is signal} \end{aligned}$$

Some events are accepted / rejected by the cut although they are background / signal. If  $N_y^{\text{acc}}$  is the number of accepted events of class  $y = s, b$  and  $N_y$  is the total number of this class's events, then the efficiency  $\epsilon_y$  is defined as

$$\epsilon_y = \frac{N_y^{\text{acc}}}{N_y}. \quad (6.11)$$

The rejection  $\rho_y$  is defined as

$$\rho_y = 1 - \epsilon_y. \quad (6.12)$$

Therefore, the best cut value  $c$  is determined by maximization of the signal-to-background-ratio  $\epsilon_s(c)/\epsilon_b(c)$ .

---

<sup>1</sup>The standard value is  $\beta = 1$ .

### 6.1.3 Overtraining

As already mentioned in Section 6.1.1, decision trees are sensitive to statistical fluctuations in the training sample. Instead of extracting general information from the event sample as basis for classification, the algorithm starts to memorize the training data in order to achieve maximum signal and background separation. As a consequence of this, the decision tree shows excellent but too optimistic discrimination performance when analyzing training events, and yields diminished classification efficiency when analyzing unknown data. In this case the decision tree is considered as "overtrained"<sup>1</sup>. Overtraining occurs when the decision tree's number of degrees of freedom is larger than the variety of useful information provided by the data of the training sample.

Combining and boosting decision trees helps to reduce the vulnerability to overtraining though does not remove it completely. The detection of overtraining is not always easy, as there is no universal rule how to reveal it.

One approach is to compare the classification results of the training sample with the results of a second, statistically independent test sample. If they are equal, the impact of overtraining is insignificant. An additional K-S-test<sup>2</sup> (see [82]) with the BDTs' output distributions of both samples determines the likelihood of the output distribution for the test sample to the training sample. Therefore, a high likelihood value indicates that the BDTs did not adapt to fluctuations in the training sample and overtraining is negligible.

Another approach is to remove statistically unimportant branches from the BDTs on basis of complex algorithms and thereby make them more general. However, this so-called "pruning" was not used in the present MVA.

## 6.2 Correlations between the MVA variables

The correlation between event variables describes their statistical relation towards each other. Contrary to proportionality relations, correlations only allow to infer from a variable's value on the other variable's value on a statistical mean. For a MVA the ideal case is given if all variables are uncorrelated and thus contribute independent information on the analyzed event. If, on the other hand, correlations are present, the analysis of additional event variables does not necessarily yield new information.

The degree of linear correlation between two variables is expressed in terms of a linear correlation coefficient (cf. [83]). For the present MVA based on the nine variables introduced in Chapter 5, the correlations matrices from training samples are shown separately for signal and background events in Figure 6.2 and Figure 6.3.

The presence of correlations degrades the classification performance of BDTs. As described in Section 6.1.1, decision trees work on basis of a branched sequence of cuts. Cut variables and values are optimized towards best separation of signal and background distribution. If variables are correlated, an explicit cut on one variable also involves an implicit cut

<sup>1</sup>The problem of possible overtraining is not inherent only to decision trees, but also to other classifiers like artificial neural networks.

<sup>2</sup>K-S: Kolmogorov-Smirnov

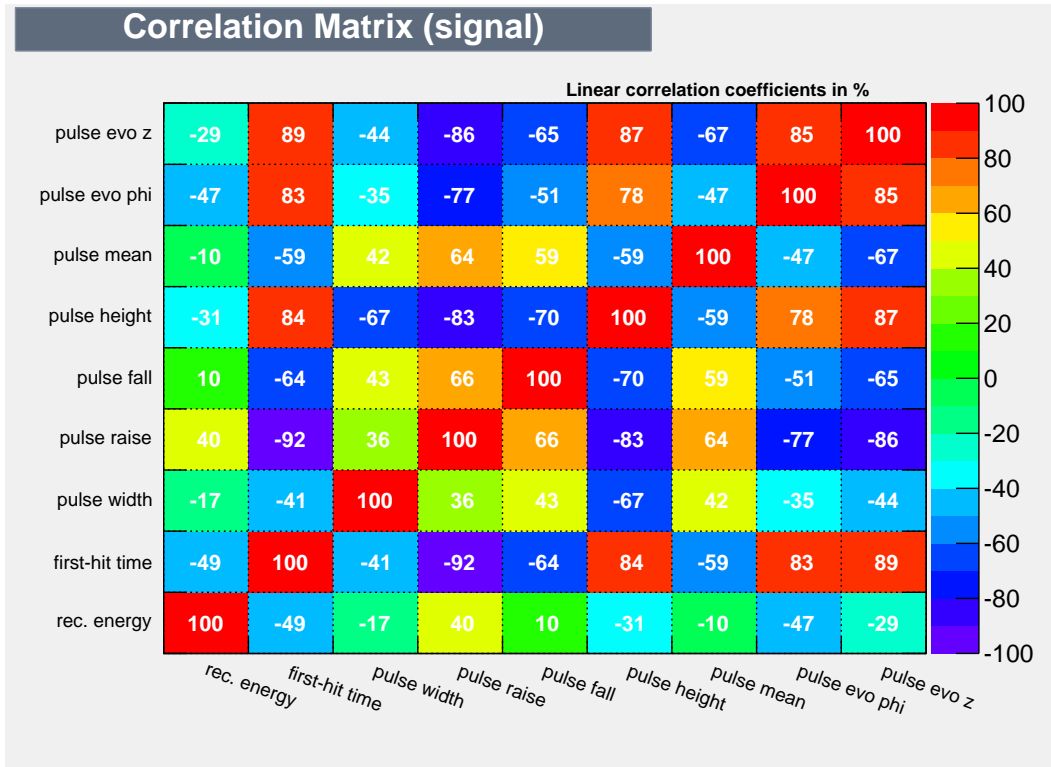


**Figure 6.2:** Correlation matrix with linear correlation coefficients for the used MVA variables on basis of a training sample with signal events. Figure created with TMVA [79].

on a correlated variable in the statistical mean. Therefore, a BDT's structure is possibly affected by correlations between variables in the training sample. If the same correlations are not present in a test sample or real data, but the tree structure is adapted to them, discrimination performance is degraded.

As one can see from Figure 6.2 and Figure 6.3, strong correlations between the variables in the signal and in the background training sample exist. This was expected, as many variables base on the same fundamental information of TOF-corrected PMT hit times. Especially the variables derived from the event's pulse shape show correlations, as they all parameterize the same characteristic form (cf. Figure 5.6(a)) of an event's first hit pulse. The TOF-correction applied to the PMT hit times reduced the position-dependence of the pulse shape and thus suppressed uncorrelated form variances making the pulse more typical for the different particle types.

Reduction of variable correlations is possible by removing or combining single variables for the MVA. As a positive side-effect, the MVA get less complex and one has to consider systematic effects on fewer variables during analysis. Furthermore, linear correlations can be removed by transformation of the variable tuple  $\mathbf{x}$  with the square-root  $C'$  of the covariance matrix  $C$  [79]:

$$\mathbf{x} \mapsto (C')^{-1} \mathbf{x}, \quad (C')^2 = C \quad (6.13)$$

In presence of strong non-linear correlations this technique can yield contrary effects and

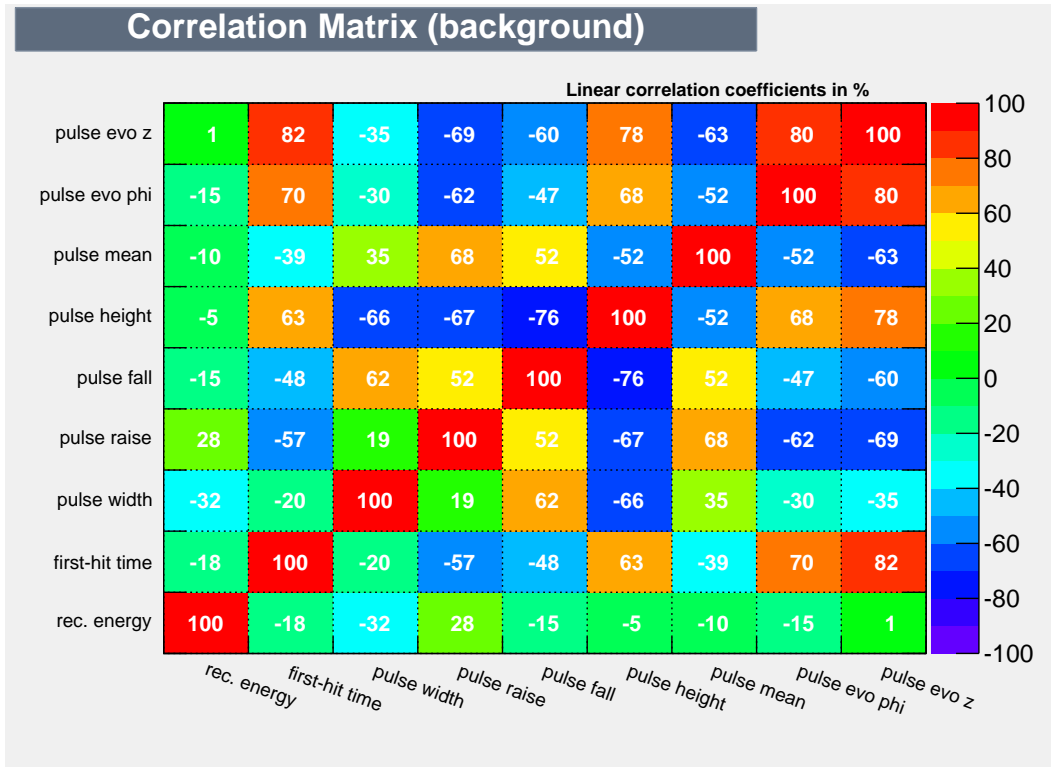


**Figure 6.3:** Correlation matrix with linear correlation coefficients for the used MVA variables on basis of a training sample with background events. Figure created with TMVA [79].

deteriorate classification performance. Nevertheless, the decorrelation technique was used in this work as it had positive influence on the discrimination performance in preceding MVA test runs.

### 6.3 MVA settings and results

In this section the settings of the MVA method, its procedure and the obtained results are presented. It was the aim of the analysis to assess the potential to discriminate electron and neutral pion events in LENA by using BDTs as MVA method and to provide first quantitative results on basis of a simplified Monte Carlo study. No effort was made to tune the BDT parameters systematically for maximal classification performance, like it was done in [80]. This is justified, as no real data requiring analysis exist and the simplified Monte Carlo study was expected to yield optimistic results per se.

Two different procedures using BDTs for event classification were evaluated on basis of Monte Carlo data. At first a general analysis was done, including the entire samples of simulated electron and neutral pion events (see Section 6.3.1). The second analysis, treated in Section 6.3.2, aimed to determine the energy dependence of the discrimination performance by restricting the MVA to sub-samples of events in defined energy ranges. Both procedures were based on mutual conditions and BDTs settings, which will be introduced in the following.

The generation of event samples used for the MVA was discussed in Section 5.1.2. The

samples comprised 213 491 electron events as signal and 210 000 neutral pion events as background. All events started in the center of the detector with negative  $x$ -axis as momentum direction. The flat spectra of true deposited energy ranged from 135 MeV to 1 GeV for both samples.

One pre-selection cut was applied to electrons and neutral pions: As discussed in Section 5.4.6, the distributions of the first hit pulse's mean time for electrons and neutral pions cluster around a few nanoseconds. However, there is a subclass of events featuring values of several microseconds, probably due to subsequent decay processes. Therefore, events with mean times above 25 ns were for the moment excluded from the present analysis for simplicity. They could be easily included in the MVA as soon as an algorithm for the separation of subsequent events is available. The cut value of 25 ns is chosen to be right at the start of the mean time distributions' tails. 208 742 ( $\sim 97.7\%$ ) electrons and 203 491 ( $\sim 96.9\%$ ) neutral pions remained after the cut.

BDTs based on the TMVA-package<sup>1</sup> [79] were implemented in the analysis. The following important settings were fixed as standard in all analysis runs and mostly coincide with the default values for BDTs of TMVA:

- *Minimum number of events per tree node:* 500 — Minimum number of events allocated to a new child node due to a node split.
- *Boost type:* AdaBoost — Calculation of the boost weight (see Section 6.1.2).
- *Boost factor:* AdaBoost  $\beta = 1.0$  — External factor to adjust the boosting strength (see Equation 6.6).
- *Separation type:* Gini-index — Criterion to evaluate the best cut variable and cut value for node splitting (see Equation 6.2).
- *Number of cuts:* 20 — Number of different cuts to find the best cut variable and cut value.
- *Prune method:* No pruning — Algorithm to remove statistically unimportant branches from trees (see Section 6.1.3).
- *Variable transformation:* Decorrelation — Transformation applied to the event variables before the MVA (see Section 6.2).

The number of trained trees and their maximum depth was set differently in both analysis procedures and is therefore stated in the corresponding section. Following an advice given in [79], small unpruned trees were trained instead of large pruned ones.

### 6.3.1 General analysis

Basis for evaluation of the BDTs' discrimination performance is the relation between signal efficiency  $\epsilon_s(c)$  and background rejection  $\rho_b(c)$ . Both quantities depend on the cut  $c$  applied to the BDTs' output distribution. This relation is visualized by the classifier's ROC<sup>2</sup> curve. An example for a classifier based on 400 BDTs is shown in Figure 6.4.

<sup>1</sup>TMVA is integrated into the ROOT analysis framework [74].

<sup>2</sup>ROC: Receiver operating characteristic

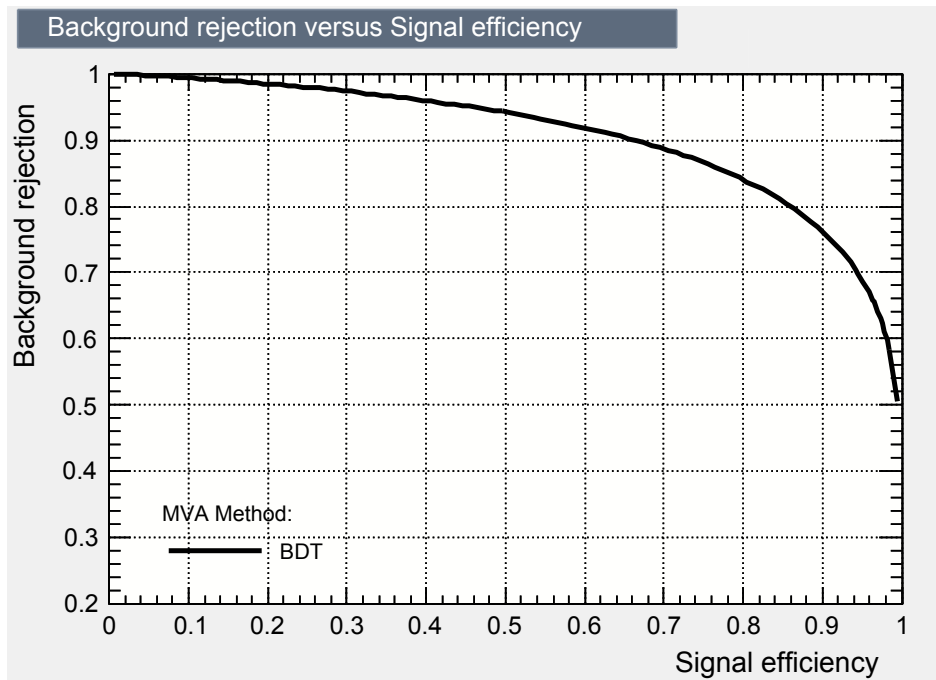


**Figure 6.4:** ROC curve of a BDT classifier based on 400 single trees with a maximum depth of 3. Figure created with TMVA [79].

If a classifier is trained for a later analysis of real events, it is the goal to optimize the classifier's settings in order to maximize the area under the ROC curve. At the same time, one has to make sure that the classifier is not excessively overtrained. Number and depth of BDTs are important parameters to influence the performance, but they also affect overtraining as they determine the classifier's degrees of freedom.

In order to detect overtraining (see Section 6.1.3), the event sample was randomly split into two equal parts. One part was used as training sample, the other part was used to determine the classifier's performance on unknown data. Furthermore, a K-S-test based on the output distributions of training and test sample was performed.

In the given context, the analysis was not intended to produce a single, systematically optimized classifier for application on real data, but rather aimed for assessment of discrimination performance of BDTs in general. Therefore, different settings for number of BDTs per classifier and maximum depth of a BDT were used to investigate the impact of these parameters on the ROC curve and the results from overtraining tests. The following parameter values were used:

- Number of BDTs per classifier: 25, 100 and 400
- Maximum depth of a BDT: 2 and 3

Preceding tests with different TMVA-settings for BDTs showed an unexpected behavior for results from equally trained classifiers: The performance of a classifier and the results from overtraining tests considerably changed for different event compositions of training and test samples as these were built by randomly splitting the entire event sample. An example for the output distribution of a BDT classifier with high likelihood values for signal and

background from K–S-test is shown in Figure 6.5. The results from another BDT classifier with the same settings, but different compositions of test and training sample, are shown in Figure 6.6. One notices the decreased likelihood value from K–S-test. A possible explanation for this effect is the influence of different correlations in the randomly composed event samples (cf. Section 6.2).

The observed dependency of a classifier’s output on the composition of training and test samples complicated assessing the discrimination performance of BDTs on basis of a single classifier. For this reason, the mean discrimination performance was determined by averaging over results from 10 classifiers, each of them trained with the same settings but randomly selected events for training and testing. The results from a single classifier to average over comprised the signal efficiencies at benchmark points of 70 %, 90 % and 99 % background rejection from training and test sample. Also the likelihood values from K–S-tests for signal and background were averaged. The resulting mean values with their standard deviations for different setting combinations are summarized in Table 6.1.

The procedure was repeated excluding reconstructed energy from the MVA variables. This effectively reduced the dimension of variable space by one and provided less event information to the classifier. Furthermore, it evaluated the importance of the reconstructed energy as MVA variable. The corresponding results are summarized in Table 6.2.

In case of the general analysis, the signal efficiency mean values of the test samples and for different parameter settings at background rejection levels of 70 %, 90 % and 99 % range from 94.1 % to 85.5 %, from 65.3 % to 49.6 % and from 14.2 % to 8.8 %. The upper limits of the ranges correspond to classifiers with 400 BDTs of depth 3 and mark the best results. Corresponding ranges for the analysis excluding reconstructed event energy as MVA variable are 91.4 % to 83.3 %, 60.7 % to 47.2 % and 12.7 % to 8.4 %. Again, the best efficiency values come from classifiers with 400 BDTs of depth 3.

The comparison of the resulting signal efficiencies for fixed background rejection benchmarks shows higher values for an increased number of trees and tree depths. Except the result for 400 trees and maximum depth 3 at 99 % background rejection in Table 6.1, all efficiency mean values from the test samples are in good agreement with the mean values from the training samples. This is especially true if one takes the standard deviations into account. In most cases the test efficiencies are slightly below or just equal to the training efficiencies. This hints towards an on average negligible impact of overtraining. However, significance of the averaged results from K–S-tests regarding overtraining is difficult to estimate due to the large error ranges.

Comparing the results of Table 6.1 and Table 6.2, the positive impact of including the event’s reconstructed energy in the MVA classification is clearly demonstrated. Signal efficiencies are lower in all cases if the reconstructed energy is removed as variable. Furthermore, the standard deviations of the determined mean efficiency values decrease with increasing values for the setting parameters if the reconstructed energy is included. Without, this is only the case for settings with a maximum tree depth equal to 3.

As a result, the best discrimination performance was achieved for 400 BDTs of depth 3 with

signal efficiencies of 94.1 %, 65.3 % and 14.2 % at background rejection levels of 70 %, 90 % and 99 %.

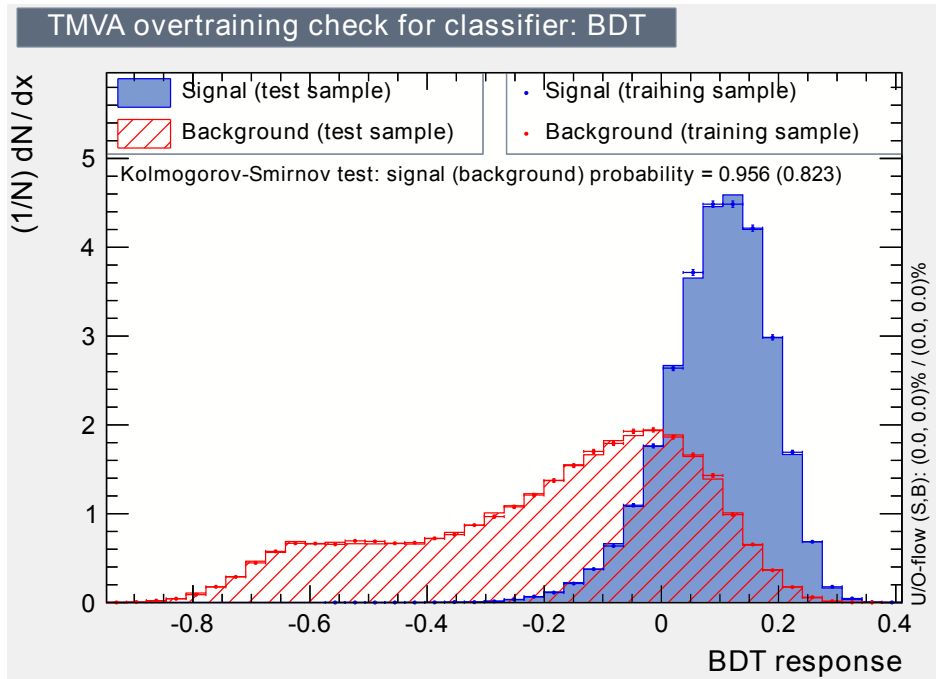


**Figure 6.5:** Output distribution of a BDT classifier with 100 single trees of maximum depth 2. The likelihood results from K–S-test are 0.956 (0.823) for signal (background). Figure created with TMVA [79].

### 6.3.2 Energy-dependent analysis

In addition to the general analysis done in Section 6.3.1, the energy-dependent performance of BDT classifiers was investigated. The procedure remained the same as in the general case, but several sub-samples of events in defined ranges of true deposited energy were used for the MVA (see Table 6.3). As before, these sub-samples were subdivided into training and test samples. 10 classifiers were trained and their results for signal efficiencies at distinct benchmark points of background rejections averaged. The number of trees per BDT classifier was set to 100, each of the trees had a maximum depth of 3. Reconstructed energy was always included as MVA variable. Table 6.4 shows the averaged results for signal efficiencies and K–S-test likelihoods in different energy ranges. Furthermore, the averaged signal efficiencies for background rejections of 70 %, 90 % and 99 % are visualized in Figure 6.7, Figure 6.8 and Figure 6.9.

As in the case of general analysis, the signal efficiency mean values for training and test samples are in good agreement. One exception is the energy range from 135 MeV to 200 MeV. Averaged efficiency results indicate overtrained classifiers in this range, as the mean values from test samples are considerably lower than values from training samples at 99 % background rejection. The probable reason is the small size of the training sample for that energy range (see Table 6.3), which leads to adaptation of the classifiers' degrees of freedom to statistical fluctuations in the small sample. Likelihood values from K–S-test for

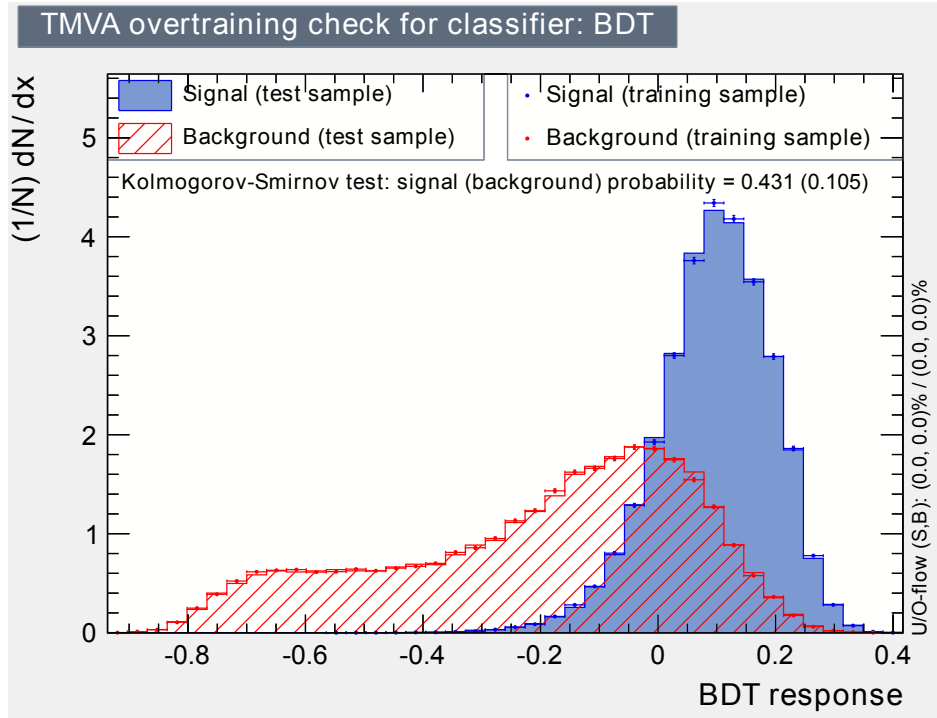


**Figure 6.6:** Output distribution of a BDT classifier with 100 single trees of maximum depth 2. The likelihood results from K-S-test are 0.431 (0.105) for signal (background). Figure created with TMVA [79].

**Table 6.1:** Results from the general analysis using the reconstructed event energy as MVA variable. The averaged signal efficiencies for different classifier settings are shown for training (Train) and test (Test) samples at benchmark points of 70 %, 90 % and 99 % background rejection. Furthermore, the averaged likelihood values for signal (Sig.) and background (Bkg.) from K-S-test are summarized.

Settings	Signal efficiency at background rejection level						K-S likelihood	
	70 % (Test)	70 % (Train)	90 % (Test)	90 % (Train)	99 % (Test)	99 % (Train)	Sig.	Bkg.
25 Trees Depth 2	85.5 % ±1.1 %	85.6 % ±1.0 %	49.6 % ±1.2 %	50.0 % ±1.3 %	8.8 % ±1.0 %	8.8 % ±1.0 %	57.3 % +26.5 % -26.5 %	44.8 % +28.5 % -28.5 %
25 Trees Depth 3	87.9 % ±0.9 %	87.8 % ±0.8 %	53.3 % ±1.3 %	53.7 % ±1.5 %	10.2 % ±0.9 %	10.2 % ±0.9 %	64.2 % +32.9 % -32.9 %	47.3 % +33.5 % -33.5 %
100 Trees Depth 2	89.0 % ±0.9 %	88.9 % ±0.8 %	54.3 % ±1.4 %	54.3 % ±1.4 %	9.9 % ±0.6 %	10.1 % ±0.6 %	64.5 % +34.0 % -34.0 %	72.4 % +27.6 % -27.7 %
100 Trees Depth 3	92.0 % ±0.6 %	92.1 % ±0.6 %	60.1 % ±1.1 %	60.5 % ±1.1 %	11.5 % ±1.0 %	11.8 % ±0.9 %	35.9 % +28.8 % -28.8 %	59.9 % +27.8 % -27.8 %
400 Trees Depth 2	91.9 % ±0.5 %	92.0 % ±0.5 %	59.3 % ±1.0 %	59.6 % ±1.1 %	11.3 % ±0.5 %	11.6 % ±0.7 %	81.8 % +18.2 % -21.8 %	62.5 % +31.1 % -31.1 %
400 Trees Depth 3	94.1 % ±0.2 %	94.3 % ±0.3 %	65.3 % ±0.4 %	65.8 % ±0.6 %	14.2 % ±0.6 %	15.2 % ±0.3 %	72.6 % +27.4 % -33.7 %	50.9 % +28.9 % -28.9 %

**Table 6.2:** Results from the general analysis excluding reconstructed energy as MVA variable. The averaged signal efficiencies for different classifier settings are shown for training (Train) and test (Test) samples at benchmark points of 70 %, 90 % and 99 % background rejection. Furthermore, the averaged likelihood values for signal (Sig.) and background (Bkg.) from K–S-test are summarized.

Settings	Signal efficiency at background rejection level						K–S likelihood	
	70 % (Test)	70 % (Train)	90 % (Test)	90 % (Train)	99 % (Test)	99 % (Train)	Sig.	Bkg.
25 Trees Depth 2	83.3 % ±1.1 %	83.2 % ±1.2 %	47.2 % ±1.2 %	47.1 % ±1.3 %	8.4 % ±0.5 %	8.3 % ±0.5 %	57.2 % $^{+33.8}_{-33.8}$ %	58.2 % $^{+34.7}_{-34.7}$ %
25 Trees Depth 3	86.0 % ±0.8 %	86.0 % ±0.8 %	51.5 % ±1.0 %	51.6 % ±1.2 %	9.3 % ±0.8 %	9.5 % ±0.8 %	47.0 % $^{+26.6}_{-26.6}$ %	56.2 % $^{+37.5}_{-37.5}$ %
100 Trees Depth 2	85.7 % ±1.2 %	85.6 % ±1.2 %	50.8 % ±2.0 %	50.5 % ±1.7 %	9.2 % ±0.6 %	9.1 % ±0.7 %	75.9 % $^{+24.1}_{-34.4}$ %	56.2 % $^{+30.6}_{-30.6}$ %
100 Trees Depth 3	89.1 % ±0.6 %	89.2 % ±0.7 %	56.9 % ±1.1 %	57.1 % ±1.4 %	11.2 % ±0.6 %	11.2 % ±0.5 %	60.7 % $^{+33.8}_{-33.8}$ %	63.3 % $^{+27.2}_{-27.2}$ %
400 Trees Depth 2	87.8 % ±1.4 %	87.8 % ±1.5 %	53.9 % ±2.5 %	53.9 % ±2.5 %	10.1 % ±0.8 %	10.2 % ±0.9 %	72.7 % $^{+27.3}_{-33.4}$ %	77.1 % $^{+22.9}_{-27.1}$ %
400 Trees Depth 3	91.4 % ±0.4 %	91.6 % ±0.4 %	60.7 % ±0.5 %	61.2 % ±0.5 %	12.7 % ±0.3 %	13.1 % ±0.4 %	53.2 % $^{+35.6}_{-35.6}$ %	60.4 % $^{+32.5}_{-32.5}$ %

signal and background show large standard deviations and thus make it difficult to assess significance of these results regarding overtraining.

The ranges of signal efficiency mean values for energies from  $(167.5 \pm 65)$ MeV to  $(900 \pm 100)$ MeV at background rejection levels of 70 %, 90 % and 99 % are 94.9 % to 91.8 %, 73.8 % to 58.0 % and 23.1 % to 11.2 % for the test sample.

Dependency of discrimination performance on true deposited energy is visible at all three benchmark points and is especially distinctive at the investigated benchmark point of 90 % background rejection: The signal efficiencies considerably decrease with rising true deposited energy (see Figure 6.7 to Figure 6.9). This result was expected, as the increased energy of neutral pions allowed smaller opening angles of photons from the pion’s decay (see Section 4.2.2). Smaller opening angles allow more overlap between resulting electromagnetic showers which are in turn harder to distinguish from a shower induced by a single electron.

A comparison of the corresponding results from general analysis for 100 trees of depth 3 per classifier (see Table 6.1) with the results from present analysis shows that mean values from the former analysis are substantially lower. This can be explained by interpreting the corresponding efficiency values from general analysis, 92.0 %, 60.1 % and 11.5 %, as mean values for the entire inspected energy range. The mean values from averaging over the results of the energy-dependent analysis are  $(93.3 \pm 1.1)\%$ ,  $(64.7 \pm 2.7)\%$  and  $(15.1 \pm 2.9)\%$ . These values are in good agreement to those of the general analysis if one considers the impact of the overtrained first energy bin.

Furthermore, introduction of energy cuts resulted in ”boundary effects”, as the single clas-

sifiers from energy-dependent analysis automatically adapted to a specific energy range and stayed unaffected by events just below or above the energy cut. This automatic adaption and the classifiers' artificial "blindness" to possibly similar events beyond the cuts leads to an increased signal efficiency at a given background rejection. In addition, one has to take the reduced sample sizes for training and testing into account (see Table 6.3).

**Table 6.3:** Samples sizes after cuts on true deposited energy. Each sub-samples was again divided into training and test sample for MVA.

True energy range	Number of electron events	Number of neutral pion events
135 MeV to 200 MeV	16 144	15 797
200 MeV to 400 MeV	48 999	47 703
400 MeV to 600 MeV	48 145	46 820
600 MeV to 800 MeV	47 999	46 670
800 MeV to 1000 MeV	47 455	46 501

**Table 6.4:** Results from energy-dependent analysis with 100 trees of maximum depth 3 per BDT classifier. The averaged signal efficiencies for different true deposited energy ranges are shown for training (Train) and test (Test) samples at benchmark points of 70 %, 90 % and 99 % background rejection. Furthermore, the averaged likelihood values for signal (Sig.) and background (Bkg.) from K-S-test are summarized.

True energy range	Signal efficiency at background rejection level						K-S likelihood	
	70 % (Test)	70 % (Train)	90 % (Test)	90 % (Train)	99 % (Test)	99 % (Train)	Sig.	Bkg.
135 to 200 MeV	94.9 % ±0.4 %	95.2 % ±0.5 %	73.8 % ±1.5 %	75.3 % ±1.3 %	23.1 % ±2.2 %	27.4 % ±2.2 %	33.4 % $^{+27.5}_{-27.5}$ %	52.5 % $^{+31.1}_{-31.1}$ %
200 to 400 MeV	94.0 % ±0.4 %	94.0 % ±0.4 %	67.5 % ±0.8 %	68.1 % ±1.2 %	14.7 % ±0.7 %	15.3 % ±1.4 %	68.2 % $^{+27.8}_{-27.8}$ %	67.9 % $^{+27.2}_{-27.2}$ %
400 to 600 MeV	93.3 % ±0.5 %	93.3 % ±0.5 %	63.4 % ±1.4 %	63.8 % ±1.1 %	13.4 % ±1.3 %	14.1 % ±0.8 %	78.5 % $^{+21.5}_{-23.7}$ %	62.9 % $^{+32.0}_{-32.0}$ %
600 to 800 MeV	92.3 % ±0.5 %	92.5 % ±0.5 %	60.8 % ±0.8 %	61.4 % ±1.3 %	13.2 % ±1.1 %	14.0 % ±1.4 %	63.1 % $^{+34.4}_{-34.4}$ %	60.3 % $^{+28.6}_{-28.6}$ %
800 to 1000 MeV	91.8 % ±0.6 %	91.8 % ±0.6 %	58.0 % ±1.3 %	58.7 % ±1.2 %	11.2 % ±0.6 %	11.7 % ±0.6 %	73.1 % $^{+26.9}_{-28.9}$ %	47.5 % $^{+26.8}_{-26.8}$ %

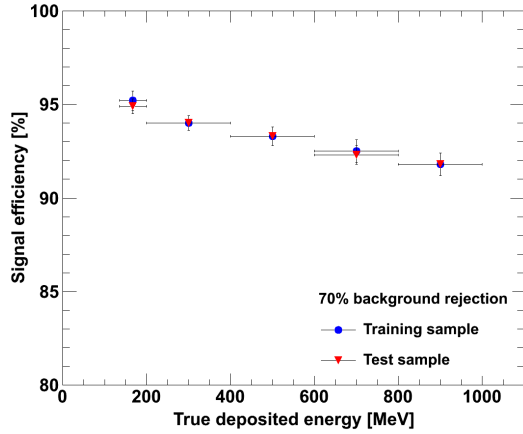


**Figure 6.7:** Mean values and standard deviations of signal efficiencies from energy-dependent analysis for 70% background rejection. Values were obtained by averaging over results of 10 BDT classifiers with 100 trees of maximum depth 3 per classifier. The results of the first energy bin are possibly affected by overtrained classifiers (see text).

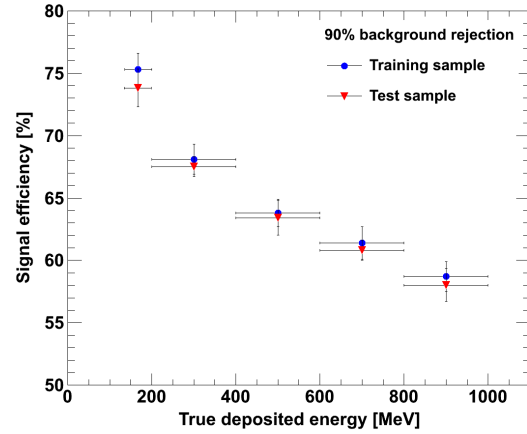


**Figure 6.8:** Mean values and standard deviations of signal efficiencies from energy-dependent analysis for 90% background rejection. Values were obtained by averaging over results of 10 BDT classifiers with 100 trees of maximum depth 3 per classifier. The results of the first energy bin are possibly affected by overtrained classifiers (see text).

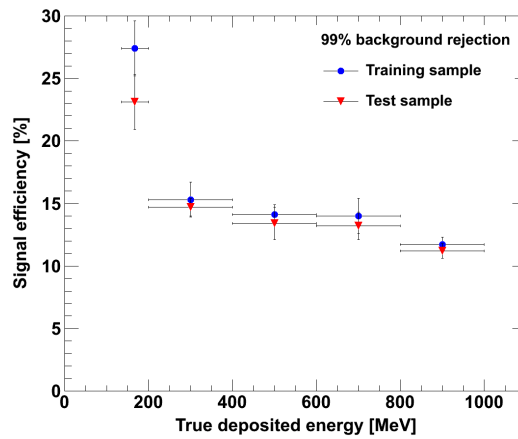


**Figure 6.9:** Mean values and standard deviations of signal efficiencies from energy-dependent analysis for 99% background rejection. Values were obtained by averaging over results of 10 BDT classifiers with 100 trees of maximum depth 3 per classifier. The results of the first energy bin are possibly affected by overtrained classifiers (see text).



## Chapter 7

# Conclusion and Outlook

Within the framework of this thesis, the feasibility to discriminate NC neutral pion and CC  $\nu_e$  events in the 50 kt liquid scintillator detector LENA [32] was investigated for energies up to 1 GeV. Neutral pions dominantly decay into two photons. If these photons cannot be identified as separate particles, their combined event signature is indistinguishable from an electron event. This circumstance introduces an important background to oscillation experiments searching for  $\bar{\nu}_e$  appearance in a  $\bar{\nu}_\mu$  beam.

In the LAGUNA-LBNO project, the application of LENA as a far detector for a long-baseline neutrino oscillation experiment with a  $\bar{\nu}_\mu$  beam is studied. The sensitivity of a long-baseline experiment with LENA regarding the mixing angle  $\theta_{13}$ , the CP-violating phase  $\delta_{CP}$  and the neutrino mass hierarchy was investigated with GLoBES. The assumed baseline of 2288 km from CERN to Pyhäsalmi in Finland shows great potential to measure all three parameters if the NC background can be sufficiently rejected. In case a NC background rejection of 99 % is achieved, the minimum values of  $\sin^2 2\theta_{13}$  range from 0.002 to 0.01 for signal efficiencies from 90 % to 15 % in order to measure  $\theta_{13}$  at  $3\sigma$  CL for at least 50 % of possible  $\delta_{CP}$  values. The corresponding values for sensitivity on the mass hierarchy range from 0.003 to 0.013. CP-violation can be discovered at  $3\sigma$  confidence level for at least 50 % of possible  $\delta_{CP}$  values and a signal efficiency of 90 % if  $\sin^2 2\theta_{13}$  is greater than 0.016.

As indicated by the GLoBES analysis, efficient rejection of NC events is needed in order to maximize the sensitivity of LENA in a long-baseline experiment. The required ability to deduce general event information from the isotropic light of liquid scintillator for particle identification was demonstrated in [7] and [6] for different energy ranges. The underlying idea is to use the arrival time patterns of the scintillation photons at the PMTs for particle tacking.

Based on these prior works, nine event variables were extracted from simulated particle events in order to conduct a multivariate analysis for discrimination of neutral pions and electrons in liquid scintillator. The particles were directly generated in the energy range from 135 MeV to 1000 MeV with a GEANT4-based simulation of the LENA detector. No neutrino interaction vertex was included in the simulation. Starting position of the primary particle was the center of the cylindrical detector and their initial momentum was restricted to radial direction. Although it is a special analysis case, a TOF-correction applied to the

PMT arrival times of scintillation photons nearly removed the position-dependence of the results and thus make them applicable to other vertex positions.

Six of the deduced event variables were extracted from a non-parametric fit to the event's overall TOF-corrected pulse shape or directly from underlying corrected photon arrival times. Furthermore, two variables characterizing the spatial expansion rate of the TOF-corrected PMT hit pattern around the event's first PMT hit were constructed. The last variable included in the multivariate analysis was the event's reconstructed energy. Strong correlations between the different variables existed. This was expected, as many variables relied on the fundamental information of the pulse shape. However, the correlations grant opportunities to optimize the variable selection in the future.

The actual multivariate analysis was done with boosted decision tree classifiers. Potential overtraining is a serious issue to machine-based learning algorithms and was controlled with comparisons of the classifier's performance on samples of training and test data. In addition, Kolmogorov–Smirnov-tests were done to the classifier's output distributions for signal and background events. Preceding test runs revealed fluctuations of the discrimination performance due to randomized event compositions of training samples. Therefore, the number of boosted decision trees per classifier (25, 100, 400) and their maximum depth (2, 3) were varied between sets of ten classifiers with equal parameter settings. For each of these sets, the signal efficiency was determined at benchmark values of 70 %, 90 % and 99 % background rejection by averaging over the corresponding values from each single classifier. The entire procedure was repeated without reconstructed event energy as variable.

Best discrimination results were obtained for classifiers with 400 boosted decision trees of depth 3 with reconstructed energy included. Their averaged signal efficiencies for the test samples at the above mentioned benchmark values for background rejection were  $(94.1 \pm 0.2)\%$  [70 %],  $(65.3 \pm 0.4)\%$  [90 %] and  $(14.2 \pm 0.6)\%$  [99 %]. In addition to the general analysis, the energy-dependence of the discrimination performance was investigated with classifiers of 100 trees of depth 2. The averaged signal efficiencies for the test samples at 99 % background rejection decreased from  $(14.7 \pm 0.7)\%$  at  $(300 \pm 100)\text{MeV}$  to  $(11.2 \pm 0.6)\%$  at  $(900 \pm 100)\text{MeV}$ . Results in a first energy bin of  $(167.5 \pm 32.5)\text{MeV}$  indicated overtraining due to small training samples, but this has not been corrected for this basic study.

Efficient identification of NC neutral pion background is a basic prerequisite for long-baseline  $\nu_e$  appearance search. The present work has successfully demonstrated the basic feasibility to discriminate single neutral pion event and electron events in LENA on basis of a multivariate analysis with simulated events. Despite the simplifications used in the current analysis state, a more detailed study, which aims to extend the analysis to higher energies and more realistic conditions, is by all means justified.

# Appendix A

## Neutral pion decay kinematics

This section briefly covers some important equations regarding the two-body decay  $\pi^0 \rightarrow \gamma + \gamma$ , which are deduced from relativistic kinematics. The photons are assumed to travel in the  $x$ - $z$ -plane and described by the following denotations:

- $E_i$  : energy,
- $\mathbf{p}_i$  : three-momentum,
- $q_i$  : four-momentum,
- $\alpha$  : opening angle between the photons,

$i = 1, 2$ . Variables marked with " ' " refer to quantities in the rest frame  $\Sigma_R$  of the neutral pion, while normal variables refer to quantities in the laboratory (lab) frame  $\Sigma_L$ . Both frames of reference are related to each other by a special Lorentz transformation:

$$\begin{aligned}x' &= x , \\y' &= y , \\z' &= \gamma(z - \beta t) , \\t' &= \gamma(t - \beta z) ,\end{aligned}$$

with  $\gamma = \frac{1}{\sqrt{1-\beta^2}}$  and  $\beta$  as speed of  $\Sigma_R$  relative to  $\Sigma_L$  in fractions of speed of light in vacuum  $c$ . Natural units ( $\hbar = c = 1$ ) are used.

### Invariant mass of photons in the laboratory frame

With

$$\begin{aligned}E_i &= |\mathbf{p}_i| , \\q_1 &= E_1 (1, 0, 0, 1) , \\q_2 &= E_2 (1, \sin \alpha, 0, \cos \alpha) ,\end{aligned}$$

the square of invariant mass  $m$  for two photons starting from the origin is given by

$$\begin{aligned} m^2 &= (q_1 + q_2)^2 = \underbrace{q_1^2}_0 + \underbrace{q_2^2}_0 + 2 q_1 q_2 \\ &= 2 E_1 E_2 (1 - \cos \alpha) . \end{aligned}$$

With  $\cos \alpha = 1 - 2 \sin^2 \frac{\alpha}{2}$  one finally gets

$$m^2 = 4 E_1 E_2 \sin^2 \frac{\alpha}{2} . \quad (\text{A.1})$$

If the photons come from the decay of a neutral pion with mass  $m_\pi$ ,  $m^2 = m_\pi^2$  must hold.

## Minimum opening angle between photons in the laboratory frame

A neutral pion has momentum  $\mathbf{p}_\pi = p_\pi(0, 0, 1)$ . In  $\Sigma_R$ , the opening angle between the photons from neutral pion decay is always  $\alpha' = \pi$ , as momentum and energy conservation must hold.  $\alpha = \pi$  is realized in  $\Sigma_L$  only if one photon is emitted in the pion's momentum direction and the other one in opposite direction. It corresponds to the case of maximum opening angle.

The opening angle between the photons is minimal for fixed pion energy if they are emitted perpendicular to the direction of boost from  $\Sigma_R$  to  $\Sigma_L$ ,  $\mathbf{p}'_i = \pm \frac{m_\pi}{2} (1, 0, 0) = \mathbf{p}_i$ . In this case, the pion's total energy  $E_\pi$  is equally distributed between the photons:  $E_i = |\mathbf{p}_i| = E_\pi/2$ . In  $\Sigma_L$  both photons have a non-vanishing momentum component in  $z$ -direction due to the boost. Therefore, the following equation holds for both photons:

$$\sin \frac{\alpha_{\min}}{2} = \frac{|\mathbf{p}_{x,i}|}{|\mathbf{p}_i|} = \frac{m_\pi/2}{E_\pi/2}$$

With  $E_\pi = \gamma m_\pi$  one gets

$$\alpha_{\min} = 2 \arcsin \frac{m_\pi}{E_\pi} = 2 \arcsin \frac{1}{\gamma} . \quad (\text{A.2})$$

## Energy distribution between photons

The energy  $E_i$  in  $\Sigma_L$  of a photon from pion decay shall be calculated as a function of pion energy  $E_\pi$  and the opening angle between the photons  $\alpha$ . Let  $E_\pi = E_1 + E_2$  and  $E_\pi > E_1 \geq E_2$ . Starting from Equation A.1 one gets

$$\begin{aligned} m_\pi^2 &= 4 : (E_\pi - E_i) E_i \sin^2 \frac{\alpha}{2} \\ \Leftrightarrow \frac{m_\pi^2}{4 \sin^2 \frac{\alpha}{2}} &= E_i E_\pi - E_i^2 . \end{aligned}$$

Completing the squares on the right-hand side yields

$$\begin{aligned} \left(E_i - \frac{E_\pi}{2}\right)^2 &= \left(\frac{E_\pi}{2}\right)^2 - \frac{m_\pi^2}{4 \sin^2 \frac{\alpha}{2}} \\ \Leftrightarrow E_i &= \frac{E_\pi}{2} \pm \sqrt{\frac{E_\pi^2}{4} - \frac{m_\pi^2}{4 \sin^2 \frac{\alpha}{2}}}. \end{aligned}$$

With  $E_\pi = \gamma m_\pi$  one finally gets

$$E_i = \frac{E_\pi}{2} \left(1 \pm \sqrt{1 - \frac{1}{\gamma^2 \sin^2 \frac{\alpha}{2}}}\right), \quad \sin^2 \frac{\alpha}{2} \in \left[\frac{1}{\gamma^2}, 1\right]. \quad (\text{A.3})$$

The plus sign corresponds to  $E_1$  and the minus sign to  $E_2$ .



# Appendix B

## Utilized software frameworks

The following versions of software frameworks and libraries were for used for preparation of this thesis:

<b>GLoBES</b>	Ver. 3.1.10:	C-based framework commonly used for simulation of long-baseline neutrino oscillations experiments [64][65].
<b>ROOT</b>	Ver. 5.29.02:	Object-oriented data analysis framework developed at CERN [74].
<b>TMVA</b>	Ver. 4.1.2:	Package for multivariate data analysis integrated into the ROOT framework [79].
<b>CLHEP</b>	Ver. 2.0.4.6:	C++ class library specifically developed for high-energy physics. It is a prerequisite for <b>GEANT4</b> .
<b>GEANT4</b>	Ver. 9.3.p02:	Object-oriented Monte Carlo simulation framework developed at CERN. It is mainly used for particle physics applications [72].



# Bibliography

- [1] Pauli, W., Collected Scientific Papers (Interscience Publishers, 1964).
- [2] C. Cowan, F. Reines, F. Harrison, H. Kruse, and A. McGuire, *Science* **124**, 103 (1956).
- [3] Borexino Collaboration, G. Alimonti *et al.*, *Nucl.Instrum.Meth.* **A600**, 568 (2009), 0806.2400.
- [4] P. Alivisatos *et al.*, (1998).
- [5] J. G. Learned, (2009), 0902.4009.
- [6] J. Peltoniemi, (2009), 0909.4974.
- [7] D. Hellgartner, *Lepton track reconstruction in LENA and attenuation length measurements in liquid scintillators*, Diploma thesis, Technische Universität München, 2011.
- [8] P. Schmüser, *Feynman-Graphen und Eichtheorien für Experimentalphysiker (German Edition)* (Springer, 1994).
- [9] J. Davis, Raymond, D. S. Harmer, and K. C. Hoffman, *Phys.Rev.Lett.* **20**, 1205 (1968).
- [10] J. Bahcall, W. A. Fowler, J. Iben, I., and R. Sears, *Astrophys.J.* **137**, 344 (1963).
- [11] SNO Collaboration, Q. Ahmad *et al.*, *Phys.Rev.Lett.* **87**, 071301 (2001), nucl-ex/0106015.
- [12] S. Bilenky, *Introduction to the Physics of Massive and Mixed Neutrinos (Lecture Notes in Physics)* (Springer, 2010).
- [13] L. Wolfenstein, *Phys.Rev.* **D17**, 2369 (1978).
- [14] Particle Data Group, K. Nakamura *et al.*, *J.Phys.G* **G37**, 075021 (2010).
- [15] T. Schwetz, M. Tortola, and J. Valle, *New J.Phys.* **13**, 063004 (2011), 1103.0734.
- [16] T. Schwetz, M. Tortola, and J. Valle, *New J.Phys.* **13**, 109401 (2011), 1108.1376.
- [17] K. Eitel, *Nucl.Phys.Proc.Suppl.* **143**, 197 (2005).
- [18] The T2K Collaboration, Y. Itow *et al.*, p. 239 (2001), hep-ex/0106019.
- [19] T2K Collaboration, K. Abe *et al.*, *Phys.Rev.Lett.* **107**, 041801 (2011), 1106.2822.
- [20] S. K. Agarwalla, T. Li, and A. Rubbia, (2011), 1109.6526.

- [21] V. Barger, D. Marfatia, and K. Whisnant, Phys.Rev. **D65**, 073023 (2002), hep-ph/0112119.
- [22] ASroParticle ERAnet, <http://www.aspera-eu.org>.
- [23] D. Autiero *et al.*, JCAP **0711**, 011 (2007), 0705.0116.
- [24] LAGUNA Collaboration, A. Rubbia, Acta Phys.Polon. **B41**, 1727 (2010).
- [25] LAGUNA - Large Apparatus studying Grand Unification and Neutrino Astrophysics, <http://www.laguna-science.eu/>.
- [26] A. de Bellefon *et al.*, (2006), hep-ex/0607026.
- [27] Y. Fukuda *et al.*, Nucl.Instrum.Meth. **A501**, 418 (2003).
- [28] A. Rubbia, J.Phys.Conf.Ser. **171**, 012020 (2009), 0908.1286.
- [29] ICARUS Collaboration, S. Amerio *et al.*, Nucl.Instrum.Meth. **A527**, 329 (2004).
- [30] A. Rubbia, (2010), 1003.1921.
- [31] OPERA Collaboration, M. Guler *et al.*, (2000).
- [32] LENA Collaboration, M. Wurm *et al.*, (2011), 1104.5620.
- [33] T. M. Undagoitia, *Measurement of light emission in organic liquid scintillators and studies towards the search for proton decay in the future large-scale detector LENA*, PhD thesis, Technische Universität München, 2008.
- [34] C. Grupen, *Teilchendetektoren (German Edition)* (, 1993).
- [35] W. Trzaska *et al.*, Acta Phys.Polon. **B41**, 1779 (2010).
- [36] L. Mosca, Acta Phys.Polon. **B41**, 1773 (2010).
- [37] K. Zuber, *Neutrino Physics (Series in High Energy Physics, Cosmology and Gravitation)* (Taylor & Francis, 2003).
- [38] J. N. Bahcall, A. M. Serenelli, and S. Basu, Astrophys.J. **621**, L85 (2005), astro-ph/0412440.
- [39] SNO Collaboration, J. Boger *et al.*, Nucl.Instrum.Meth. **A449**, 172 (2000), nucl-ex/9910016.
- [40] H.-T. Janka, K. Langanke, A. Marek, G. Martinez-Pinedo, and B. Mueller, Phys.Rept. **442**, 38 (2007), astro-ph/0612072.
- [41] A. Weigert, H. J. Wendker, and L. Wisotzki, *Astronomie und Astrophysik: Ein Grundkurs (German Edition)* (Wiley-VCH, 2005).
- [42] J. F. Beacom, Ann.Rev.Nucl.Part.Sci. **60**, 439 (2010), 1004.3311.

- [43] W. Arnett, J. N. Bahcall, R. Kirshner, and S. Woosley, *Ann.Rev.Astron.Astrophys.* **27**, 629 (1989).
- [44] J. M. Winter, *Phenomenology of Supernova Neutrinos, Spatial Event Reconstruction, and Scintillation Light Yield Measurements for the Liquid-Scintillator Detector LENA*, Diploma thesis, Technische Universität München, 2007.
- [45] T. Araki *et al.*, *Nature* **436**, 499 (2005).
- [46] G. Bellini *et al.*, *Phys.Lett.* **B687**, 299 (2010), 1003.0284.
- [47] P. Coloma, T. Li, and S. Pascoli, (2011), 1110.1402.
- [48] Borexino Collaboration, G. Bellini *et al.*, *JINST* **6**, P05005 (2011), 1101.3101.
- [49] KamLAND Collaboration, S. Abe *et al.*, *Phys.Rev.* **C81**, 025807 (2010), 0907.0066.
- [50] Super-Kamiokande Collaboration, H. Nishino *et al.*, *Phys.Rev.Lett.* **102**, 141801 (2009), 0903.0676.
- [51] Super-Kamiokande Collaboration, K. Kobayashi *et al.*, *Phys.Rev.* **D72**, 052007 (2005), hep-ex/0502026.
- [52] P. Zucchelli, *Phys.Lett.* **B532**, 166 (2002).
- [53] A. Cervera *et al.*, *Nucl.Phys.* **B579**, 17 (2000), hep-ph/0002108.
- [54] E. Gschwendtner *et al.*, *Conf.Proc.* **C100523**, THPEC046 (2010).
- [55] R. Acquafredda *et al.*, *JINST* **4**, P04018 (2009).
- [56] SciBooNE Collaboration, A. Aguilar-Arevalo *et al.*, (2006), hep-ex/0601022, Spokespersons: T. Nakaya, M.O. Wascko.
- [57] E. Paschos and J. Yu, *Phys.Rev.* **D65**, 033002 (2002), hep-ph/0107261.
- [58] E. Paschos, L. Pasquali, and J. Yu, *Nucl.Phys.* **B588**, 263 (2000), hep-ph/0005255.
- [59] Y. Kurimoto, (2010), Ph.D. Thesis (Advisor: Tsuyoshi Nakaya).
- [60] W. R. Leo, *Techniques for Nuclear and Particle Physics Experiments: A How-to Approach* (Springer, 1994).
- [61] D. Stefan, (2011), 1110.1652.
- [62] MiniBooNE Collaboration, A. Aguilar-Arevalo *et al.*, *Nucl.Instrum.Meth.* **A599**, 28 (2009), 0806.4201.
- [63] R. Patterson *et al.*, *Nucl.Instrum.Meth.* **A608**, 206 (2009), 0902.2222.
- [64] P. Huber, M. Lindner, and W. Winter, *Comput.Phys.Commun.* **167**, 195 (2005), hep-ph/0407333.

- [65] P. Huber, J. Kopp, M. Lindner, M. Rolinec, and W. Winter, *Comput.Phys.Commun.* **177**, 432 (2007), hep-ph/0701187.
- [66] J. Peltoniemi, (2009), 0911.4876.
- [67] E. Kozlovskaya, J. Peltoniemi, and J. Sarkamo, (2003), hep-ph/0305042.
- [68] A. Dziewonski and D. Anderson, *Phys.Earth Planet.Interiors* **25**, 297 (1981).
- [69] A. Longhin, *PoS ICHEP2010*, 325 (2010).
- [70] A. Longhin, Neutrino fluxes for the LAGUNA sites, <http://irfu.cea.fr/en/Phoce/Pisp/index.php?id=72>.
- [71] M. D. Messier, UMI-99-23965.
- [72] GEANT4, S. Agostinelli *et al.*, *Nucl.Instrum.Meth.* **A506**, 250 (2003).
- [73] M. Wurm, Private communication, Institut für Experimentalphysik, Universität Hamburg, 2011.
- [74] R. Brun and F. Rademakers, *Nucl.Instrum.Meth.* **A389**, 81 (1997).
- [75] F. James and M. Roos, *Comput.Phys.Commun.* **10**, 343 (1975).
- [76] D. Hellgartner, Private communication, Chair for Experimental Physics and Astroparticle Physics, Technische Universität München, 2011.
- [77] B. Povh, K. Rith, and C. Scholz, *Teilchen Und Kerne: Eine Einführung in die physikalischen Konzepte (Springer-Lehrbuch) (German Edition)* (Springer, 1999).
- [78] K. S. Cranmer, *Comput.Phys.Commun.* **136**, 198 (2001), hep-ex/0011057.
- [79] A. Hocker *et al.*, *PoS ACAT*, 040 (2007), physics/0703039.
- [80] H.-J. Yang, B. P. Roe, and J. Zhu, *Nucl.Instrum.Meth.* **A555**, 370 (2005), physics/0508045.
- [81] Y. Freund and R. E. Schapire, Experiments with a New Boosting Algorithm, in *In Proceedings of the Thirteenth International Conference on Machine Learning*, pp. 148–156, 1996.
- [82] F. James, *Statistical Methods in Experimental Physics(2nd Edition)* (World Scientific Publishing Company, 2006).
- [83] K. A. Semendjajew, *Taschenbuch der Mathematik* (Deutsch Harri GmbH, 2005).

# Danksagung

Zum Abschluss möchte ich an dieser Stelle allen danken, die mich bei der Fertigstellung dieser Arbeit unterstützt haben.

Mein Dank geht an Prof. Dr. Caren Hagner, die mich in Ihre Neutrinophysik-Arbeitsgruppe aufgenommen und zur Anfertigung einer Diplomarbeit zum Themengebiet LENA motiviert hat.

Allergrößter Dank geht an Dr. Michael Wurm für das Stellen des spannenden und herausfordernden Diplomarbeitsthemas. Ich danke ihm für die außerordentliche Hilfs- und Einsatzbereitschaft bei der Betreuung dieser Arbeit, für die Hinweise zur schriftlichen Ausarbeitung und für seine schier endlose Geduld.

I want to thank Prof. Dr. Alessandro Mirizzi for elaboration of the second opinion on my thesis.

Selbstverständlich gilt mein Dank der gesamten Neutrinophysik-Arbeitsgruppe, die mich freundlich aufgenommen und mir stets mit Rat und Tat zur Seite gestanden hat. Ich bedanke mich für konstruktive Kritik an meiner Arbeit, Hilfsbereitschaft bei Problemen mit der EDV, interessante Diskussionen beim Mittagessen, spannende Matches am Kicker-Tisch und leckere Kuchen in der Teeküche bei: Prof. Dr. Caren Hagner, Prof. Dr. Walter Schmidt-Parzefall, Dr. Daniel Bick, Dr. Joachim Ebert, Dr. Björn Wonsak, Dr. Michael Wurm, Torben Ferber, Christoph Göllnitz, Nadine Heidrich, Martin Hierholzer, Annika Hollnagel, Jan Lenkeit, Christian Oldorf, Jan Timm, Benjamin Büttner, Mikko Meyer, Manuel Harder, Markus Kaiser, Hans-Jürgen Ohmacht und Volker Braunert.

Besonderer Dank geht an Dr. Daniel Bick für die Betreuung in den ersten Wochen meiner Arbeit. Vielen Dank an Nadine Heidrich, Annika Hollnagel und Christian Oldorf für das Korrekturlesen der Arbeit.

Für das Zurverfügungstellen der Ergebnisse seiner Arbeit, die mir viel Zeit erspart haben, geht ein großer Dank an Dominikus Hellgartner. Außerdem danke ich ihm für ausführliche Beantwortung meiner vielen Fragen und Hilfestellungen bei Problemen. Ebenfalls besonderer Dank geht an Randolph Möllenberg, der durch die Betreuung und Bereitstellung der LENA-Simulation fundamental zur Ermöglichung und Bearbeitung der Aufgabenstellung beigetragen hat. I also want to thank Dr. Juha Peltoniemi and Tracey Li for helping me with the GloBES software and for sharing their files and information with me.

Ich bedanke mich außerdem bei Lukas Hoppenau, Kim Susan Petersen, Shigeko Schlüter,

Marc Stöver, Annika Vanhoefer und Christian Ziemann.

Zum Schluss möchte ich meinen Eltern und meiner Schwester dafür danken, dass Sie mir stets in meinem Leben zur Seite stehen. Meinen Eltern möchte ich besonders dafür danken, dass sie mir das Physikstudium ermöglichten und mich stets in seinem Verlauf unterstützt haben.

Hiermit versichere ich, die vorliegende Arbeit selbständig und ausschließlich mit den angegebenen Quellen und Hilfsmitteln verfasst zu haben.

Mit der Veröffentlichung dieser Arbeit und der Auslage in der Bibliothek bin ich einverstanden.

Hamburg, Januar 2012

Sebastian Lorenz